Cranfield University

Ashley James

Oxide Thermoelectric Energy Harvesting Materials

School of Applied Sciences

PhD

Academic Year: 2014

Supervised by: Prof. Robert Dorey
Dr. Paul Jones

November 2014

Cranfield University

Ashley James

Oxide Thermoelectric Energy Harvesting Materials

School of Applied Sciences

PhD

Academic Year: 2014

Supervised by: Prof. Robert Dorey
Dr. Paul Jones

November 2014

Abstract

Conventional thermoelectric materials found in many thermoelectric devices have unfavourable properties; they often suffer instability at high temperatures and contain toxic metals which pose a hazard to the environment. Oxide thermoelectric materials are stable, less toxic and could eventually replace conventional materials. The thermoelectric performance of oxide materials currently do not match conventional materials however, there is potential for improvement through doping and altering the microstructure and chemistry through modification of the processing conditions. This project aims to examine the doping and processing conditions and the effect this has upon the thermoelectric behaviour of oxide based thermoelectric materials.

Zinc oxide (ZnO) has been investigated as an oxide thermoelectric material and doping of ZnO with aluminium (Al) and antimony (Sb) by mixed oxide synthesis was investigated. Al_2O_3 and Sb_2O_3 were used as aluminium (Al) and antimony (Sb) dopant sources for ZnO, which were reacted with ZnO at temperatures of 1000°C-1300°C. Al was found to incorporate effectively into the ZnO system and was shown to produce n-type behaviour. The Sb doped ZnO material was also found to display n-type behaviour which is intriguing as Sb is considered a p-type dopant in the ZnO system; at low levels <1.0at.%, Sb incorporates onto the Zn site rather than the O site as expected, which leads to n-type behaviour. The addition of Sb dopant leads to the formation of secondary phase of $Zn_7Sb_2O_{12}$, which appears to increase the Seebeck coefficient by an energy filtering effect with higher levels of dopant leading to higher levels of secondary phase. Grain size and porosity also play a significant role in both the Al and Sb doped systems with small grains and higher levels of porosity leading to higher values of Seebeck coefficient up to $-100\mu V.K^{-1}$ for Al (0.5at.%) and $-115\mu V.K^{-1}$ for Sb (0.8at.%). The ZT figure of merits were found to be highest for materials sintered at 1300°C with values of 6×10^{-5} and 2×10^{-10} for Al and Sb doped ZnO respectively, these values are low compared to literature values, which are in the region of 0.01. This is due to high electrical resistivities of the synthesised samples, which is linked to porosity.

A better understanding of the effects that microstructure plays on thermoelectric behaviour has been developed and procedures to isolate the contributions from grain size, and degree of dopant incorporation to the thermoelectric properties have been conducted.

Acknowledgements

I would like to thank all those who have helped and supervised me in my PhD. Professor Rob Dorey and Dr. Paul Jones who helped me develop my skills as a researcher, and guided me through my PhD and who made sure I completed my work successfully and who provided me with helpful and excellent suggestions to develop this thesis.

Andrew Stallard and Dr. Chris Shaw, without whom I could not have obtained the results needed. I would also like to thank my colleagues in our group with who have been of great help. Also to Enza Giaracuni who has been a great help with administration.

My thanks go out to my father, Christopher, my grandmother, Margaret, and my grandfather, Leslie for their love and support throughout my studies, also my brothers, Tristan, Hedley, and Rory, my uncle, Peter and the rest of my family and friends. My thanks also go out to my mother, Linda, whose love and memory has kept me inspired and without whom I would never have made it here. My special thanks go to Kate Sadler who has always been there for me and has provided a great deal of strength and support.

Finally I would like to acknowledge the financial support provided by European Thermodynamics Limited and EPSRC.

Contents

List of Figures

List of tables

1. Introduction

Thermoelectric energy conversion is regarded as a promising technology for both electrical power generation from waste heat and for cooling applications. Thermoelectric materials develop an electrical charge when a temperature gradient is applied across them. This charge can then be utilised in an external system or stored in a capacitor or battery for later use. The Peltier effect is the reversal of this process, where an electrical current is applied a temperature gradient can be developed across the material.

Conventional thermoelectric materials consist of intermetallic compounds such as bismuth telluride and silicon-germanium. These are high performing but have unfavourable properties; they often suffer from instability due to oxidation in air, contain toxic metals which pose a hazard to the environment, and are often costly to manufacture. Some contain scarce elements which question whether there will be long term availability. Oxide materials which are more stable, less toxic and lower in cost could potentially replace these intermetallic materials. The thermoelectric performances of oxide materials such as strontium titanate and sodium cobaltate are higher than other oxides but currently do not match performance levels of commercial thermoelectric materials. There is potential for improving the properties by modifying the microstructure of the material and doping. If the performance of oxide thermoelectric materials were improved it would expand the industry by making thermoelectric devices more cost effective and reducing the impact upon the environment. This project will focus on the development of oxide materials as an alternative to intermetallic thermoelectric materials and the improvement of their performance.

The electrical and thermal conductivities, together with the Seebeck coefficient, affect the thermoelectric behaviour of thermoelectric materials. Lower thermal conductivity improves the thermoelectric behaviour by slowing the heat transportation and thus increasing the temperature difference across the material. A higher electrical conductivity is important to reduce losses through resistance and a high Seebeck coefficient is important as it dictates how much voltage is produced across the material for a given temperature difference.

Aim and objectives

The aim of this work is to examine the effect of doping and processing conditions on the electrical and thermal conductivities and Seebeck coefficient and hence thermoelectric performance of oxide thermoelectric materials.

In order to accomplish this, the following objectives need to be met.

- Synthesis of doped and undoped oxide thermoelectric materials
- Characterisation of electrical conductivity, thermal conductivity and Seebeck coefficient of materials
- Evaluation of thermoelectric behaviour through the thermoelectric figure of merit (ZT), and power factor
- Linking the observed microstructures and composition to the observed thermal, electrical, and thermoelectric behaviour

Structure of thesis

The structure of the thesis is detailed below, included are the chapter titles and descriptions of each section.

2. Literature review

   The literature review gives an introduction to energy harvesting, the methods utilised in order to scavenge energy from various sources and their applications. An introduction into thermoelectrics and their applications is reviewed including what material properties are deemed desirable when identifying thermoelectric materials for uses in various applications. The review then looks on alternatives to conventional thermoelectric materials with a focus on oxide thermoelectric materials.

3. Methodology

   The first part of the methodology section describes the steps carried out to synthesise the materials including powder preparation, doping of the material, milling, thermal treatment, forming pellets, and sintering treatments. The second part of the method section gives a description of the sample preparation and analysis of the properties of the materials including SEM, XRD, electrical characterisation, calculation of porosity, and thermoelectric characterisation of the materials in terms of Seebeck coefficient and thermal conductivity.

4. Porosity dependent variables

   This chapter focuses on the properties that are strongly dependent upon the level of porosity of the material. Comparisons of the porosity of doped samples sintered at different temperatures are carried out while linking to various porosity models and experimental data obtained from SEM and XRD analysis. The crystallography data is linked to porosity and used to explain observations in microstructure.

5. Electrical and thermal conductivity

   The effect that porosity has on the electrical and thermal conduction of doped ZnO is investigated. By linking porosity effects to known models and experimental data obtained, the effects that doping has on the electrical and thermal properties is studied.

6. Seebeck

   An analysis of the Seebeck measurements is carried out for the samples and the effect that the level of dopant inclusion and the degree of porosity is linked to observations.

7. Thermoelectric behaviour

   The overall thermoelectric behaviour is analysed by bringing together experimental data in previous chapters and identifying idealised material in terms of dopant level as well as microstructure.

2. Literature review

2.1. Energy harvesting

Energy harvesting is the gathering of energy available in the local environment (Lee et al., 2013) and may either be stored or used immediately. Examples of energy harvesting include solar cells for capturing solar energy, piezoelectric devices for capturing vibration energy, and wind turbines for capturing energy from the wind. Energy can also be captured from waste sources such as heat from an automobile exhaust unit and excess body heat. There are several advantages of energy harvesting over powering from energy storage devices (such as batteries and capacitors) or generators (such as diesel/petrol fuelled generators) which include the reduced need for maintenance, refuelling, and the replacement of batteries. For example, remote weather stations are able to harvest environmental energy in order to operate which reduces maintenance required to change the batteries or maintain generator units, while pacemakers can make use of the body's natural temperature to harvest power which is advantageous because changing the battery requires a medical procedure which is both costly and stressful for the patient.

Energy may be harvested from areas where there are excess amounts of mechanical vibration, light, or heat. Special designed systems are able to capture some of this energy which can then be utilised.

2.2. Thermoelectric materials

Thermoelectric materials have attracted attention in recent years due to their use in a wide variety of applications. When a thermoelectric material is subjected to a temperature difference along its length, the charge carriers within the material flow along the thermal gradient and the energy can be captured. Two materials, one n-type and one p-type are connected in parallel to a heat source and heat sink and electrically in series. Electrons are transferred due to the different temperatures resulting in an electric potential. This process is reversible, a temperature difference can be induced if a potential is applied.

One factor limiting the use of thermoelectrics for energy generation is the low conversion efficiency of thermoelectric modules (~5%) (Rowe and Min, 1998) however, where the cost of thermal input is not a concern, for example when harvesting energy from sources of wasted heat, a low conversion efficiency is not a drawback. The main factor to consider is to maximise power output.

2.3. Seebeck coefficient

The basis of thermocouples was established by Thomas Johann Seebeck in 1821 when he discovered that when a junction of two different conductors is heated, a voltage is produced. He discovered that the voltage generated by the two conductors can be related to the corresponding temperature gradient between the junction and the ends of the conductors. Different materials have different Seebeck coefficients which are a measure of how much voltage is generated for a given temperature difference (Fleurial, 2009). It is an essential property for evaluating the potential performance of thermoelectric materials. The charge carriers flow down the thermal gradient from heat source to heat sink, for n- type material the charge carriers are electrons for p- type material the charge carriers are holes.

2.4. Figure of merit

Thermoelectric materials are generally ranked using the figure of merit, Z. Frequently the dimensionless figure of merit, ZT, will be used in its place because the terms have a dependence on temperature, *equation (1)*.

$$ZT = \frac{S^2 \sigma T}{\kappa} \qquad (1)$$

Where S is the Seebeck coefficient, σ is the electrical conductivity, T is the absolute temperature of the material (usually taken as the average of the temperatures from the hot and cold side of the sample) and κ is the thermal conductivity which is comprised from the sum of contributions from the electrical charge carriers, κ_{el} and the phonon lattice vibrations, κ_{ph}. A high Seebeck coefficient is required to output a high voltage for a given temperature difference, a high electrical conductivity is important to ensure that losses through electrical resistance are minimal, and a low thermal conductivity to ensure a high temperature difference is maintained.

The power generated by a thermoelectric material, P, is given by *equation (2)* where V is the voltage produced and ΔT is the temperature difference between the hot side and the cold side of the material. From this a power factor term ($S^2\sigma$) can be defined to predict the relative effectiveness of different materials

$$P = V^2\sigma = S^2\sigma\Delta T^2 \quad (2)$$

In metals the main contribution to thermal conductivity is from the charge carriers so $\kappa_{el} >> \kappa_{ph}$ generally holds true. As κ_{el} is proportional to the electrical conductivity by means of the Wiedemann-Franz law, *equation (3)*, where L_0 is the Lorentz number (Ohtaki and Hayashi, 2006), ZT can be given by *equation (4)*.

$$\kappa_{el} = L_0\sigma T \quad (3)$$

$$ZT = \frac{S^2}{L_0} \quad (4)$$

This shows that the only way to improve ZT in metals is to increase the Seebeck coefficient, however metals generally have very small S due to high carrier density (Ohtaki and Hayashi, 2006) therefore are unsuitable for high ZT materials. In semiconductors, where the concentrations of charge carriers are generally much lower than in metals, high ZT values can be obtained by various means because the condition $\kappa_{el} << \kappa_{ph}$ holds and *equation (1)* is valid. However, the power factor, $S^2\sigma$ is at a maximum at an optimal carrier concentration regardless of the material used (*Figure 1)*. This requires a higher carrier mobility and for the thermal conductivity to be minimised in order to increase ZT. This leads to an issue with attempts at improving ZT, as low thermal conductivity and high electrical conductivity rarely occur in real materials because scattering centres for phonons usually also scatter electrons. Therefore if one parameter is changed, it often changes the other resulting in little or no increase in ZT. However, it is possible to alter the relative scattering of phonons and electrons by carefully modifying the structure of the material by including point defects, dislocations, grain boundaries, and inclusions which can reduce the thermal conductivity through phonon scattering with minimum effect to electric conductivity.

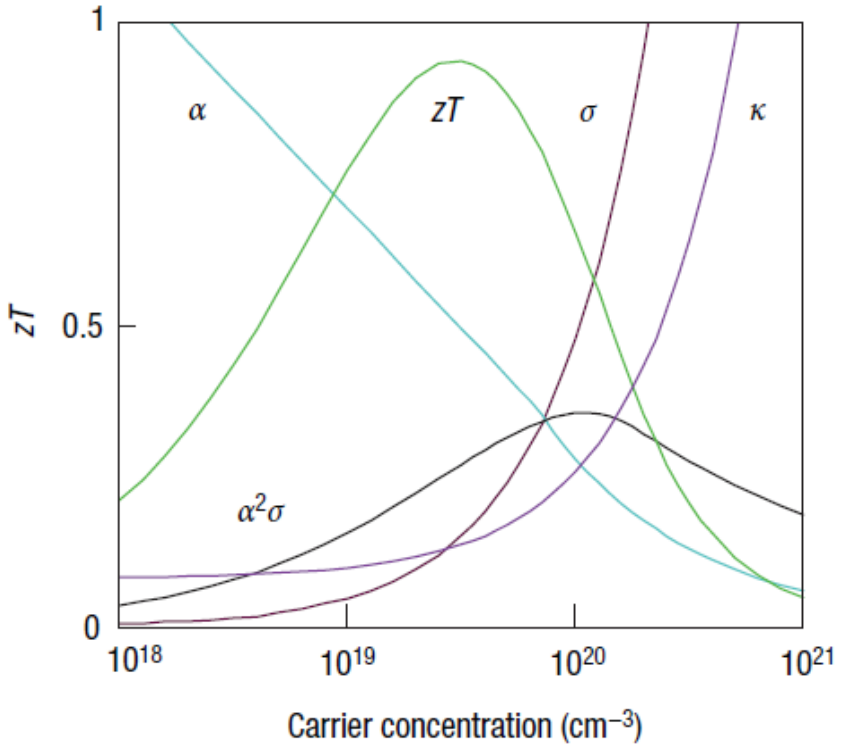

Figure 1: Maximising the figure of merit (ZT) of thermoelectric materials involves a compromise of the thermal conductivity (κ) and Seebeck coefficient (α) with the electrical conductivity (σ) (Snyder and Toberer, 2008)

2.5. Thermal conductivity

In a solid, heat is conducted by phonons and charge carriers (electrons and holes). As atoms in a solid are bound to their neighbours, any disturbance in one is passed onto the next and therefore the atoms are in a permanent state of vibration and the overall motion can be thought of as waves, which can be either longitudinal or transverse (Ruoho, 2012). Low frequency lattice vibrations are acoustic but high frequency waves are more important for heat conduction. When phonons interact with charge carriers, phonon drag occurs; this is when the momentum of the phonons is transferred to the charge carriers. This phenomenon becomes smaller as the concentration of charge carriers increases and is thought to prevent the use of phonon drag being used as a mechanism for improving the thermoelectric figure of merit (Ruoho, 2012).

A common method adopted to improve a material's thermoelectric figure of merit is to reduce the lattice thermal conductivity. This can be achieved in a number of ways; for example, phonons can be scattered by creating point defects such as interstitials or vacancies or at interfaces (Snyder and Toberer, 2008). Low thermal conductivity can also be found in materials with a complex crystal structure, for example, materials such as $CsBi_4Te_6$ have lower lattice thermal conductivities than Bi_2Te_3 due to the Cs layers and Bi-Bi bonds which are not found in Bi_2Te_3 (Snyder and Toberer, 2008). Rattling structures such as Skutterudites have also been found to have low thermal conductivities due to a 'rattling' ion which scatters phonons.

In porous materials, a large volume fraction of open pores are beneficial for heat insulation but have a negative effect on the electrical conduction through the material. This is due to there being less electrically conductive material available per unit volume and also the pore surface acts to scatter electrons as well as phonons. If the volume fraction of porosity is kept small and the size of the pores reduced and distributed evenly throughout the matrix material while avoiding a network of connecting pores, the result would be an almost dense material with small discreet pores evenly scattered throughout (Ohtaki and Hayashi, 2006). The distribution of pores can be carefully tuned to the scale of the mean free path of the

phonons which disrupts their path but has minimal effect on the electron conduction. Ohtaki and Hayashi (Ohtaki and Hayashi, 2006) introduced a nanovoid structure into Al doped ZnO matrix material for selective phonon scattering, by creating a homogenous distribution of 150nm sized voids within the material, which were created by dispersing combustible nanosized material within the doped ZnO powder before thermal treatment. The electrical and thermal conductivities were reduced from bulk values, and an increase in the Seebeck coefficient was also observed. Due to the improvements in these properties, the overall ZT value was improved by up to 0.65.

2.6. Thermoelectric device efficiency

When considering the efficiency of a thermoelectric device, there are factors to consider other than the maximum ZT of the active materials within the device. For a thermoelectric generator, the device ZT (ZT_D) is considered. ZT_D differs from the material ZT because ZT_D is based on the overall performance of the system and includes external sources of thermal and electrical loss. The efficiency, η of a thermoelectric material can be determined from ZT, *Equation (5)* and the device efficiency by substituting ZT for ZT_D.

$$\eta = \frac{\Delta T}{T_h} \cdot \frac{\sqrt{1+ZT}-1}{\sqrt{1+ZT}+\frac{T_c}{T_h}} \qquad (5)$$

Like all heat engines, the maximum efficiency possible is limited by the Carnot efficiency, *equation (6)*.

$$\eta = 1 - \frac{T_c}{T_h} \qquad (6)$$

If a perfect device existed, where there are no external thermal or electric losses and the n-type and p- type thermoelectric material properties were matched (S, σ, κ) the maximum

device efficiency could be given by *Equation (5)* using the material ZT (Snyder and Toberer, 2008).

2.7. Shape

A conventional thermoelectric device consists of n- and p- type legs which are made of blocks of thermoelectric material. (Min and Rowe, 1992) calculated that decreasing the length of the legs of the semiconductor material increases the power output of the module. This is beneficial not only because the module is capable of delivering higher power with the same materials but less active material is used (Min and Rowe, 1992). Min calculated that a reduction in thermoelement length from 2.54mm to 0.5mm gave an increase in power by approximately 75%. This increase in power was accompanied by an acceptably small decrease in conversion efficiency of around 8%.

A single thermoelectric couple is shown in *Figure 2* it consists of n-type and p-type thermo elements connected by electrically conducting strips and supported by two thermally conductive ceramic plates. When contact effects are neglected, the power output of the ideal thermoelectric generator is given by *equation (7)*, where ρ is the electrical resistivity, ΔT is the temperature difference across the thermo elements, A is the cross sectional area and L is the length of the thermo elements.

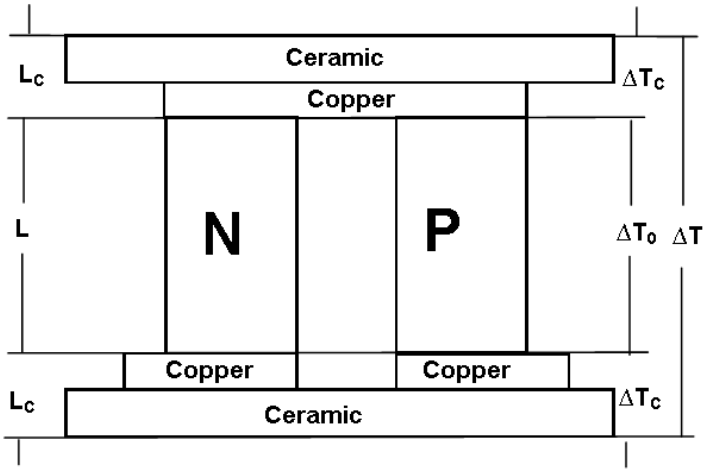

Figure 2: Single couple thermoelectric module (Min and Rowe, 1992)

$$P = \frac{S^2 \Delta T}{2\rho} \cdot \frac{A}{L} \qquad (7)$$

The implication of *equation (7)* is that the power output approaches infinity as the length of the thermo elements approaches zero. In an actual device this cannot be realised due to physical factors such as the thermal and electrical resistances as well as being unable to maintain a temperature difference.

Efforts to optimise the geometry of a thermoelectric element by minimising the thermal conductivity, κ, do not specify actual dimensions. There are other factors to take into account when optimising the dimensions for improved thermoelectric performance, for example, the contact resistance at the end of the thermoelectric element legs and the heat leakage to the cold junction through spaces around the thermo elements. Not all the heat that reaches the cold junction travels through the thermo elements, heat is transferred through radiation and also convection if the device is not operating in a vacuum. Thermal resistance occurs at the ends of the thermo elements due to contact resistances where the element joins the electrical contact strips and ceramic plates. The thermal resistances as

well as the heat leakage reduce the thermal gradient across the thermoelectric elements and therefore reduce the power output of the device.

(Omer and Infield, 1998) developed an improved thermoelectric model that allows geometric optimisation of the thermo elements in power generation mode. The model takes into account the effects of heat leakage and thermal contact resistance for the optimisation of the thermoelement length based on maximum power output from the device. The results obtained agree well with experimental results *Figure 3* and predicts that devices based on previous optimisation methods do not perform as well as devices based on the improved model.

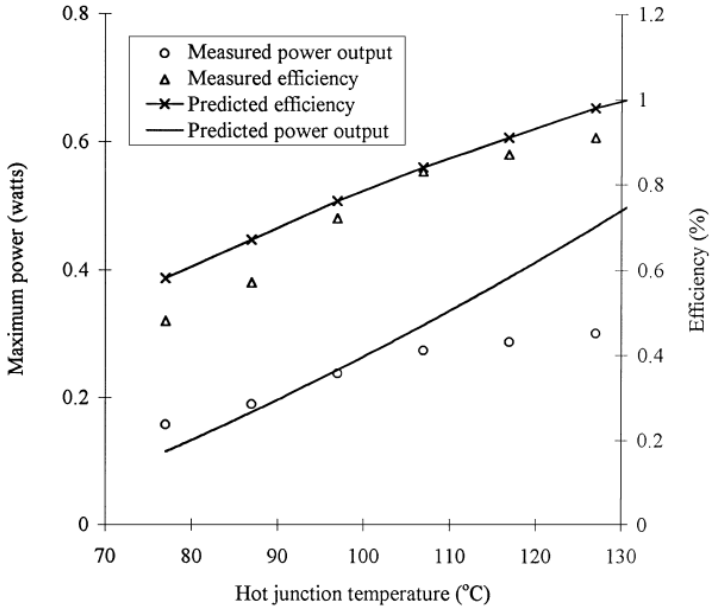

Figure 3: Comparison between predicted and measured results for the commercial device. (Omer and Infield, 1998)

2.8. Load matching

When a thermoelectric module is connected to a load, in order to establish a high power output, load matching is required in order to maintain best performance. Often a DC-DC converter is inserted between the thermoelectric module and the load in order to achieve load matching. The load matching keeps the module running at peak power output; this is usually achieved by matching the resistance of the load to the internal resistance of the module. Due to the effects of Thompson heating (Nagayoshi et al., 2002), the internal resistance of the module changes with temperature difference which means that in order to maintain a maximum power output, the load resistance must be varied with changes of the operating temperature of the module. (Freunek et al., 2009) experimented with dynamic load matching using a feedback method and discovered that the power output can be 5% more than just normal single point load matching.

Nagayoshi (Nagayoshi et al., 2002) used a method known as maximum power point tracking (MPPT) to keep the load matched to the thermoelectric module. This approach is usually applied to photovoltaic devices, typically solar cells because the optimum operation voltage changes with light intensity from the sun which widely changes with time. In thermoelectric power generation the fluctuation characteristics of the temperature difference depend on the thermal source which can often fluctuate with time. Nagayoshi also used the same circuit to deliver a constant voltage output which was set to the same voltage as the maximum voltage output that was delivered by the module at maximum temperature difference. *Figure 4* shows the graph of power as a function of temperature difference. The MPPT shows a wide range of load matching ability compared to the fixed voltage method.

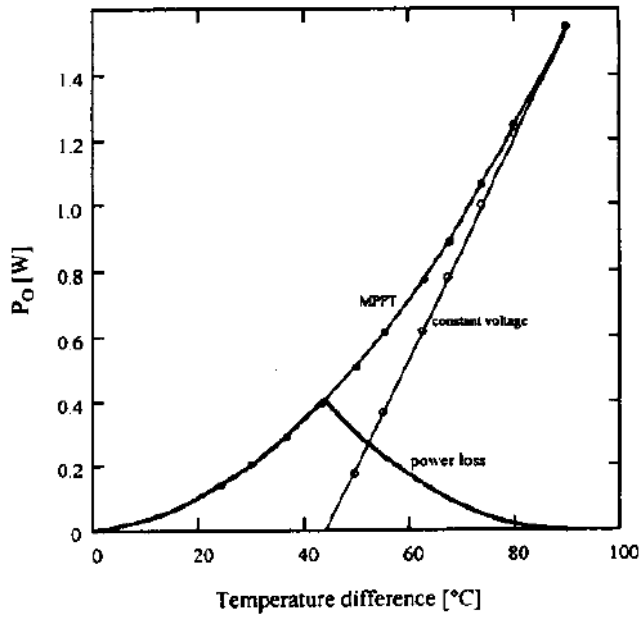

Figure 4: Power output as a function of temperature difference across TEM. The bold line shows mismatched power loss of constant voltage method (Nagayoshi et al., 2002)

2.9. Switching mode

M. Apostol and M. Nedelcu (Apostol and Nedelcu, 2001) proposed a new model for thermoelectric transport which relies on "chopping" the electric contact from the thermoelectric module to the load. Rather than the conventional steady state condition of a constant electron flow commonly utilised in thermoelectric energy generation systems, the switching of the electric supply acts as a pumping system and higher powers can be obtained.

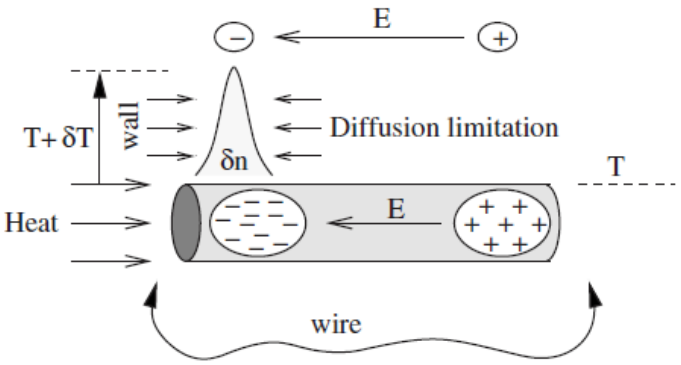

Figure 5: Pulse build up in a TE element (Apostol and Nedelcu, 2010)

In open circuit condition, raising the temperature of one end of a thermoelectric material will increase the proportion of charge carriers in one portion of the material and deplete in another. For a p-type material the charge carriers are holes, which will migrate from the heated end of the material to the cooler end. This creates a separation of charge in the material where a higher concentration of holes develop at the cool end of the material and a higher concentration of electrons develop at the heated end, diminishing their concentration in the rest of the sample. If the two ends of the sample are electrically connected through an external circuit, such as a wire *Figure 5*, the accumulation of charge will discharge through the wire, the electrons will flow through the circuit in a very short amount of time and the electrical energy from the electron flow can be utilised. After completing the circuit, the electron pulse reaches the cold end of the sample, if the circuit is left closed, the electrons will continue through the circuit endlessly and the concentration of electrons in the pulse will dissipate over the length of the material until steady state conduction is reached where the electron flow will pass in usual thermoelectric manner.

The electric pulse can deliver higher power to an external circuit than in steady state condition (Apostol and Nedelcu, 2010). In order to avoid the stationary condition, the contact to the external circuit must be interrupted once the electron pulse reaches the cool end of the material. With the external circuit disconnected, the thermoelectric transport increases the concentration of electrons at the hot side of the material and decreases from the fresh supply of electrons at the cold end. The sample is ready for another operational

cycle and the electric connections can be made to the circuit again (Apostol and Nedelcu, 2010).

This way, the system is behaving truly as a thermo engine by pumping electrons through a circuit in pulses. The electric contacts must be connected and disconnected with a well defined frequency given by the time required to build up an electron pulse while the thermal contacts are permanently maintained. M. Nedelcu (Nedelcu et al., 2002) attempted to test this theory by periodically interrupting the current output of a thermoelectric generator using a MOSFET (metal oxide semiconductor field-effect transistor) acting as an electronic switch. A square wave signal was applied to the MOSFET to switch the output at a frequency of 5KHz. The power output of the pulsed module was slightly higher than for the module under steady state condition, the frequency was not operating at optimum levels and the author expects fine tuning of the pulse width to yield better results.

2.10. Thermoelectric materials

Conventional thermoelectric materials consist of intermetallic compounds such as bismuth telluride, lead telluride and silicon-germanium. These are high performing with ZT ~1 but have unfavourable properties; they often suffer from instability due to oxidation in air, contain toxic elements which pose a hazard to the environment, are often expensive to manufacture and some contain scarce elements which question whether there will be long term availability. Despite these issues, these materials are still widely used in the field of energy harvesting.

The most widely used thermoelectric materials are alloys of tellurides, (Bi_2Te_3, PbTe, Sb_2Te_3). For low temperature applications of up to 200°C, alloys of Bi_2Te_3 have the largest figure of merit for both n- and p- type thermoelectric systems, having a peak ZT from 0.8 to 1.1 with p-type material obtaining higher values, *Figure 6* (Snyder and Toberer, 2008). For mid temperature ranges (200-600°C), typically group IV tellurides are used such as Pb_2Te_3 and GeTe and have maximum ZT of around 0.8. High temperature thermoelectric

generators (>600°C) typically use silicon-germanium alloys for both n- and p- type material, the ZT of which is typically lower due to high thermal conductivity of the crystal lattice.

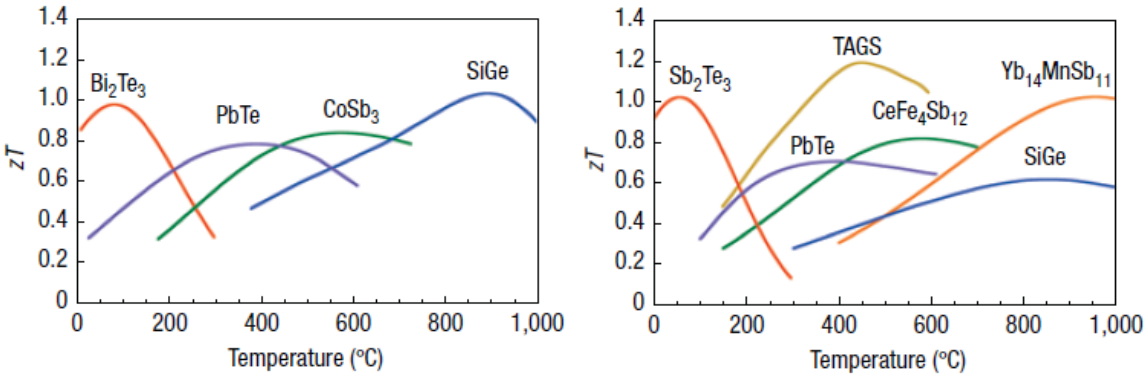

n-Type ZT p-type ZT

Figure 6: Figure of merit, ZT of some thermoelectric materials. (Snyder and Toberer, 2008)

2.11. Cobalt based oxide materials

Colbalt based p-type oxide semiconductors such as Na_xCoO_2, which exhibit large thermoelectric figures of merit, have attracted much attention for the realisation of high temperature thermoelectric power generation (He et al., 2011). This has sparked great interest into oxide materials due to their various advantages over standard thermoelectric materials including their resistance to high temperatures, low toxicity and their low costs, meaning they could potentially replace intermetallic materials. Whilst p-type oxide thermoelectric materials exhibit reasonable ZT values, n-type oxide materials, which are a partner for p-type oxide materials for thermoelectric modules, exhibit lower ZT values. Therefore in order to create modules with improved performance it is necessary to either improve the ZT values for existing materials or explore novel oxide materials with large ZT values.

Since the discovery of the highly performing p type material, $NaCo_2O_4$ in 1997 (Terasaki et al., 1997) cobalt oxides with hexagonal CoO_2 sheets similar to Na_xCoO_2 have been studied in terms of their thermoelectric performance (He et al., 2011). $NaCo_2O_4$ has high electrical

conductivity and high Seebeck coefficient, resulting in a very high power factor of 5000$Wm^{-1}K^{-2}$ (Li et al., 2010) and a ZT of around 0.7 to 0.8 at 1000K (Tritt and Subramanian, 2006). These materials have a complex structure known as a hybrid crystal, which can be thought of as made of nano blocks that contain different compositions, different structural symmetries and therefore different thermoelectric properties (*Figure 7*). The electrical and thermal transport properties, which are usually linked in many materials, are decoupled to some extent in this system and can be individually tuned to improve the overall ZT of the material. In Cobalt oxides, the CoO_2 nano blocks form nano sheets which possess a strongly correlated electron structure which serves as an electron transport structure. This leads to high power factors, whereas the disordered sodium or calcium colbalt oxide layers act as phonon scattering regions reducing thermal conductivities (Koumoto et al., 2006). This produces a material with low thermal conductivity and high electrical conductivity. The structure of Na_xCoO_2 is shown in *Figure 7*. The development of hybrid crystals or structures composed of periodic arrangements of layered nano sheets having different functions is a novel method for achieving improved thermoelectric performance.

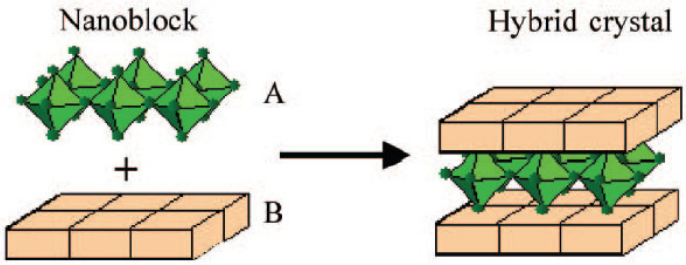

Figure 7: Structure of hybrid crystal (Koumoto et al., 2006)

The Seebeck coefficients of thermoelectric oxide materials based upon cobalt oxides such as Na_xCoO_2 and $Ca_3Co_4O_9$, have been found to be high, above 100 µV/K (Tahashi et al., 2010; Shikano and Funahashi, 2003). Promising p type thermoelectric properties have been found in calcium cobalt oxide. (Tahashi et al., 2010) fabricated calcium cobalt oxides from a base $Ca(OH)_2$ material using solid state reaction. They reported a high Seebeck coefficient of 160 mV/K at 873 K for sintering temperature of 1193 K and a power factor of 100 $Wm^{-1}K^{-2}$ at 873 K. After sintering at 1293 K, a very high Seebeck coefficient of greater than 600µV/K was

reported, however a large power factor was not obtained because the electrical resistivity was an order of magnitude different. Different properties were reported because the $Ca_3Co_4O_9$ decomposed into $Ca_3Co_2O_6$ at higher temperature. This is confirmed by (Sopicka-Lizer et al., 2005) who investigated the behaviour or $CaCO_3$ with different Ca:Co ratios after heat treating at different temperatures between 973K and 1373K. It was found that $Ca_3Co_4O_9$ decomposes and forms $Ca_3Co_2O_6$ around 1223K which is in agreement with the change in composition found by (Tahashi et al., 2010). This means that careful consideration of the thermal treatments is required to synthesise the material in order to achieve high thermoelectric performance and avoid the reduction in electrical conductivity which can have a large effect on the power factor of the material.

2.12. Skutterudites

The search for thermoelectric materials has discovered a promising group of materials known as skutterudites. These materials are prospective candidates for energy harvesting in the intermediate temperature range (Shi et al., 2011). A skutterudite has the general formula MX_3 where M is the transition metal Cobalt (Co), Rhodium (Rh), or Iridium (Ir), and X is phosphorous (P), Arsenic (As), or antimony (Sb) and crystallizes with the body centred cubic structure (Shi et al., 2011). A unit cell is made with 8 groups of MX_3 blocks (*Figure 8*), in this structure there are two large lattice voids surrounded by 12 X atoms which allow this structure to change the electronic and lattice properties (*Figure 9*).

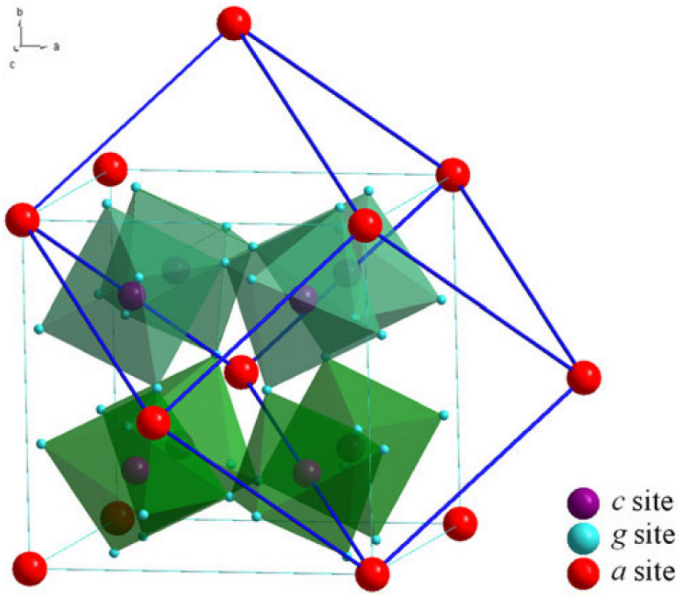

Figure 8: Crystal structure of a typical skutterudite material. Transition metal atoms, M occupy the 8c sites and X atoms occupy the 24g sites. Guest atoms could be filled into the voids at 2a sites (Shi et al., 2011).

Skutterudites have outstanding electrical properties with high carrier mobility, which is important for a high performing thermoelectric material, the thermal conductivity in unfilled skutterudites is too high for high thermoelectric efficiency. $CoSb_3$ for example has a high thermal conductivity of $10Wm^{-1}K^{-1}$ which prevents it from competing with state of the art Bi_2Te_3 which has a thermal conductivity of $1.0\text{-}1.5Wm^{-1}K^{-1}$ (Li et al., 2010). The voids in the lattice could be filled with a small metal guest atom, typically large mass interstitials such as rare earth elements (Nolasa et al., 2000) are chosen and since the voids are typically larger than most elemental ions, the filler is likely to "rattle" within the void. This reduces the thermal conductivity by introducing disorder into the lattice by the void filling atom which disrupts the propagation of phonons through the lattice. The more loosely bound ions rattle at lower frequency and are therefore more effective at disrupting the lower frequency, heat carrying phonons. Smaller and heavier ions in the void space mean a larger reduction of the lattice thermal conductivity (Nolasa et al., 2000). This concept was introduced by (Slack and Tsoukala, 1994), which proposed the ideal concept that high

efficiency thermoelectric materials should be a phonon-glass electron-crystal (PGEC) material. (Sales et al., 1996) reported $CoSb_3$ based Skutterites of $Ce_{0.9}Fe_3CoSb_{12}$ and $La_{0.9}Fe_3CoSb_{12}$ with a low thermal conductivity of 1.4 $Wm^{-1}K^{-1}$, which is one-seventh of that of unfilled $CoSb_3$, and a high *ZT* of greater than 1.0 which puts these materials in competition with Bi_2Te_3 materials.

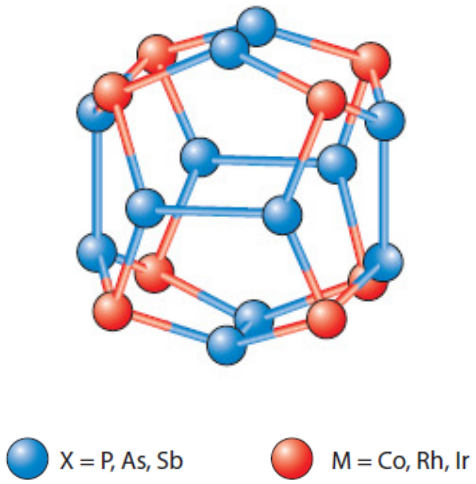

Figure 9: Structure of the M_8X_{12} dodecahedron void in the skutterudite unit cell (Li et al., 2010)

By adding atoms to the voids, the elements donate their valence electrons to the conduction bands of the material which can improve the electrical conductivity of the material but also pushes the material towards n type conduction with high electron concentration. P type conduction can be achieved by doping with electron deficient atoms at the M or X sites, ZT has been estimated to reach 1.3 for Fe substituted La filled skutterudites (p type) by (Sales et al., 1997). (Tang et al., 2005) investigated the properties of doped skutterudites of $R_yM_xCo_{4-x}Sb_{12}$ (x=0.0–3.0, y=0.0–0.7) where R = Ce, Ba, Y is the filler and M = Fe, Ni is the dopant to substitute onto a Co site. Both n and p type skutterudites with high performance were obtained. The p-type $Ce_{0.28}Fe_{1.5}Co_{2.5}Sb_{12}$ has a peak *ZT* of 1.1 at 750 K, and n-type $Ba_{0.30}Ni_{0.05}Co_{3.95}Sb_{12}$ showed a maximum *ZT* of 1.25 at 900 K. $CoSb_3$ shows much promise for thermoelectric applications because of the high thermoelectric performance in both n and p doped material. The ability to obtain both n

and p type doping in the same material means that the p and n type legs in a thermoelectric device are constructed of the same base material and have similar mechanical and thermal properties to minimise thermal stresses which can cause failure in a device.

2.13. Strontium titanate

Strontium titanate, $SrTiO_3$ is an n-type thermoelectric oxide which shows promise for harvesting thermal energy, it exhibits a high Seebeck coefficient which means a relatively large voltage can be generated for a given temperature difference (Muta et al., 2004). Because of the material's high melting point of 2080°C electron doped $SrTiO_3$ can be used at temperatures as high as 1000K without deterioration. $SrTiO_3$ is a metal oxide, its precursor materials are non-toxic and abundant in natural resources meaning that there are reduced environmental issues regarding the materials used. The electrical conductivity can be controlled by substitutional doping, for example lanthanum, La^{3+} can be substituted in place of strontium, Sr (Muta et al., 2004) and niobium, Nb^{5+} can be substituted in place of titanium, Ti in the material. This has the effect of increasing the electrical conductivity while only making small changes to thermal conductivity thus improving the figure of merit.

It has been reported that La doped $SrTiO_3$ has a power factor comparable to those of commercial materials such as Bi_2Te_3 alloys (Liu et al., 2010), which are used in many thermoelectric devices. However, because $SrTiO_3$ has a relatively high thermal conductivity, it does not exhibit high enough performance for practical applications (Liu et al., 2010). Therefore to improve the ZT value of $SrTiO_3$ it is essential to reduce the thermal conductivity without reducing the $S^2.\sigma$ value (Ohta, 2007). (Muta et al., 2004) have reported that substitution of Sr^{2+} with Ca^{2+} or Ba^{2+} is a good way to reduce the thermal conductivity of $SrTiO_3$, however, this also decreases the power factor. This indicates that on occasion substitution lowers the thermoelectric performance. Work carried out by (Shang et al., 2011) revealed that doping $SrTiO_3$ with La not only improves the electrical conductivity but lowers the thermal conductivity of bulk $SrTiO_3$, this double effect gives an improvement to the overall thermoelectric performance of $SrTiO_3$. Other dopants have also been investigated, (Muta et al., 2003) for example used rare earth doping with yttrium Y,

lanthanum La, samarium Sm, gadolinium Gd and dysprosium Dy. They discovered that the thermal conductivity of the material decreased with increasing ionic rare earth radii due to an increase in phonon-impurity scattering. Dy doping produced the highest figure of merit of 2.2.

While doping of $SrTiO_3$ gives promising results by improving electric conductivity a reduction process is also required, whereby the oxygen content of the material is reduced (Marina et al., 2002). Usually this is undertaken in a reducing atmosphere, for example, Savaniu (Savaniu and Irvine, 2009) used a 5% hydrogen in argon. The material was heated in this atmosphere and the hydrogen reacted with the only oxygen available, which is contained in the $SrTiO_3$ powder to form H_2O which was carried away by the flowing atmosphere. (Yu et al., 2008) Investigated the reduction of thermal conductivity in oxygen deficient $SrTiO_3$ where $La_xSr_{1-x}TiO_{3-d}$ films were grown in an oxygen deficient environment. A marked decrease in the thermal conductivity of the films was discovered which is of benefit to improving the ZT of the films. (Savaniu and Irvine, 2009) also investigated the effects of sintering La doped $SrTiO_3$ in reducing atmosphere; reduction studies were carried out on La doped $SrTiO_3$ at 900°C in a 5% H_2 in Ar atmosphere for 12 hours. They discovered that the electrical conductivity of the reduced material is higher than that of un-doped material. Reducing the oxygen content has the effect of transforming the Ti^{4+} to Ti^{3+} which improves the electrical conductivity of the material. The reduction becomes accentuated above 1000°C, meaning the removal of oxygen becomes much greater.

Heat treatment of $SrTiO_3$ in reducing conditions can form oxygen vacancies and therefore inject electrons into the conduction band which improves the electrical conductivity. However, the thermal conductivity of the oxide can also be high because of the simple crystal structure of the material and the light atomic mass of the constituence which limits the figure of merit, ZT to between 0.1 and 0.2. Thin films have been made and demonstrated ZT = 0.37 for 20% Nb $SrTiO_3$ film. The major drawback of $SrTiO_3$ based oxides is that reducing conditions are necessary for n-type doping. High temperatures in an oxygen containing environment will remove the carriers from the conduction band which leads to the oxide only being suitable for applications in an oxygen free environment. Practical use

will require measures to protect the oxide from oxidising using anti-oxidizing surface protection such as paint or polymer coating.

2.14. Calcium Manganese Oxide

While $SrTiO_3$ is a promising thermoelectric oxide, there are other materials which are also promising, Calcium manganese oxide for example. $CaMnO_3$ like $SrTiO_3$ is an oxide, and two dopants commonly used with $CaMnO_3$ are ytterbium which enters the calcium site and niobium on the manganese site (Park et al., 2009). Doping with ytterbium has advantages over doping with niobium such as higher electrical conductivity and Seebeck coefficient resulting in larger thermoelectric figure of merit. Some dopants such as lanthanum tend to increase electrical conductivity while other dopants such as praseodymium tend to reduce the thermal conductivity. The difference in properties of different dopants provides opportunities to selectively co-dope to obtain a material with tuned thermoelectric properties. For example dysprosium increases electrical conductivity in combination with ytterbium, which decreases thermal conductivity is an effective combination.

2.15. Zinc oxide

Zinc oxide is a wide band gap semiconductor with high electron mobility and thermal conductivity (Han et al., 2014). ZnO crystallises in the wurzite structure at ambient pressure and temperature, this is a hexagonal lattice with each Zn ion surrounded by four O^{2-} ions in a tetrahedral configuration and vice versa (*Figure 10*) (Ruoho, 2012). ZnO is intrinsically an n-type semiconductor and it is believed that native defects such as Zn interstitials and O vacancies (Coleman and Jagadish, 2006) are thought to compensate the donors and give rise to the native conductivity.

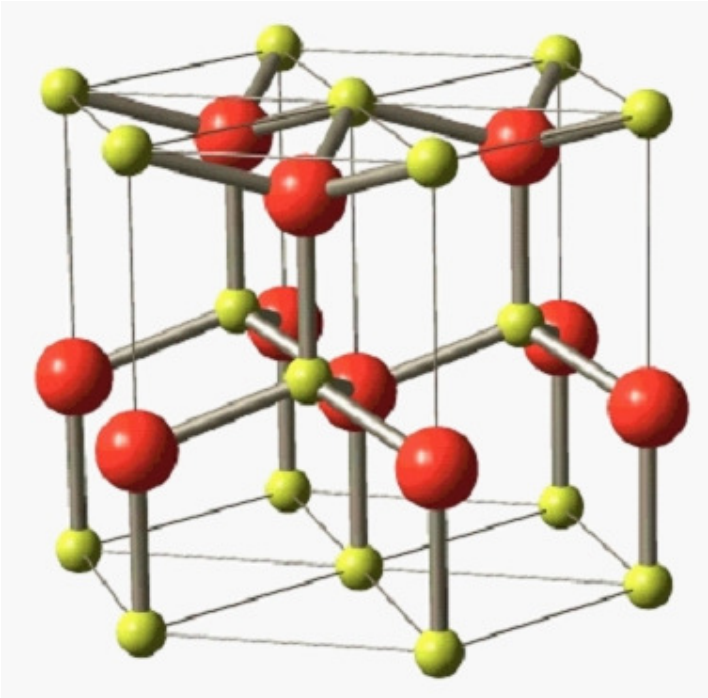

Figure 10: Crystal structure of ZnO (Wurzite structure) (Onodera and Takesada, 2012)

Al is the most common n-type dopant for ZnO, but In, Ga, Ti, Mo, Nb, Cu, Ge and Ca have also been studied (Ruoho, 2012). The high thermal conductivity of ZnO systems has kept the thermoelectric performance of Al- doped ZnO at a low level of ZT = 0.3 at 1000°C (Ohtaki et al., 2009). The thermoelectric properties of Al doped ZnO were investigated (Tsubota et al.,

1997) and it was found that there is a solubility limit for Al in ZnO of less than 0.5at. % which is thought to also limit the ZT value, however the thermal conductivity increased until 2.0at.%, and a maximum ZT value of 0.3 at 1000°C was found for $Al_{0.02}Zn_{0.98}O$.

Various attempts have been undertaken to try and improve the ZT values of n-doped ZnO by duel doping ZnO with Al and Ga. The inclusion of Ga in the structure through subsitutional doping reduces the thermal conductivity of the bulk material in order to improve the performance (Ohtaki et al., 2009). Ohtaki experimented with dual doping ZnO with Al and Ga by the mixed oxide synthesis, a Ga inclusion of 2.0mol% was enough to halve the thermal conductivity of Al - ZnO, reducing it from 40 $W.m^{-1}.K^{-1}$ for $Zn_{0.98}Al_{0.02}O$ to 13 $W.m^{-1}.K^{-1}$ for $Zn_{0.96}Al_{0.02}Ga_{0.02}O$. This value was further decreased with increasing Ga content. A drawback of this is that the inclusion of Ga into the material also decreases the electric conductivity by as much as to turn the electric conductivity of the material from metallic to semiconducting at a Ga content of ≥ 0.4 mol. %. However, the decrease in electrical conductivity was found to be relatively small for lower Ga content of < 0.4 mol. %. This also significantly enhanced the Seebeck coefficient for materials containing Ga with the highest performing material, $Zn_{0.96}Al_{0.02}Ga_{0.02}O$ with a ZT of 0.65 at 974°C

P-type doping with elements such as Li, Na, K, Ag, N, P and As have been studied (Claflin et al., 2006) but because of the natural intrinsic n-type character of ZnO, p-type doping is difficult to achieve. Of the group V dopants, (N, P, As and Sb), N is the most promising and commonly used p- type dopant. N behaves as an acceptor in the ZnO system and substitutes for O (Claflin et al., 2006). Its ionic radius is similar to that of O which allows for easy substitution. Other group V elements have much larger atomic radii than the O atom. The large size mismatch causes distortions in the lattice and low solubility. For As and Sb, (Limpijumnong et al., 2004) suggested that p- type conduction could result from shallow defects where an As or Sb atom occupies a Zn site, resulting in acceptor behaviour from the formation of a complex with two zinc vacancies. Doping with group I elements such as Li and Na have theoretically been shown to be shallow acceptors, substituting on the Zn site but Li and Na interstitials behave as donors and completely compensate the p-type

contributions (Yamamoto and Katayama-Yoshida, 1999). One of the main issues currently limiting the production of ZnO-based devices is that of achieving p-type ZnO. It has been suggested that low solubility of dopants within this material could be responsible for the difficulty in achieving p-type behaviour. Improvements in the as-grown quality of ZnO material, as well as successes with dopant atoms, indicate that p-type doping of ZnO is an achievable goal (Coleman and Jagadish, 2006).

2.15.1. Al doped ZnO

Al doped ZnO is a promising oxide material for thermoelectric energy conversion due to its chemical stability, high Seebeck coefficient of over -100μV.K^{-1} (Ohtaki et al., 2009), high power factor, and high electrical conductivity (Jantrasee et al., 2014). Doping ZnO with Al at a carefully selected concentration results in high power factors due to its excellent charge carrier properties (Han et al., 2014), and since the report that the thermoelectric performance of Al doped ZnO becomes maximum at composition x=0.02 in $Zn_{x-1}Al_xO$ (Tsubota et al., 1997), Al doped ZnO has shown promising thermoelectric performance, with ZT of 0.2 at 800°C (Jantrasee et al., 2014). Al doped ZnO is a degenerate semiconductor and demonstrates properties that are more metal-like than semiconductor-like with the electrical resistivity being proportional to the temperature (Pradhan et al., 2014).

Al doped ZnO suffers a high thermal conductivity of ~5W.m^{-1}.K^{-1} at operating temperature (Jood et al., 2011) which limits its thermoelectric performance, however the performance is one of the highest of n type thermoelectric oxides.

Although ZnO has a high thermal conductivity compared to other oxide thermoelectric materials, the thermal conductivity is dominated by the lattice and therefore improvements to the overall ZT can be made by reducing the lattice thermal conductivity without seriously affecting the electrical properties. (Ohtaki et al., 2009) successfully introduced nanovoids into the densely sintered structure of Al-doped ZnO matrix to suppress the thermal conductivity (κ) of the material. This was carried out by mixing combustible nanosized polymer particles into the powder before sintering. This resulted in improvements to the power factor which improved the maximum ZT value of the material to ~0.6 at 1247 K.

While this method yielded promising results, experimental difficulties in obtaining a well dispersed nanovoid structure within the material caused insufficient reliability of sample performance (Ohtaki et al., 2009).

One method in which the thermal conductivity can be reduced is by carefully modifying the microstructure to introduce phonon scattering sites. Jood et al. (Jood et al., 2011) enhanced the phonon scattering in Al doped ZnO through grain refinement by synthesising Al doped ZnO nano-sized crystals by microwave activated thermal decomposition of zinc and aluminium acetates in pentanediol. The nanocrystals were then cold pressed and sintered in air at 950°C. The overall effect reduced the thermal conductivity to as low as 1.5 $W.m^{-1}.K^{-1}$ at 300K for an Al dopant level of 2.0at.%. It was also found that Al doping restricts the size of the nanocrystals, and inhibits the grain growth during sintering. The overall effect of bulk nanocomposites enhanced ZT to ~0.44 which is 50% higher than the best non-nanostructured counterpart material at the same temperature. Han et al. (Han et al., 2014) achieved a ZT of 0.3 at 1223K through spark plasma sintering of Al doped ZnO nanoparticles. This figure for ZT was achieved partly due to a low thermal conductivity of 3.2 $W.m^{-1}.K^{-1}$ due to the increased grain boundary and nanoprecipitate scattering of phonons in the material. A high Seebeck coefficient greater than -200$\mu V.K^{-1}$ resulted in a power factor of 7.97×10^{-4} $W.m^{-1}.K^{-2}$ at 1223K. This means that the microstructure of the material can improve the thermoelectric properties by introducing scattering sites into the material.

2.16. Novel materials

Much interest in thermoelectrics stems from the evidence of enhanced ZT through nanostructured thin films and wires due to the enhanced Seebeck and reduction of thermal conductivity. High ZT values of above 2 have been reported in thin films but difficulty in obtaining reliable measurements makes them difficult to reproduce in independent laboratories (Snyder and Toberer, 2008). Before high ZT devices can be realised with thin film technology, improvements to both the electrical and thermal contacts of the thin film materials in a device are needed. The use of bulk nanostructured materials has advantages over thin film alternatives in that the bulk material avoids detrimental thermal and electrical losses. The main issue to overcome in bulk nanostructured system is avoiding electrical losses through electron scattering from random oriented grains in the sintered material.

To develop thermoelectric materials with improved performance requires tuning of the interconnected material properties of Seebeck coefficient, S, electrical conductivity, σ, and thermal conductivity, κ. Nanostructures provide an ability to partially disconnect the linkage between the thermal and electrical transport properties by introducing new scattering mechanisms for improving the thermoelectric performance (Li et al., 2010). Single crystals usually provide the best electrical conductivity due to the absence of grain boundaries and interfaces which scatter charge carriers. The only way of improving the ZT values of single crystal materials is by adjusting the charge carrier concentration which can be achieved through doping.

By reducing the dimensions, the thermoelectric parameters can be individually tuned for a single piece of material. When the size approaches the scale of the mean free path of the electrons in the material in any direction, the density of states increases due to quantum confinement, which results in an increase in the Seebeck coefficient. The thermal conductivity of the material is also reduced because the phonons are scattered at the surface due to the dimensions being smaller than the average mean free path of the phonons. The thermal conductivity of a monolith can also be reduced by introducing grain boundaries and interfaces into the structure which act as scattering sites for phonons. However, the improvements to the thermal conductivity will tend to reduce the electrical

conductivity because phonon scattering sites will also scatter charge carriers. Phonons and electrons have different mean-free paths and therefore it is possible to reduce the thermal conductivity while minimising effects to electrical conduction by careful tuning of scattering conditions within the material. A micro – nano mixed grain composite material may offer an improved trade off as the nano grain network will be effective at reducing the thermal conductivity while the micro grains form a network to allow charge carriers to pass through (Li et al., 2010).

2.17. Characterisation

Accurate measurement and reliable characterisation of electrical and thermal properties of thermoelectric materials poses many challenges (Ruoho, 2012). At present the diversity of apparatus design, methodology of data acquisition and measurement contact geometry has resulted in conflicting data that cause complications in comparing reported Seebeck coefficients between different laboratories (Martin, 2013). The measurement of surface temperature by physical contact can lead to thermal offsets, which can be found everywhere. Each measurement system has contacts between the external environment, the measurement probe, and the sample which risks thermal transfer from the environment influencing measured temperatures. The influence of thermal transfer can become greater at high temperatures and therefore it is necessary to reduce these effects.

For isotropic materials, the Seebeck coefficient is not geometrically dependent; however the arrangement of measurement probes may affect the results (Martin et al., 2010). There are two main probe arrangements for measuring the thermoelectric properties; two probe and four probe *Figure 11*. In two probe arrangement, the temperature difference and the voltage is measured on the probes which are in direct contact with the ends of the sample, in this arrangement improved thermal and electrical contact is achieved (Martin et al., 2010). However, where the electrical resistivity is also measured, additional voltage contacts located away from the ends of the sample are also required. In the four probe arrangement, the temperature difference and the voltage difference are measured at two points, either

on the sample or within the sample, equidistant from the hot and cold ends of the sample and parallel to the thermal gradient.

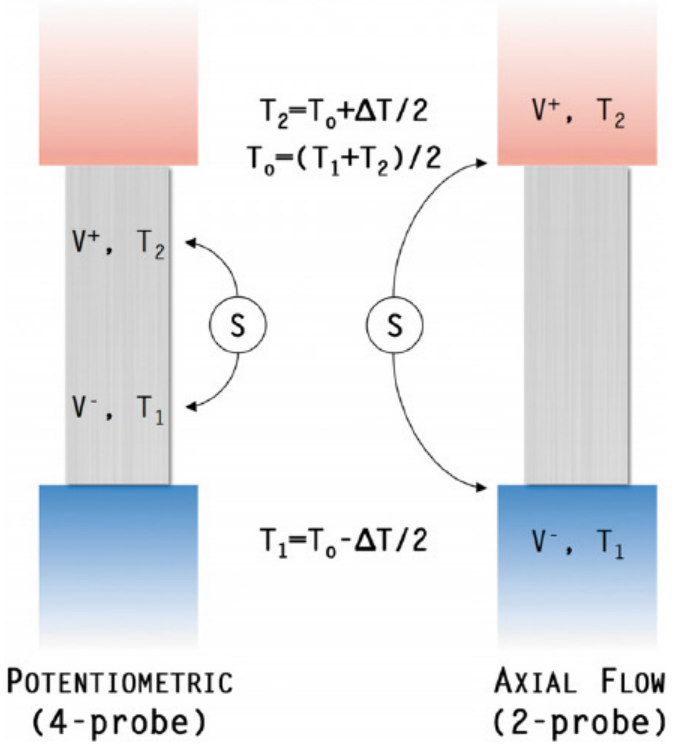

Figure 11: Diagram comparing four probe and two probe measurement arrangements (Martin et al., 2010)

Comparing the findings of different authors is difficult due to poor estimations of uncertainty, inconsistencies in sample mounting setup, lack of information regarding the temperature difference used at different temperatures, method of measuring the thermoelectric properties, and lack of detail in measurement apparatus setup.

Measurement of the Seebeck coefficient, where thermocouple probes are used, require a number of voltage measurements; one each for the thermocouple voltages, usually two are used, one for the hot and one for the cold thermocouple voltage, T_2 and T_1 respectively, which are used to determine the temperature difference across the sample, ΔT. The measurement of the voltage and the temperature must be carried out in the same location on the sample and at the same time, the interfaces between the measurement system and

the sample must be Ohmic and isothermal, the measurement of small voltages must be carried out with minimum external sources of interference.

Any probe contact to measure either the temperature or electrical properties of the material under test will have the effect of causing heat sink/reservoir effects; also the placement of measurement probes is essential to the accuracy of any measurement. Ideally the electrical properties of the material will be conducted in the same location as the temperature probe at precisely the same time in order to avoid measurements discrepancies arising from time dependent drifting. This is often done on the same probes; the electrical measurements conducted using the contacts made by the temperature probes. Also the contact between the probes and the surface of the sample must be carefully arranged. The measurement probe must make ohmic contact with the material in order to obtain reliable data. Often a metal-ceramic interface forms an insulating barrier. Because probes have a thickness, it is important to take this into account for high precision readings, the temperature is measured from the centre of tip of the probe whereas the electrical measurements will be measured from the edge of the probe. It is important to thermally isolate the material from the environment in order for the heat flow to be from the heat source to heat sink without any thermal effects induced from external sources. This is usually done by conducting the measurement in a vacuum.

(Zhou and Uher, 2005) designed an apparatus for the measurement of Seebeck coefficient and electrical resistance measurement at high temperatures of 300°C -1000°C. For Seebeck measurement, two independent heaters are set at different temperatures and the potential difference between two points along the thermal gradient is measured. The temperatures at these points are simultaneously recorded and the Seebeck coefficient can be calculated from the resulting temperature difference and voltage.

The electrical resistance is measured by setting both heaters to the same temperature so no thermal gradient is present along the sample; a 4 point probe is then used in AC mode to measure the electrical resistance of the sample. AC is used so that resistances caused by contact effects are neglected.

There are two main techniques to measure the Seebeck coefficient, integral and differential (Martin et al., 2010). In the integral approach, one end of the sample being analysed is held at a fixed temperature, T_1 while the other end is varied through a range of temperatures $T_2=T_1+\Delta T$. This method measures the voltage produced over a large ΔT with the advantage that the only one temperature requires varying which may simplify apparatus design. The differential method measures the voltage produced over a small thermal gradient ΔT. The sample is maintained at an average temperature of $T_0=(T_1+T_2)/2$ while the voltage potential is measured over a range of thermal gradients. This gives a Seebeck coefficient of ratio of potential/temperature gradient, *Figure 12*.

There are three categories of thermoelectric measurement, steady state, quasi steady state, and transient (Martin et al., 2010). Under steady state conditions, the temperature of each end of the sample is kept constant, and no thermal fluctuations are present the Seebeck coefficient is usually calculated from a linear fit of a range of electric potential and temperature measurements. This avoids the assumption that the curves intercept the point ($\Delta V=0$, $\Delta T=0$), and eliminates any offset which may arise due to in-homogeneities and contact discrepancies. A disadvantage of the steady state measurement is that it is necessary to wait for stabilisation after every ΔT increment which can increase the time required for sample analysis. The quasi steady state method is a faster measurement process. The heat flux is increased constantly while the voltage and temperature is measured simultaneously, rather than discreet, steady state temperature steps. The disadvantage in this method is that thermal drifts can occur when switching between measurement channels, resulting in the temperature and voltage readings becoming affected. This drift is proportional to the temperature profile of the system for the duration of the measurement time. In order to avoid this, high impedance meters can be used.

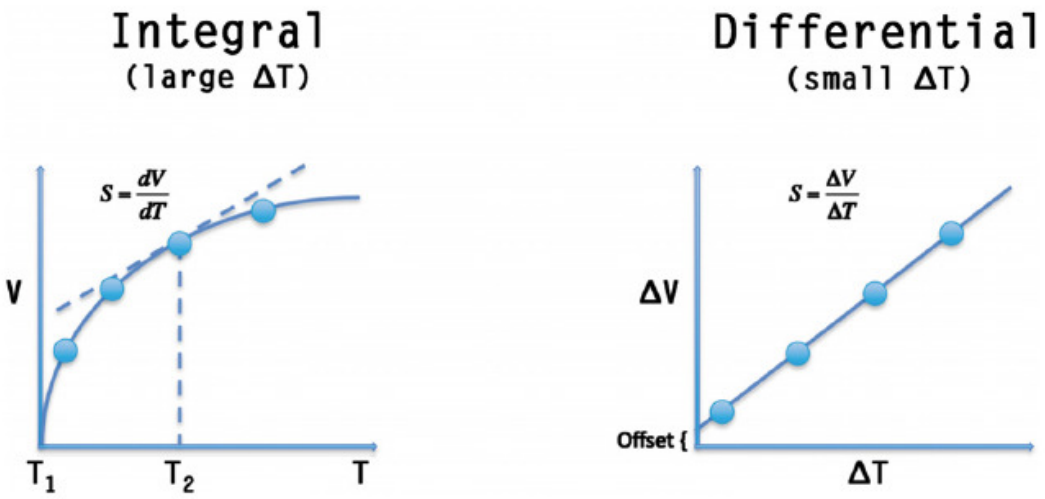

Figure 12: Two main techniques to measure the Seebeck coefficient (Martin et al., 2010)

3. Method

3.1. Introduction

In this chapter, a description of the experimental procedures used during this project is given. The first part of this chapter focuses on the synthesis of the doped material, followed by the method used to sinter the material as well as preparations for analysis. The characterisation of the doped ZnO and $SrTiO_3$ compacts is then explained.

3.2. ZnO synthesis

Powders were prepared by the mixed oxide route. Aluminium oxide (Al_2O_3) (≥98% purity – Sigma Aldrich), and antimony oxide (Sb_2O_3) (99% purity – Sigma Aldrich) were used as sources for the Al and Sb dopants for the n- and p- type ZnO, respectively. ZnO powders with dopant concentrations of 0.5at.% - 1.5at.% Al content, and 0.2at.% -1.0at.% Sb content were prepared by mixing the required amounts of Al_2O_3 or Sb_2O_3 with ZnO by ball milling in deionised water with zirconia milling media for 60 hours in polyethylene milling bottles. A ratio of 250 ml water : 100g reagents : 250g milling media was used. After milling, the resulting slurry was separated from the milling media and dried for 12 hours at 80-90°C. The resulting powder was then transferred to an alumina crucible and placed in an air furnace where the temperature was increased at a rate of 6°C/min to a hold temperature of 800°C for 4 hours. The powders were allowed to cool naturally in the furnace to a temperature safe for removal, typically 150-200°C. After thermal treatment, the powders were mechanically crushed with a pestle and mortar to break up any large agglomerates.

Pellets were created by placing 5 grams of powder into a cylindrical die with a diameter of 30mm where a pressure of 28MPa was applied and held for 30 seconds. The pellets were sintered in air at between 1000°C and 1300°C for 8 hours. The temperature was increased at a rate of 6°C/min to the designated sintering temperature.

After sintering, the pellets were wet polished with silicon carbide paper (P400) to remove the surface impurities and to produce a flat and smooth surface for electrical and thermal analysis.

3.3. Analysis

3.3.1. SEM

Cross sections of sintered pellets were prepared by mechanically fracturing the compact to reveal the internal microstructure. Polished cross sections of the sintered pellets were also prepared. This reveals the internal structure of the material by a polishing procedure that reveals a cross section of the material through grains and defects. This allows grain shape and size as well as the pore structure of the sintered compacts to be characterised. Analysis was carried out in gaseous secondary electron mode (GSE) to observe the microstructure of the cross section area of the prepared samples.

3.3.2. XRD

The phase composition of the samples was determined by XRD (Siemens 5005) with Cu Kα source. The diffraction patterns were measured in the 2θ range for 20° to 80°. Crystal peaks were identified using the supplied database.

3.3.3. Electrical resistivity

The electrical resistivities of the compacts were measured using the four point probe technique where a current is applied across the external two probes and the voltage measured across the internal two probes. The applied current was varied between -100 and 100 μA in 20μA steps and the corresponding voltage measured. The electrical resistivity, ρ of the pellets was calculated from the I/V curve with corrections made for the geometry of the electrical field through the thickness of the material, using equation *(8)*. These measurements were repeated six times at different locations across the surface of each pellet in order to obtain statistically relevant data.

$$\rho = \frac{V}{I} \frac{\pi t}{\ln\left(\frac{\sinh\left(\frac{t}{s}\right)}{\sinh\left(\frac{t}{2s}\right)}\right)} \qquad (8)$$

Calculation of resistivity of the sintered material was carried out using *Equation (8)* where ρ is the resistivity, V is the measured voltage, I is the supplied current, t is the thickness of the sample, and s is the probe spacing.

3.3.4. Porosity

The densities of the sintered compacts were determined from measurements of sample mass and volume. The mass of each pellet was measured on a laboratory balance to three significant figures. The volume of the sintered compacts was calculated by the Archemedes method where the sintered compacts were submerged in deionised water and vacuum applied to draw the water into the pores within the compacts. The overall volume of the sintered compacts was then carried out by submerging the saturated compacts in water and measuring the liquid displaced. The change in mass of the pellet before and after filling the pores with water is related to the volume of water absorbed into the pores and therefore the volume of pores, assuming an open pore structure.

The theoretical maximum density of each Al and Sb doped material was calculated using atomic masses of ZnO, Al and Sb, assuming that the Al substituted on the Zn site and that the Sb substituted on the oxygen site. The theoretical maximum density was calculated for each synthesised material according to the level of dopant. It was also assumed that there was no change in the unit cell size or shape following substitution.

The volume fraction porosity for materials with closed pore structure, where the water was not able to penetrate the pores during the Archemedes method, was calculated by comparing the experimentally determined density to the theoretical maximum density calculated of the matrix material.

3.4. Thermoelectric characterisation

3.4.1. Bespoke characterisation rig

In order to evaluate the thermoelectric characteristics of the synthesised materials, a bespoke thermoelectric characterisation rig was constructed. The main components of the characterisation unit are a 100W heater to supply heat to one side of the test sample and a liquid cooling unit to remove heat from the opposite side of the sample and maintain a thermal gradient across the sample. The heater is controlled by a temperature controller using pulse width modulation to control the temperature of the hot plate to within ±1°C. In order to ensure a uniform temperature across each face of the sample, the heater and cooler were set into copper blocks.

3.4.2. Seebeck coefficient

To measure the Seebeck voltage, silver electrodes were painted onto both faces of the sintered compacts. The compacts were sandwiched between two copper foil squares connected to an electrical meter to measure the voltage generated. Two thermocouples, set into copper discs, were placed either side of the sample to measure the temperature at the hot and cold side of the samples. Temperature was recorded by means of a data logging circuit and the voltage recorded in parallel by a high precision electrical meter. The temperature of the hot plate was increased from 40°C in discreet steps of 10°C and measurements were conducted after the measured temperatures were reached and maintained a steady state. The recordings were taken at a rate of 4/sec over a period of 5 minutes to obtain statistically relevant readings and to confirm that the temperature did not drift.

3.4.3. Thermal conductivity

In order to calculate the thermal conductivity, κ_s of the sample materials, the heat flow, Q through the material with cross sectional area, A_s and the temperature gradient, $\Delta T/L_s$ must be known according to *equation (9)* where ΔT is the temperature difference across the material and L_s is the thickness of material

$$\kappa_s = \frac{Q/A_s}{\Delta T/L_s} \qquad (9)$$

In order to find the heat flow through the material, reference material with a known thermal conductivity is placed either side of the sample material and the temperature difference across each sample measured. The comparative cut bar method was used to calculate the thermal conductivity of the sintered compacts. The sample, two reference samples of known thermal conductivity, and thermocouples were arranged as shown in *Figure 13*.

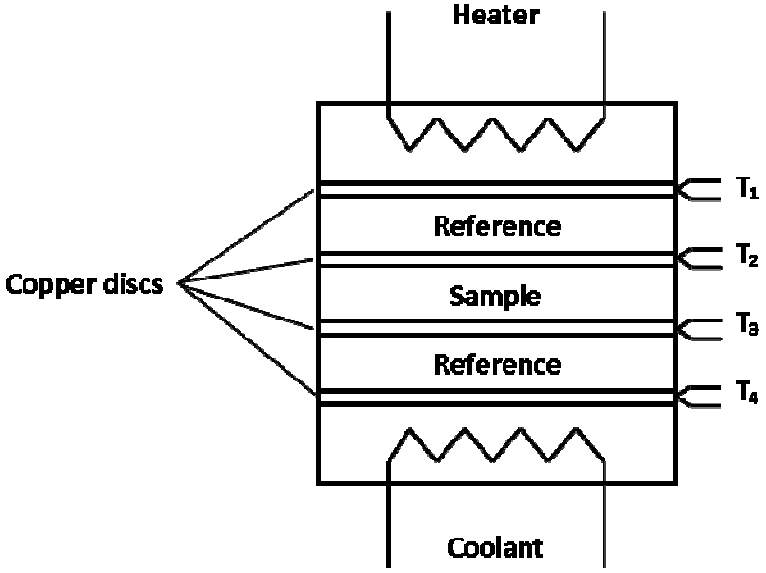

Figure 13. Diagram of the thermal conductivity measurement setup

The temperatures at the four locations were recorded by means of a data logger. The temperature of the heater was set and the temperature of the system left to settle before measurements took place to ensure steady state conditions.

To calculate the thermal conductivity of the sintered compacts, the heat flow through the reference materials were calculated from the temperature difference across each disc and the known thermal conductivity. The thermal conductivity of the sintered compacts were then calculated from the value of the heat flux through the material, see *equation (10).*

$$\frac{Q}{A} = K_s \frac{\Delta T_s}{L_s} = K_R \frac{\Delta T_1 + \Delta T_2}{2} \frac{1}{L_R} \qquad (10)$$

Where Q is the heat flux, A is the cross sectional area, K_s and K_R are the thermal conductivities of the sample and reference, respectively, and L_s and L_R are the thicknesses of the sample and reference, respectively.

4. Porosity dependent variables

4.1. Introduction

In this chapter the porosity of doped ZnO was studied and related to the level of doping and the sintering temperature. The crystallography of doped ZnO was also studied in order to determine the level of acceptance of dopant atoms into the ZnO system and the observations are linked to the porosity.

4.2. Sb dopant

Samples of antimony doped ZnO were prepared by the solid oxide route according to $ZnSb_xO_{(1-x)}$ from x = 0.000 to x = 0.010. After synthesising the powders, pellets were sintered at temperatures of 1000°C, 1100°C, 1200°C, and 1300°C.

In order to determine how the material changes with increasing Sb content, analysis was carried out using X-Ray Diffraction (XRD), the results of which are shown in *Figure 14* to *Figure 17* for samples sintered at 1000°C, 1100°C, 1200°C and 1300°C, respectively. Vertical lines indicating the relative intensities and position of the miller indices (hkl) peaks for undoped ZnO (pdf# 361451) are provided for clarity. There is also evidence of extra peaks in the XRD data, which correspond to peaks of a secondary phase of $Zn_7Sb_2O_{12}$ (pdf# 140613). Extra peaks in the XRD data corresponding to $Zn_7Sb_2O_{12}$ have also been seen in the literature, Park et al., for example (Park et al., 2008) detected extra peaks in XRD analysis of sintered samples of (1at.% - 5 at.%) Sb doped ZnO which correspond to $Zn_7Sb_2O_{12}$. Vertical lines indicating the relative intensities and positions of the (hkl) peaks of the secondary phase are also included.

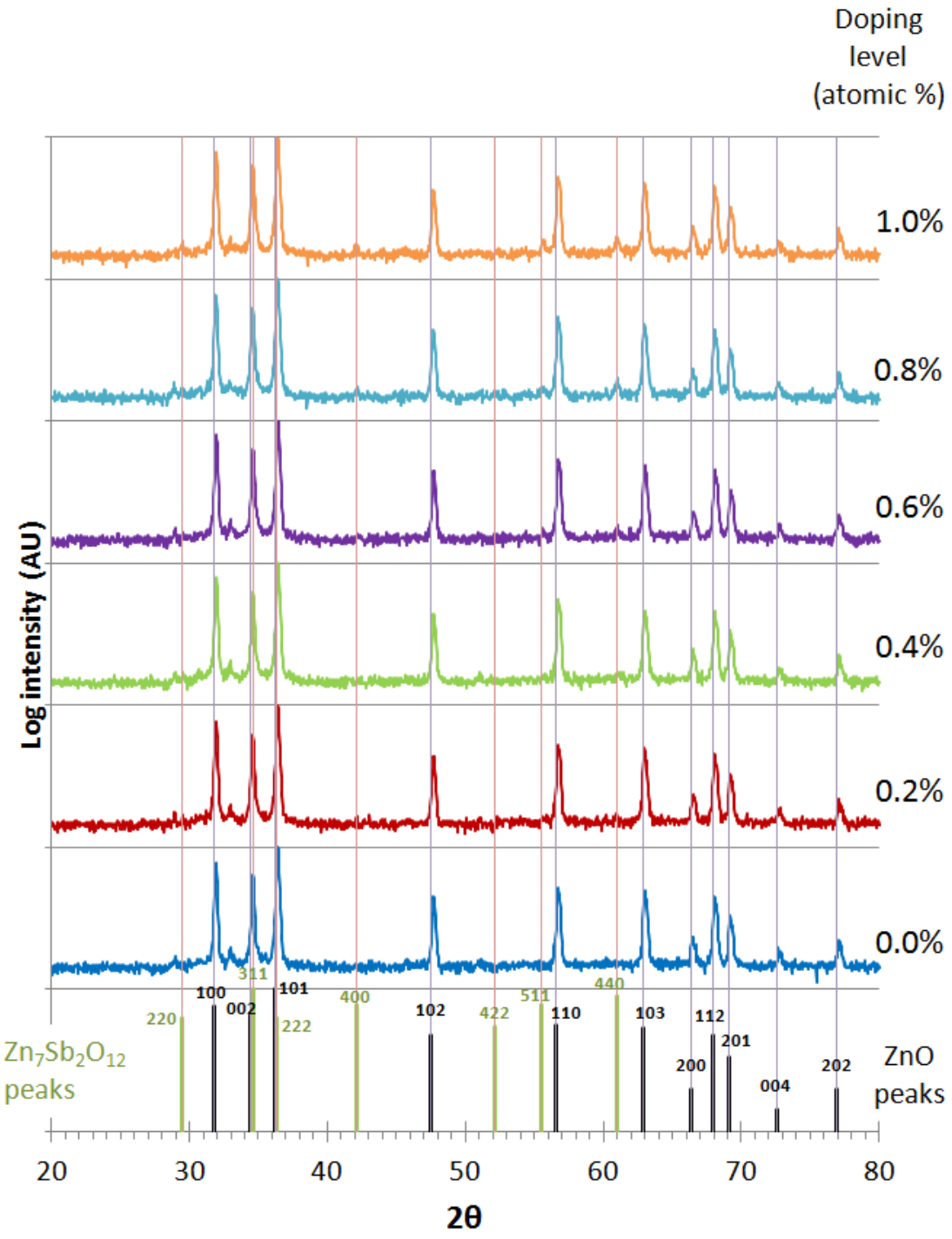

Figure 14: XRD analysis of Sb doped pellets sintered for 8 hours at 1000°C

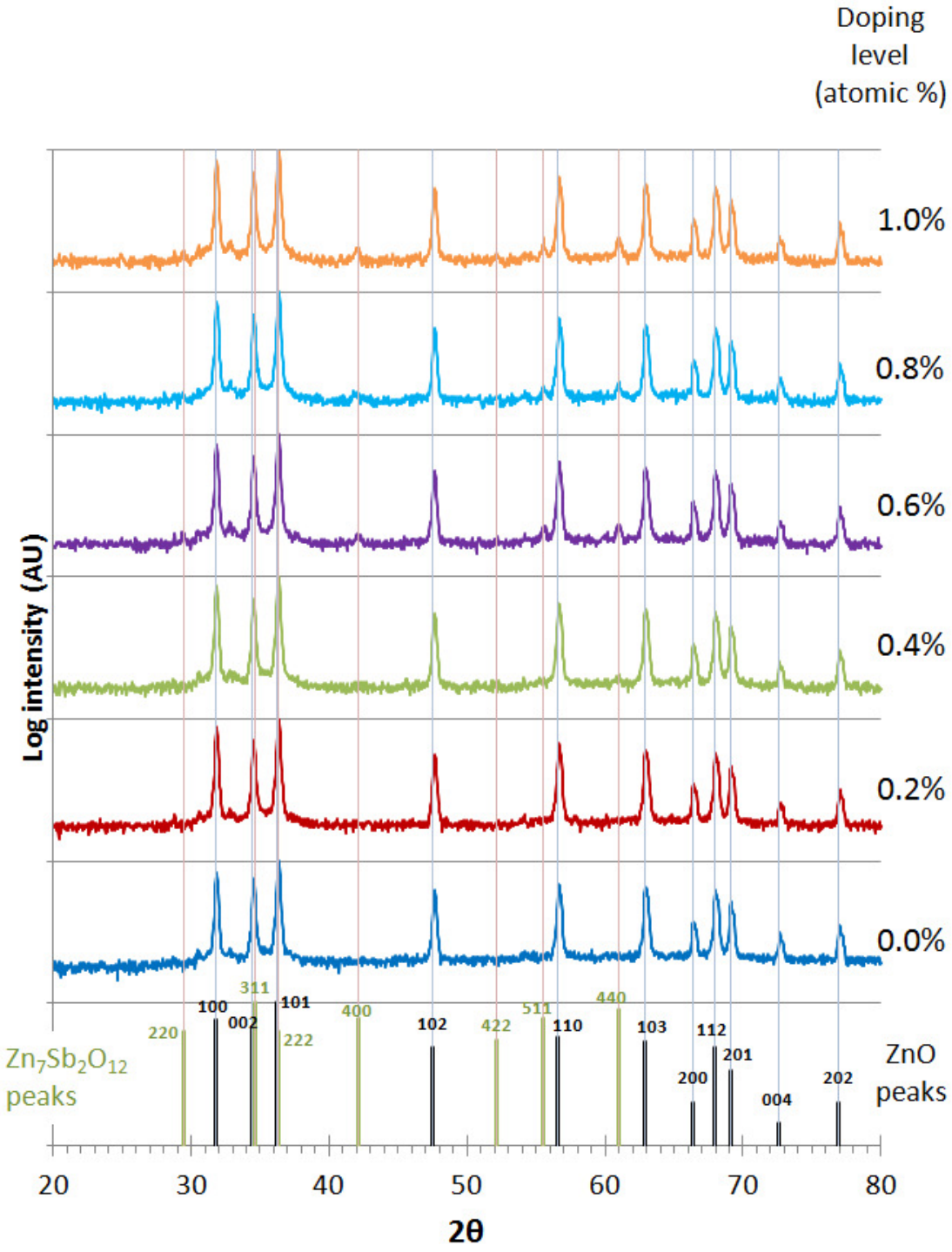

Figure 15: XRD analysis of Sb doped pellets sintered for 8 hours at 1100°C

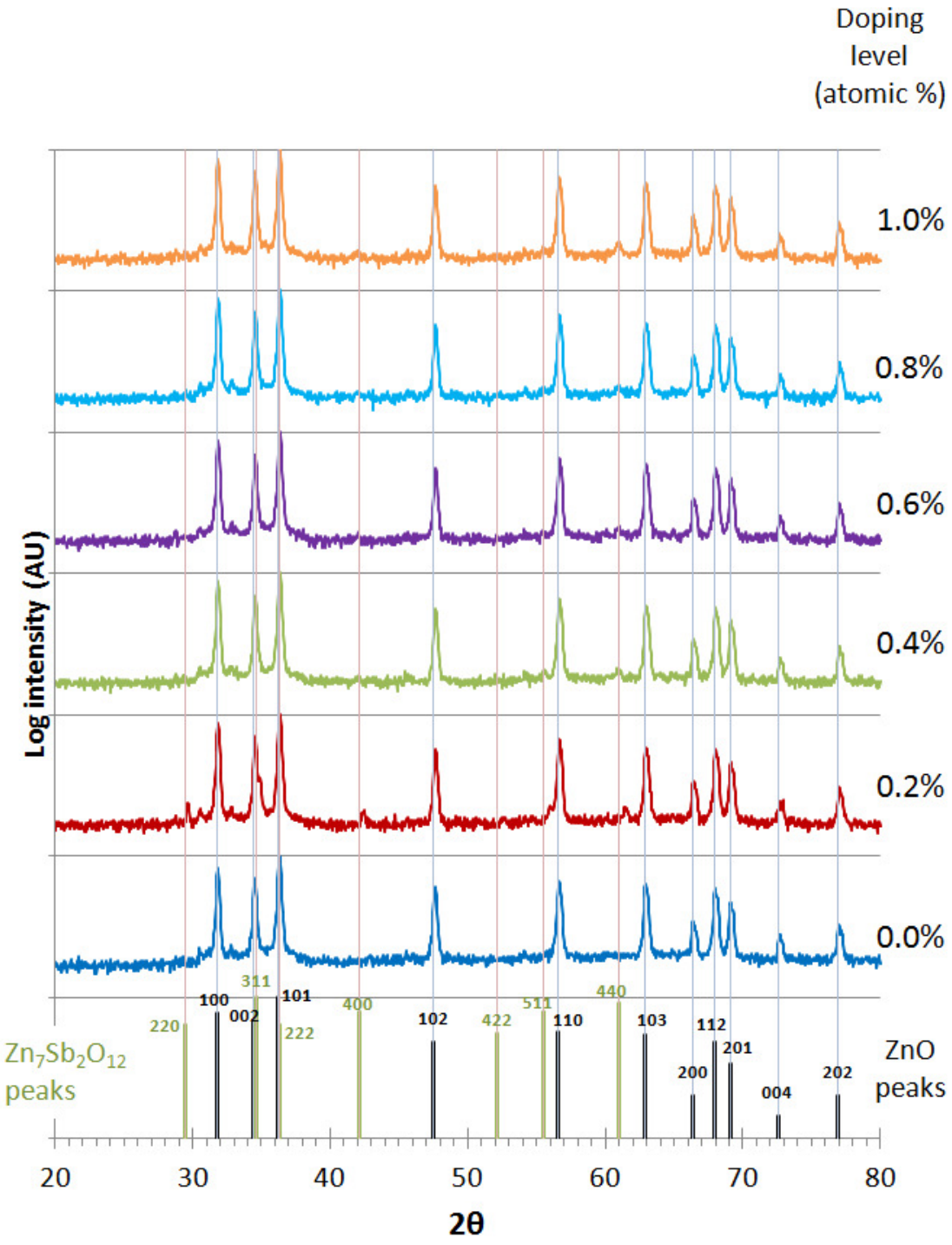

Figure 16: XRD analysis of Sb doped pellets sintered for 8 hours at 1200°C

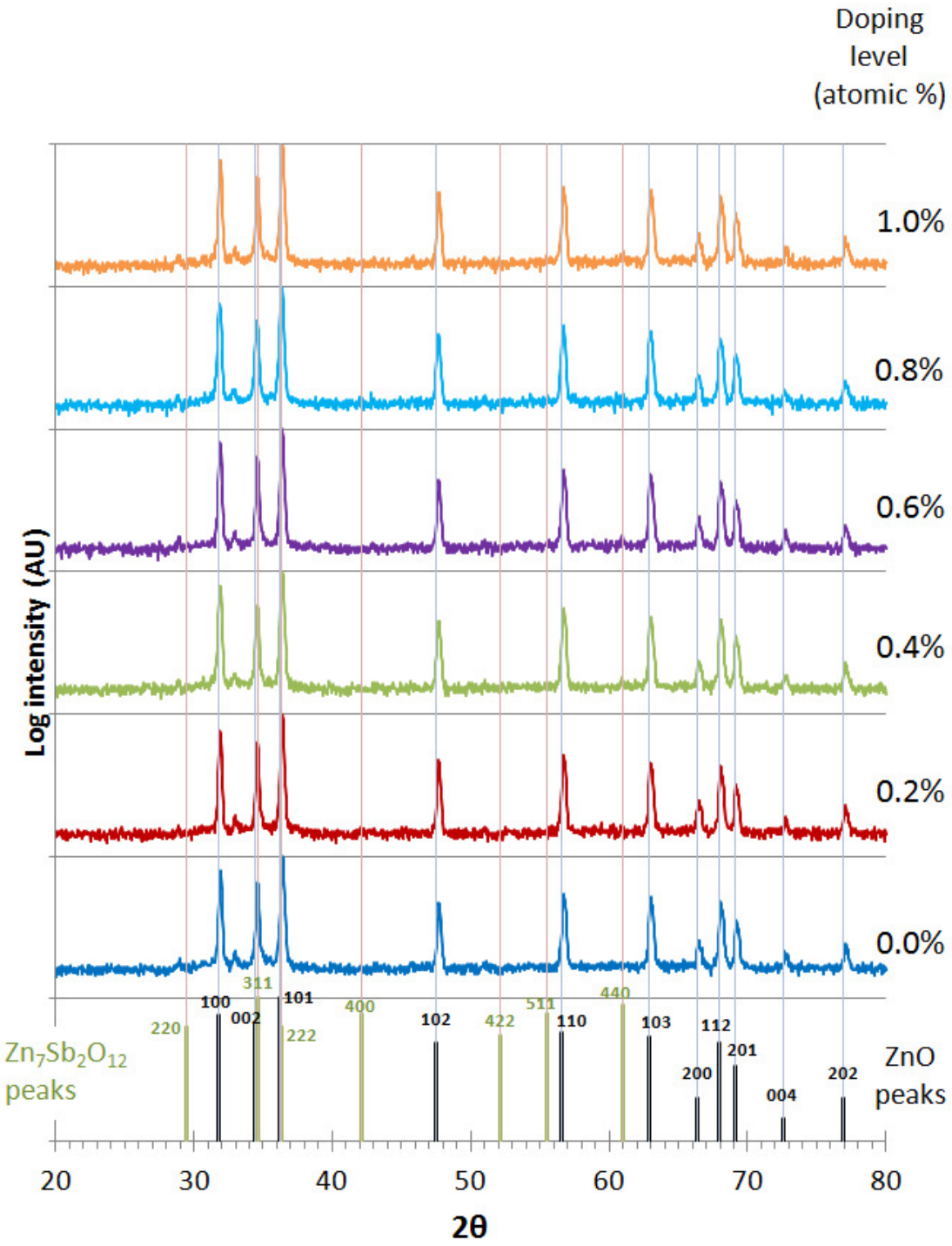

Figure 17: XRD analysis of Sb doped pellets sintered for 8 hours at 1300°C

4. Porosity dependent variables

The height of the XRD peaks of is related to the amount of the chemical phase, with higher peak intensity indicating a higher concentration of that phase. In order to determine if the amount of secondary phase is related to the doping level, the relative height of the (400) $Zn_7Sb_2O_{12}$ peaks of the secondary phase was calculated, and compared to the height of the (110) peak of ZnO as shown in *Figure 18*. The (440) peak of $Zn_7Sb_2O_{12}$ was chosen because it is the largest peak of the secondary phase on the XRD analysis, and the (110) peak of ZnO was chosen for comparison for relative height because it does not overlap with any other peaks which would cause interference issues.

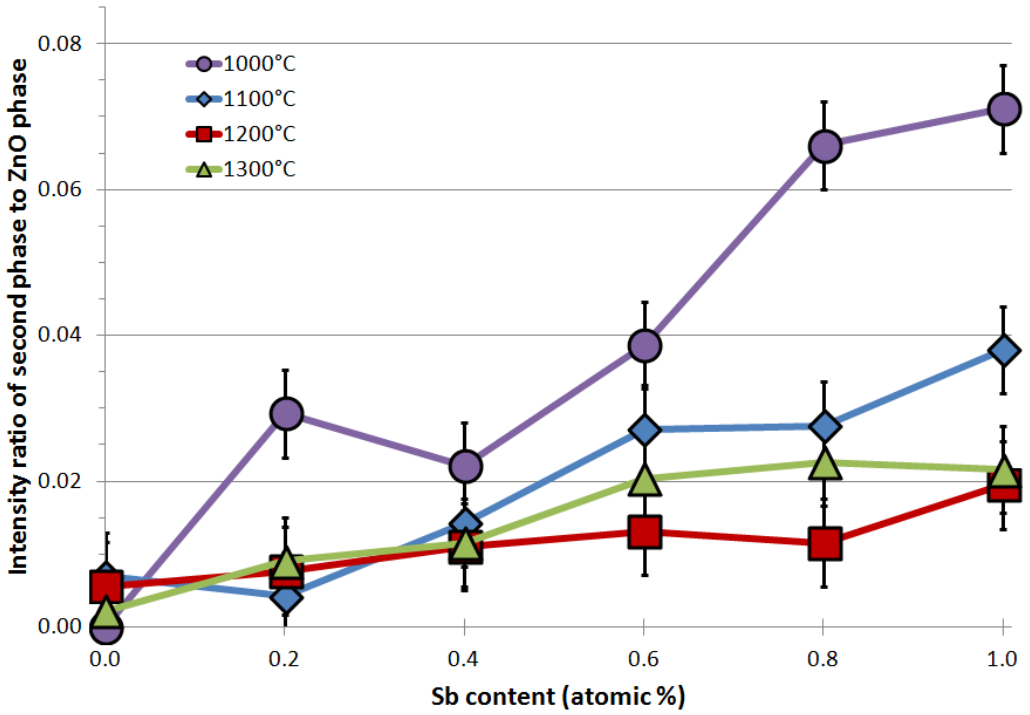

Figure 18: Relative intensity of the (440) peak of $Zn_7Sb_2O_{12}$ compared to the (110) peak of ZnO for samples of 0.0at.% to 1.0at.% Sb doped ZnO sintered for 8 hours at 1000°C, 1100°C, 1200°C, and 1300°C

The relative intensity ratio of the second phase to ZnO phase is shown in *Figure 18* as a function of Sb content. The error bars represent the error associated with the XRD measurement. There is a general trend that the relative intensity ratio of the second phase

to ZnO phase increases with increasing Sb doping level. This indicates that there is an increase in the amount of secondary phase present within the material as the amount of Sb dopant is increased. This was also observed by Park (Park et al., 2008) who found that the intensity of $Zn_7Sb_2O_{12}$ became stronger with increasing Sb content.

In order to determine if the porosities of the sintered ZnO pellets are affected by the level of Sb content, the density of the pellets were calculated using mass volume technique. The densities of $ZnSb_xO_{1-x}$ ($0.000<x<0.010$) pellets sintered for 8 hours at 1000°C, 1100°C, 1200°C and 1300°C are shown in *Figure 19* as a function of Sb content. The maximum theoretical density of the Sb–doped ZnO material was calculated by assuming that Sb substitutes on the O sites in the ZnO lattice and that the unit cell volume remained unchanged. This assumption was made on the basis that group V elements substitute onto the oxygen site in the ZnO system (Fan et al., 2013a) and the position of the XRD peaks (*Figure 14* - *Figure 17*) did not change with the increase in Sb levels which indicates the bond length, and therefore cell volume, remains unchanged. The theoretical maximum density possible is shown in *Figure 19* alongside the experimentally determined densities of the Sb doped ZnO.

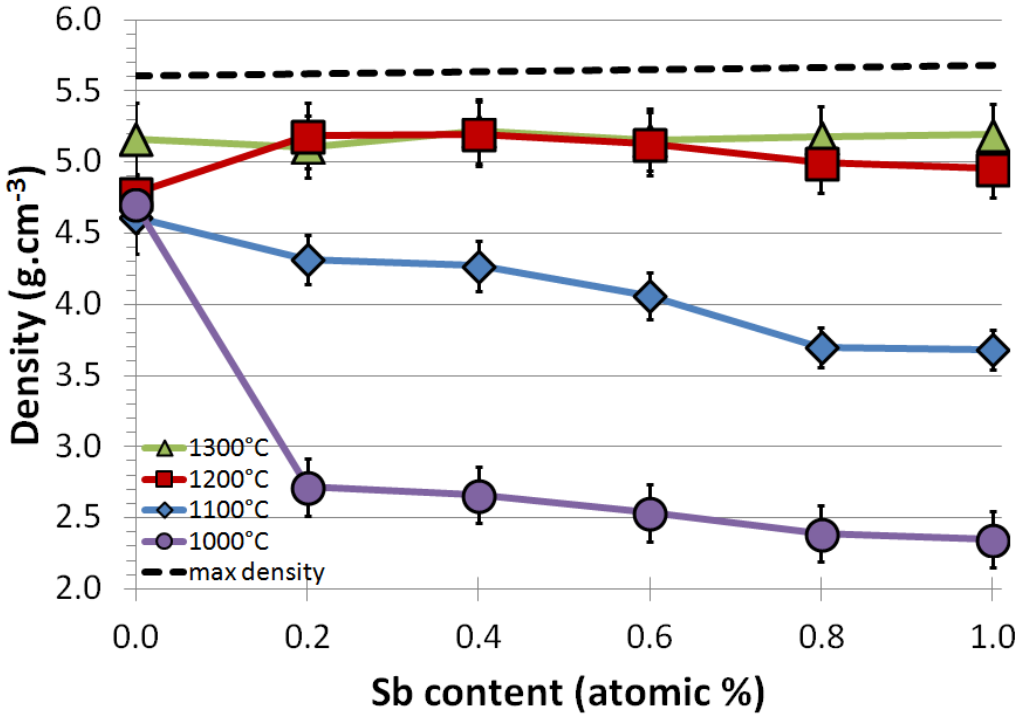

Figure 19: Density of Sb doped ZnO pellets as a function of Sb content for samples of $ZnSb_xO_{1-x}$ (0.000<x<0.010) sintered for 8 hours at 1000°C, 1100°C, 1200°C, and 1300°C.

The densities of the 0.0at.% Sb doped pellets sintered at 1000°C, 1100°C and 1200°C are similar, this indicates that at these temperatures the sintering behaviour of undoped ZnO is unchanged. The 0.0at.% pellet sintered at 1300°C has a higher density. As the level of Sb dopant was increased, the sinter treatment temperature has more of an impact upon the final density of the material. A decrease in density with increasing Sb content from 0.2at.% to 1.0at.% is apparent for the materials sintered at 1000°C and 1100°C, with the effect being more subtle for the material sintered at 1200°C. The density of the material sintered at 1300°C remains unchanged with increasing Sb content from 0.2at.% to 1.0at.% Sb.

4. Porosity dependent variables

The microstructure of the polished cross sections of 1.0at.% Sb doped ZnO compacts are shown in *Figure 20*. The darker areas in the images are the pores within the material. After sintering at 1100°C, there are many pores distributed in the material. The pores exist at the grain boundaries and at higher temperatures, where there is more energy available for grain development, there are less pores due to the grain boundaries migrating.

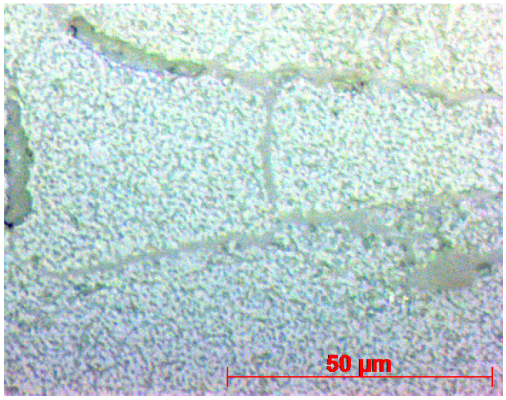

1100°C

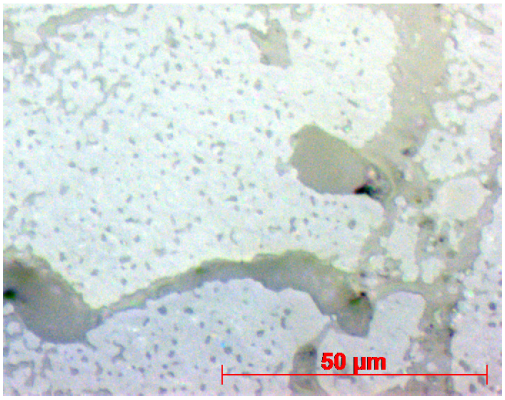

1200°C

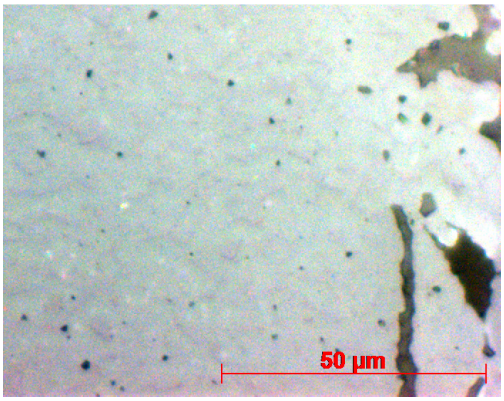

1300°C

Figure 20: Images of polished cross section of 1.0at.% Sb doped ZnO sintered for 8 hours at 1100°C, 1200°C, and 1300°C.

4. Porosity dependent variables

The SEM micrographs of the fracture cross sections of the Sb doped samples sintered at 1000°C, 1100°C, 1200°C and 1300°C are shown in *Figure 21*.

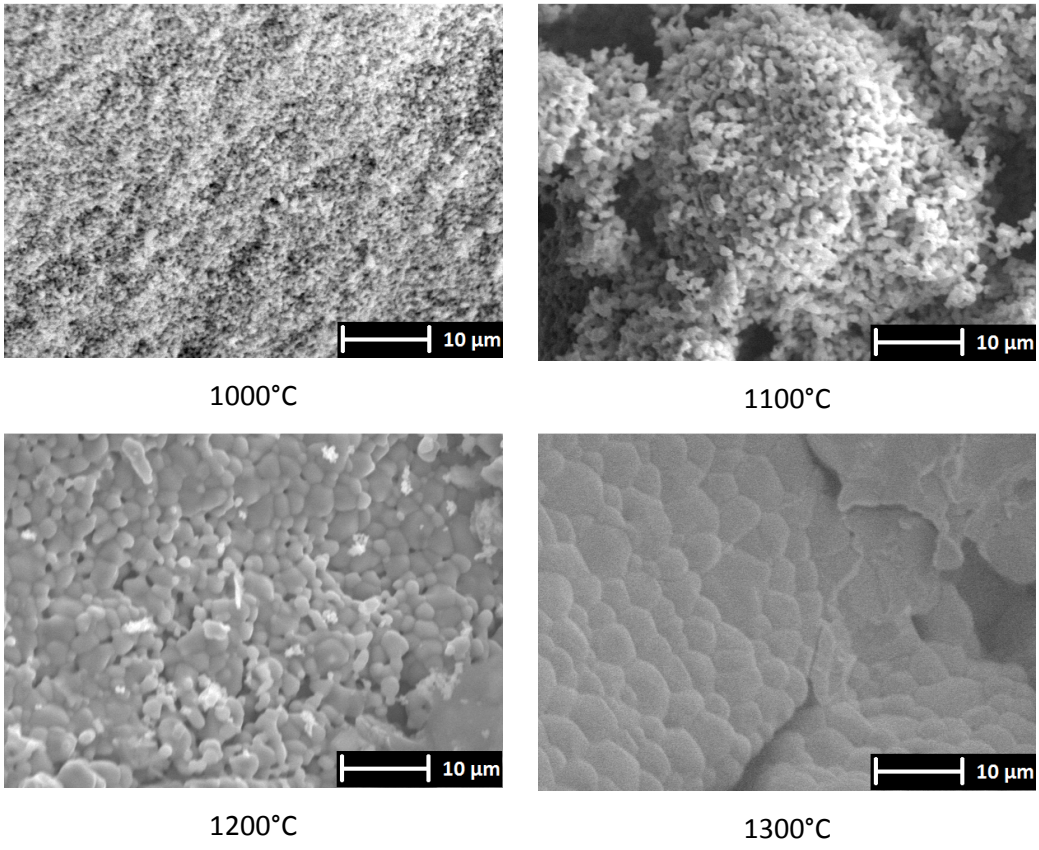

Figure 21: SEM micrographs showing the fracture cross section of 1.0at.% Sb doped ZnO sintered for 8 hours at 1000°C, 1100°C, 1200°C, and 1300°C.

There is a physical change in the microstructure of the Sb doped ZnO samples with increasing temperature, the individual grains of the material can be seen in the SEM micrographs (*Figure 21*) and are increasing in size with increasing sintering temperature for all levels of doping shown. At lower sintering temperatures, the grain sizes are smaller and the pore networks more open. After sintering at higher temperatures, the samples show a dense material with a closed pore network, this mirrors observations in *Figure 20*.

4. Porosity dependent variables

The degree of Sb dopant also has an impact upon the structure of the material. Polished cross sections of Sb doped ZnO sintered at 1200°C are shown in *Figure 22*.

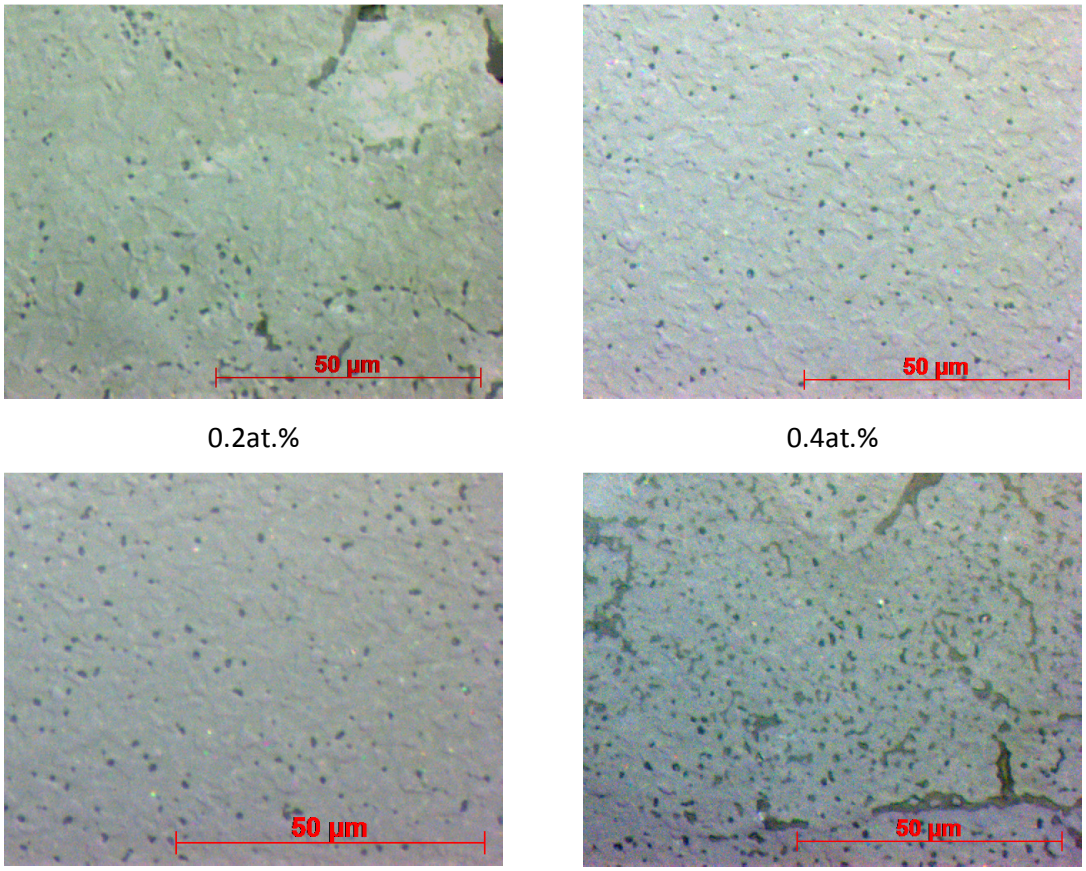

0.2at.% 0.4at.%

0.6at.% 0.8at.%

Figure 22: Images of polished cross section of 0.2at.%, 0.4at.%, 0.6at.%, and 0.8at.%Sb doped ZnO sintered for 8 hours at 1200°C.

As the Sb content is increased, the structure becomes more porous. This can be attributed to the fact that the $Zn_7Sb_2O_{12}$ phase acts to lower the grain boundary mobility due to pinning effects during sintering (Park et al., 2008). There is evidence that the amount of $Zn_7Sb_2O_{12}$ phase increases with Sb content, *Figure 18*, which means that the pinning effect increases with Sb content, resulting in smaller grains and higher porosity.

4. Porosity dependent variables

The volume fraction porosities for 0.0at.% - 1.0at.% Sb doped ZnO pellets sintered at 1000°C,1100°C, 1200°C and 1300°C are shown in *Figure 23* as a function of Sb content.

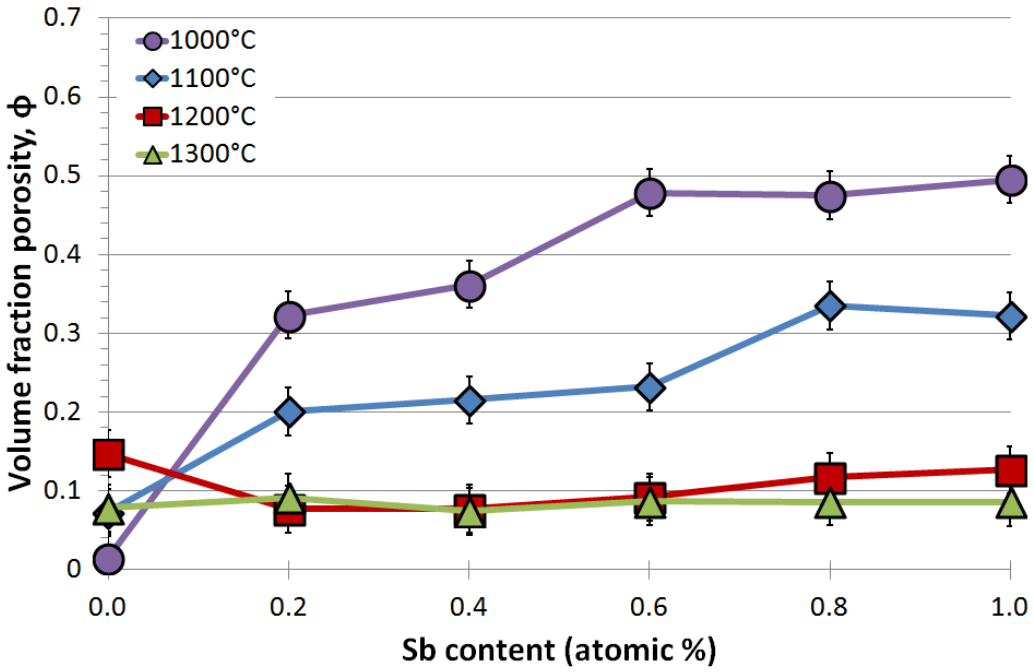

Figure 23: Porosity dependence on the doping level for Sb doped ZnO sintered at different temperatures

The sintering treatment temperature has an impact upon the degree of porosity of Sb doped ZnO, with porosity decreasing with increase in temperature. This is reflected in observations of the microstructure in *Figure 20* and *Figure 21* where the size of the grains is larger after higher sintering temperatures, and the structure less porous. The lowest porosity was found for the samples sintered at 1300°C with a porosity of 8% which remains constant with Sb content. The samples sintered at 1200°C match closely to the 1300°C samples which indicates that increasing the sintering temperature in this range has less of an impact upon porosity. This indicates a closed pore network which requires much higher energies to density the material further. There is a general trend that porosity increases with Sb doping between Sb content of 0.2 and 1.0 atomic % for the samples sintered at 1000°C, 1100°C, and 1200°C. This is further evidence that the $Zn_7Sb_2O_{12}$ phase inhibits of the densification of ZnO, causing the degree of porosity to increase with Sb content. In order to link the extent that the $Zn_7Sb_2O_{12}$ second phase has on the porosity, the volume fraction

porosity is plotted as a function of the ratio of second phase to ZnO, as determined from the data from *Figure 18*, and presented in *Figure 24*.

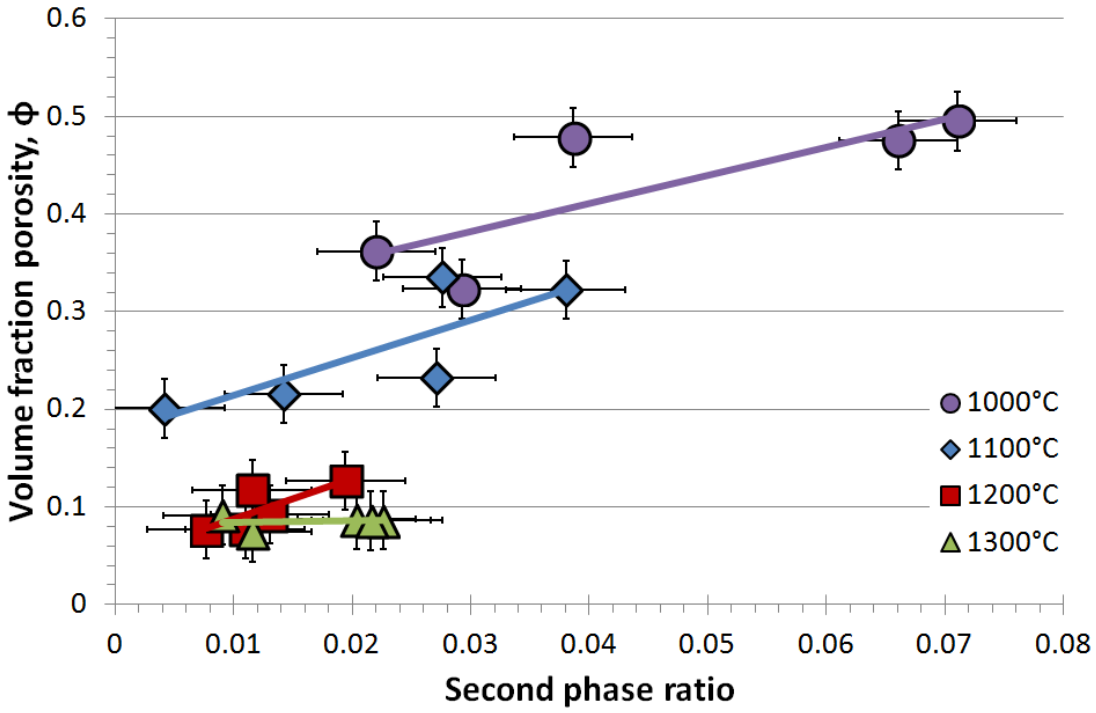

Figure 24: Volume fraction porosity as a function of the relative intensity ratio of the (440) XRD peak of $Zn_7Sb_2O_{12}$ to the (110) XRD peak of ZnO for samples of 0.2at.% to 1.0at.% Sb doped ZnO sintered for 8 hours at 1000°C, 1100°C, 1200°C, and 1300°C.

There is an increase in the volume fraction of porosity with increase in amount of $Zn_7Sb_2O_{12}$ phase present within the Sb doped samples. This indicates that the pinning mechanisms of the secondary phase are the main contribution to the increase in porosity with Sb content. This trend is present for all sintering treatment temperatures; however for the samples sintered at 1300°C the increase in porosity with the secondary phase is negligible and forms a region that remains constant across all doping levels with a porosity in the region of 8%. This implies that at this doping range, a temperature of 1300°C provides the material with enough energy for pinning effects to be less of an influence during the sintering process, resulting in a reduction of inhibition of the densification and a constant porosity with Sb content.

4.3. Al dopant

Samples of aluminium doped ZnO were prepared by the solid oxide route according to stoichiometric $ZnAl_xO_{(1-x)}$ from x = 0.000 to x = 0.015. After synthesising the pellets, the samples were sintered at temperatures of 1100°C, 1200°C, and 1300°C.

In order to determine how material changes with increasing Al content, analysis was carried out using X-Ray Diffraction, the results of which are shown in *Figure 25*, *Figure 26* and *Figure 27* for samples sintered at 1100°C, 1200°C and 1300°C respectively. Vertical lines indicating the relative intensities and position of the peaks for undoped ZnO (pdf# 361451) are provided for clarity.

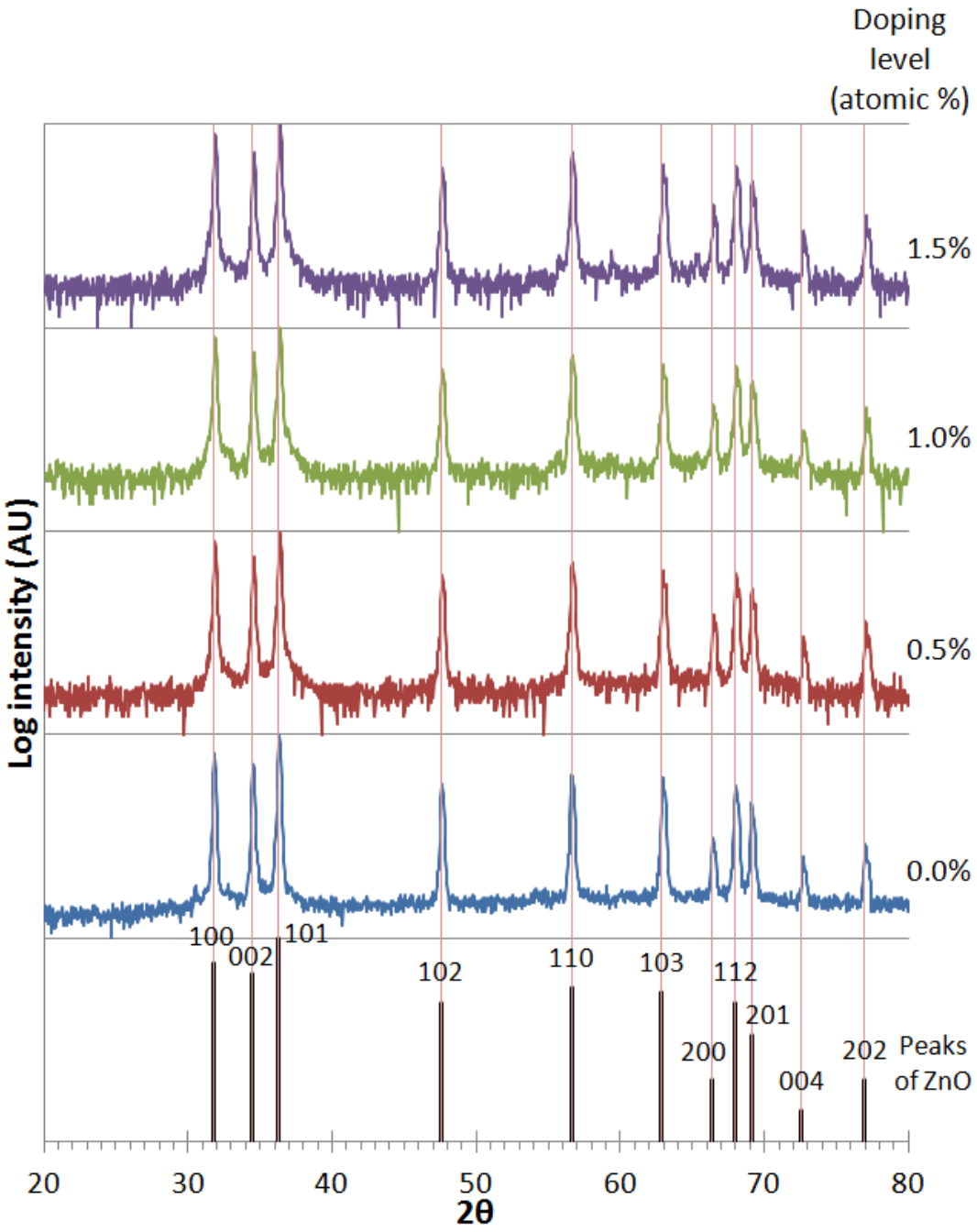

Figure 25: XRD analysis of Al doped pellets sintered for 8 hours at 1100°C

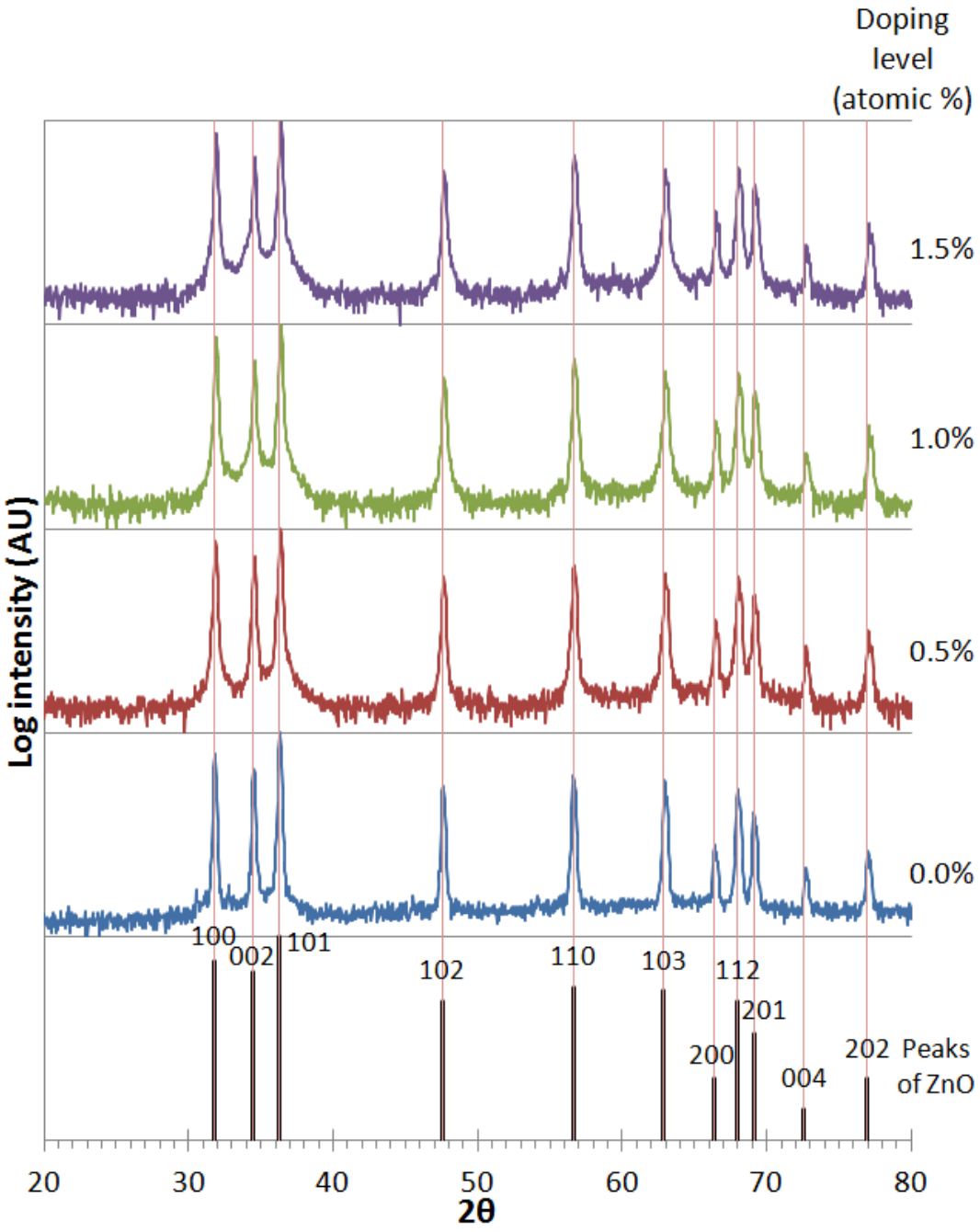

Figure 26: XRD analysis of Al doped pellets sintered for 8 hours at 1200°C

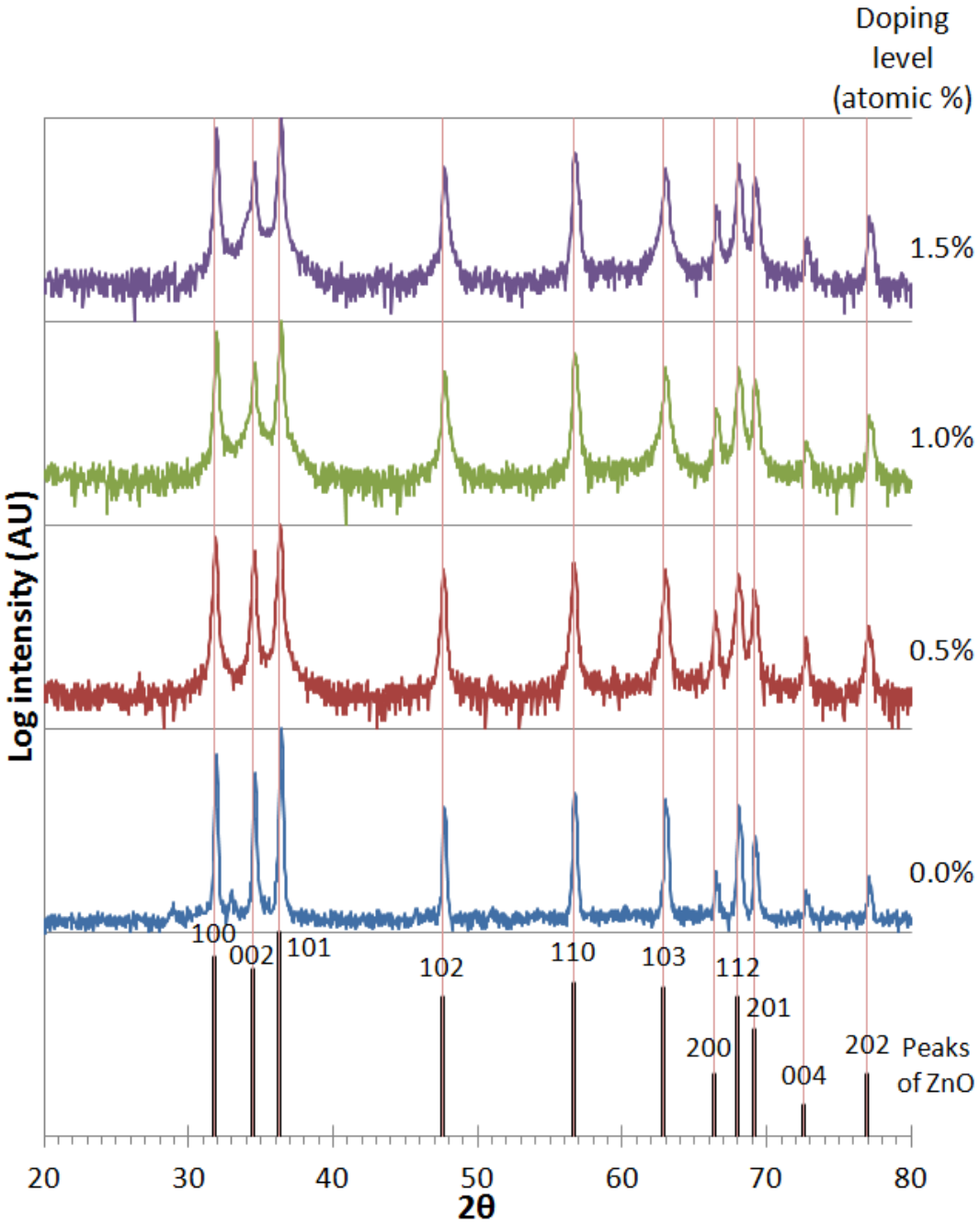

Figure 27: XRD analysis of Al doped pellets sintered for 8 hours at 1300°C

4. Porosity dependent variables

There is a broadening of the peaks of ZnO with increasing doping level and increasing sintering temperature. The broadening of the peaks is particularly apparent in the diffraction patterns of the samples sintered at 1300°C shown in *Figure 27*.

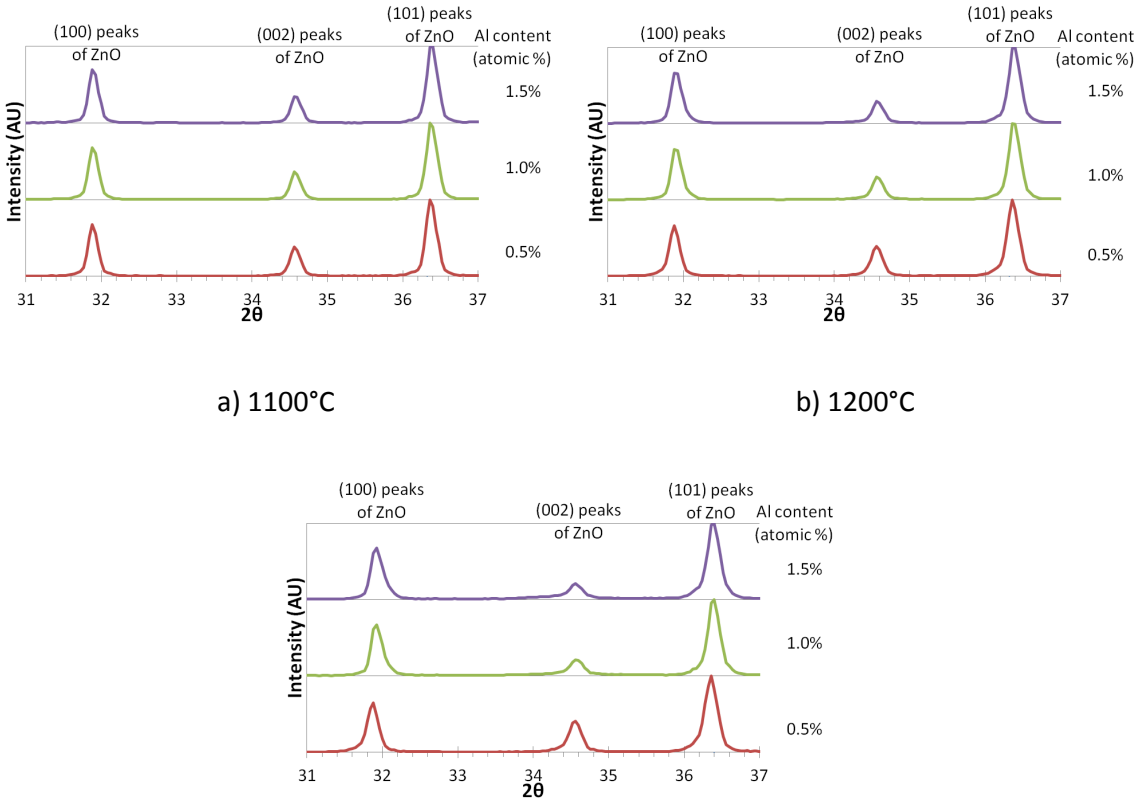

Figure 28: XRD analysis showing the (100), (002), and (101) hkl peaks of (0.5at.% to 1.5at.%) Al doped ZnO pellets sintered for 8 hours at; a) 1100°C, b) 1200°C, and c) 1300°C.

Peak broadening can also be used to estimate grain size, from the Scherrer equation, *equation (11)*, where *D* is the grain size, *K* is the shape factor, λ is the X-ray wavelength, β is the width of peak (FWHM), and θ is the Bragg angle. However, this is only applicable to nano scale grains no larger than 0.1µm (Tseng et al., 2015), and therefore is not applicable in this instance where the grain sizes are >1.0µm.

4. Porosity dependent variables

$$D = \frac{K\lambda}{\beta \cos\theta} \qquad (11)$$

The peak broadening can also be used for quantifying the extent of dopant acceptance into the unit cell. Broadening of the peaks in XRD data are indicative of substitutional doping within the material. The broadening of the peaks is related to Braggs law, *equation (12)*, where *n* is an integer, λ is the wavelength of the X-ray, *d* is the lattice, and θ is the scattering angle.

$$n\lambda = 2d \sin\theta \qquad (12)$$

In order to observe how the broadening of the peaks changes with increasing sintering treatment temperature, the width of the (101) hkl peaks of ZnO were obtained from the XRD data and the full width at half maximum (FWHM) of the peaks are shown in *Figure 29* as a function of sintering temperature.

The broadening occurs due to the distribution of both Zn-O and Al-O bonds, which have different lengths, within the material. Therefore there is a distribution of different lattice spacing, *d* within the material and therefore the angle, θ *equation (12)*, which has the effect of broadening the width of peaks. The increase in the peak width with sintering temperature is a result of the Al being accepted into the ZnO unit cell.

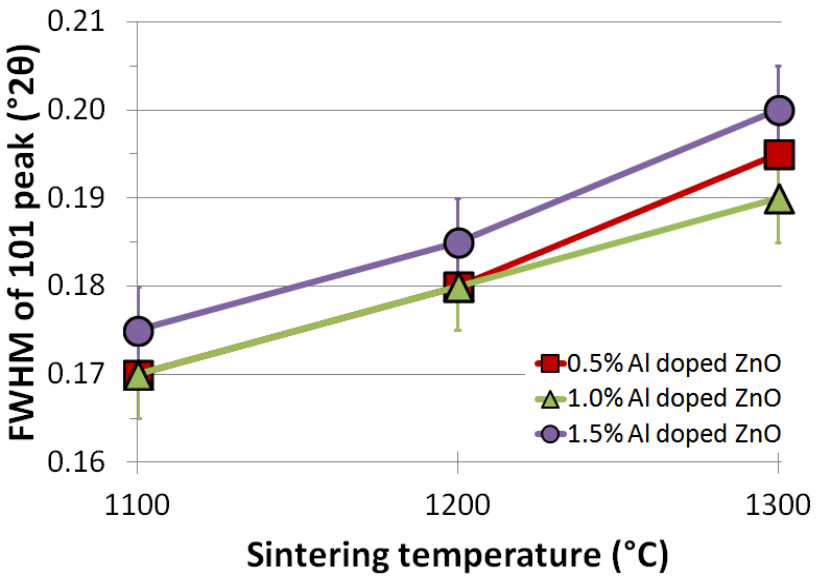

Figure 29: Full width at half maximum (FWHM) of the (101) peaks of ZnO as a function of sintering temperature for (0.5at.% to 1.5at.%) Al doped ZnO pellets sintered for 8 hours at 1100°C, 1200°C, and 1300°C

From the information presented in *Figure 29* the FWHM of the (101) peaks of ZnO increase with sintering temperature, the peaks broaden by approximately $\Delta 2\theta = 0.02°$ between sintering temperatures of 1100°C and 1300°C.

In order to determine how the porosity of the sintered ZnO pellets is affected by the level of Al doping, the density of the pellets was calculated and is shown in *Figure 30* as a function of Al content. The maximum theoretical density is also shown for comparison. This was calculated on the assumption that Al substitutes on the Zn site in ZnO (Maldonado and Stashans, 2010) and that the unit cell volume remained unchanged.

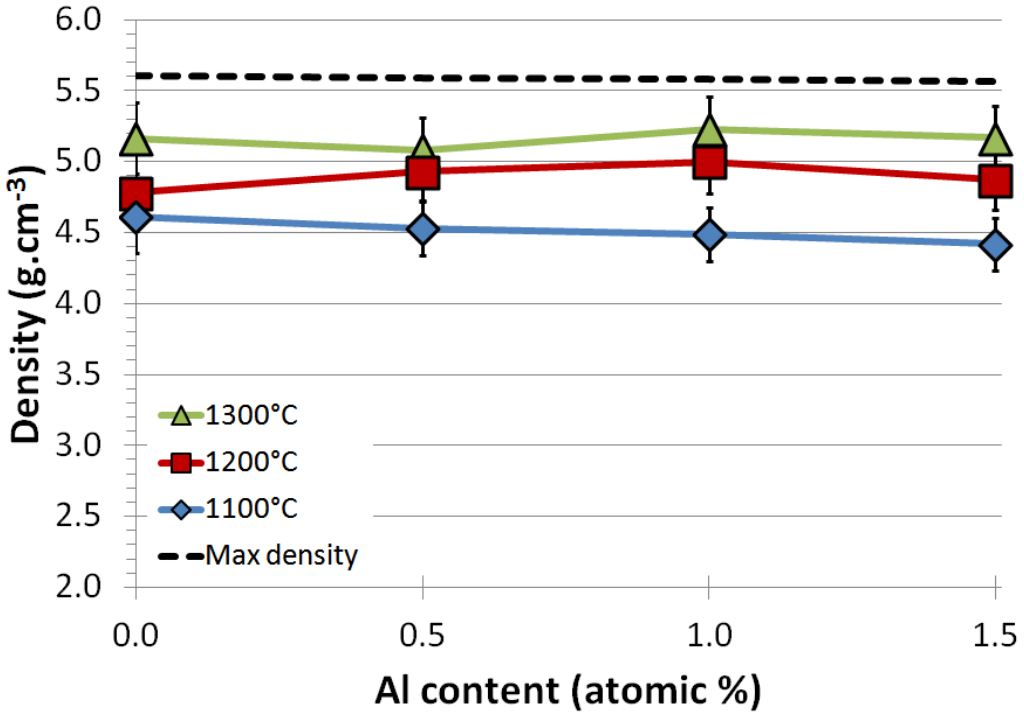

Figure 30: Density as a function of Al content for 0.0at.% to 1.5at.% Al doped ZnO sintered for 8 hours at 1100°C, 1200°C, and 1300°C.

The density of the sintered Al doped ZnO increases with sintering temperature, with a sintering temperature of 1300°C producing the pellets with the greatest density in the region of 5.2g.cm^{-1}. The density of the Al doped ZnO pellets remains constant with Al content within the error associated with the measurement. This indicates that in the doping range studied, the Al additions into the lattice do not significantly affect the final density of the sintered material.

The development of pores can be observed in the polished cross sections of sintered Al doped ZnO compacts, *Figure 31*. The darker areas in the images are the pores within the material. There are many pores distributed in the material in the sample sintered at 1100°C, after higher sintering temperatures, the number of pores in the material has reduced.

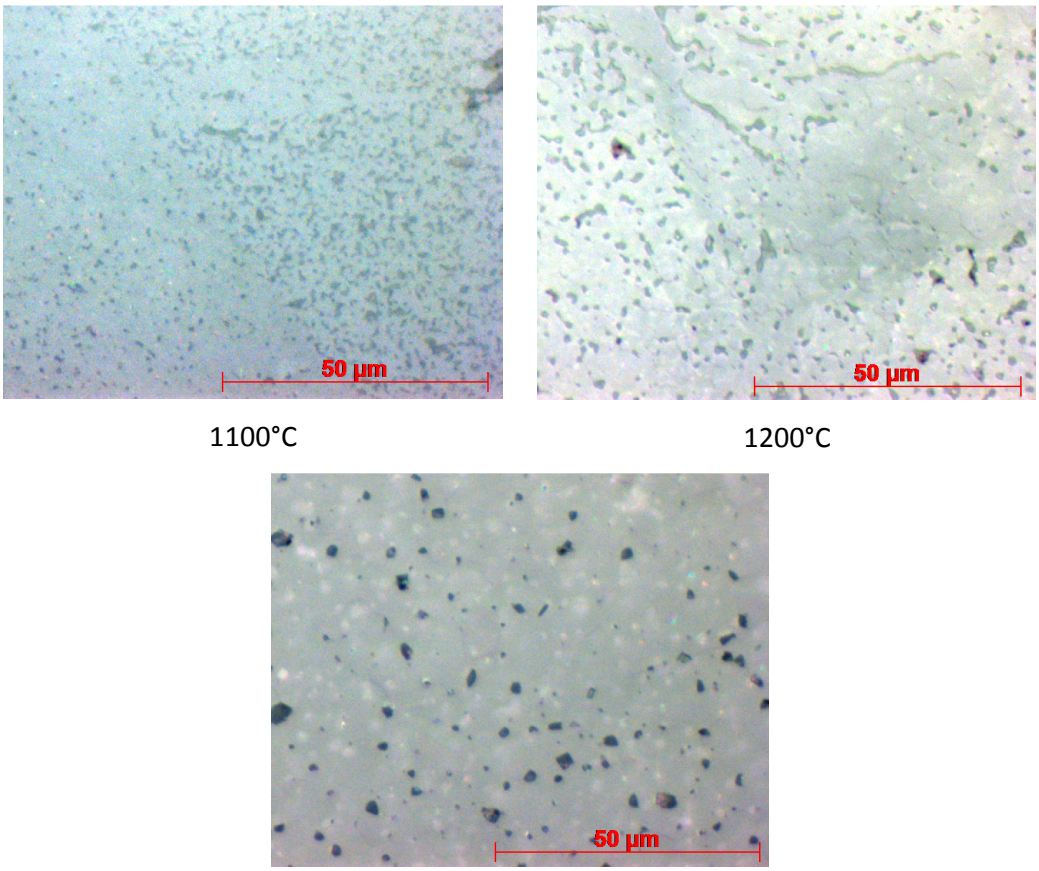

1100°C

1200°C

1300°C

Figure 31: Images of polished cross section of 1.0at.% Al ZnO sintered for 8 hours at 1100°C, 1200°C, and 1300°C

4. Porosity dependent variables

The grains can be seen in the SEM micrographs of the fracture cross sections of the sintered material, *Figure 32*. After a sinter treatment temperature of 1100°C, the grains are small and the porosity open, mirroring the observation in Figure 31, after a sinter treatment temperature of 1200°C larger grains have developed and after a sinter treatment temperature of 1300°C, the grains are much larger and the porosity has developed from an open pore structure to a more closed structure.

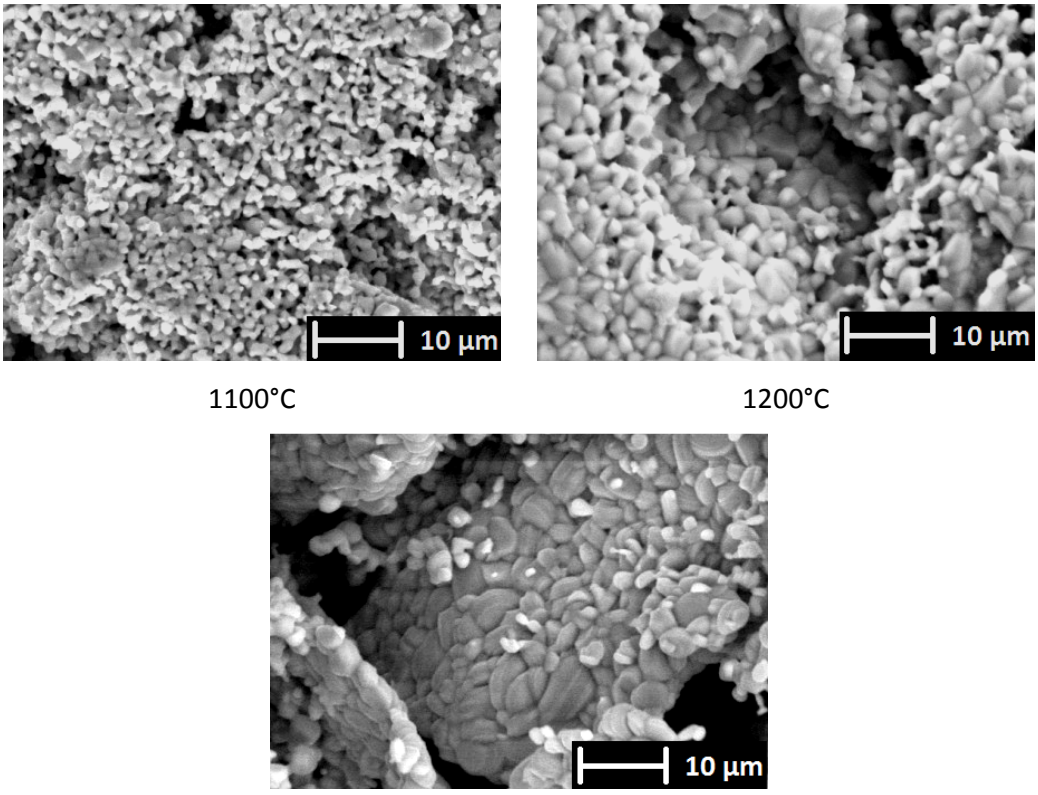

1100°C 1200°C

1300°C

Figure 32: SEM micrographs of fracture cross section of 1.0at.% Al ZnO sintered for 8 hours at 1100°C, 1200°C, and 1300°C.

4. Porosity dependent variables

The polished cross sections of 0.5at.%, 1.0at.%, and 1.5at.% Al doped ZnO sintered at 1200°C are shown in *Figure 32*. There is little change in the structure of the samples between doping levels, this indicates that the amount of Al dopant in the range studied has little impact on the microstructure.

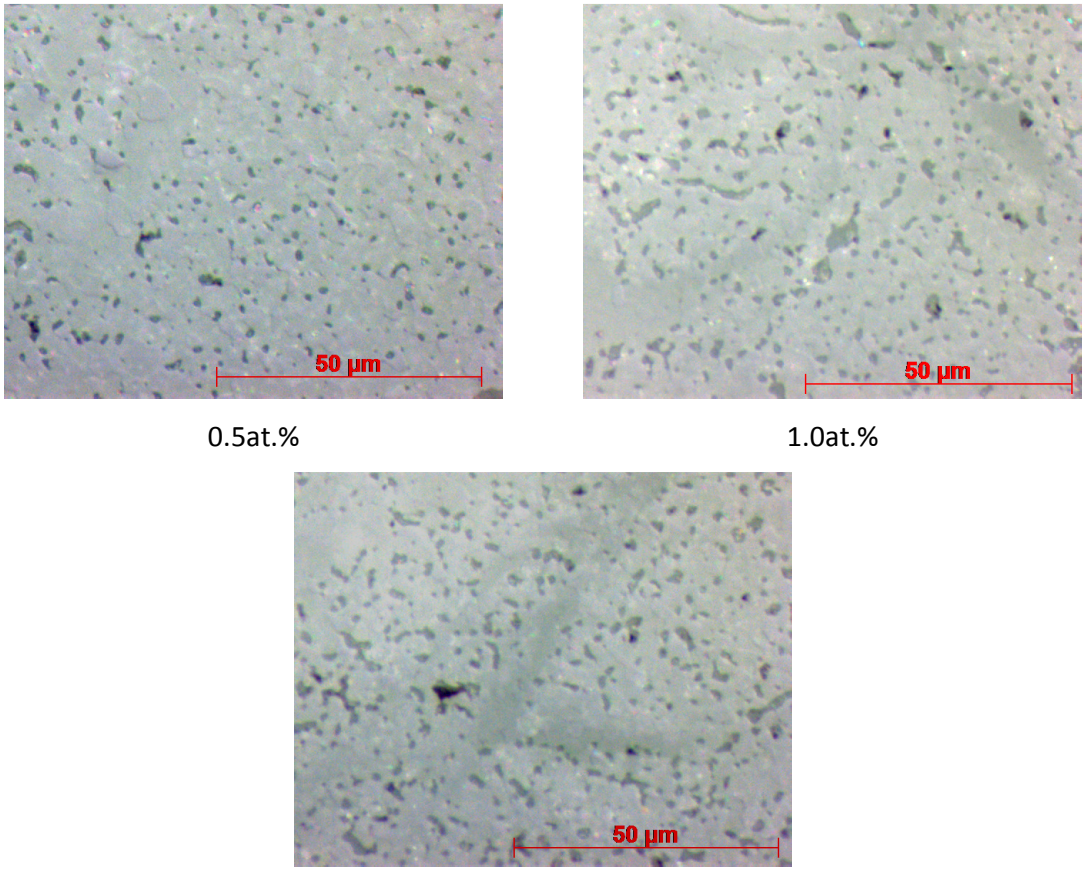

0.5at.% 1.0at.%

1.5at.%

Figure 33: Images of polished cross section of 0.5at.%, 1.0at.%, and 1.5at.% Al doped ZnO sintered for 8 hours at 1200°C.

4. Porosity dependent variables

In order to determine if the Al content has an impact on the porosity, the volume fraction porosity of the Al doped ZnO samples is shown in *Figure 34* as a function of Al content.

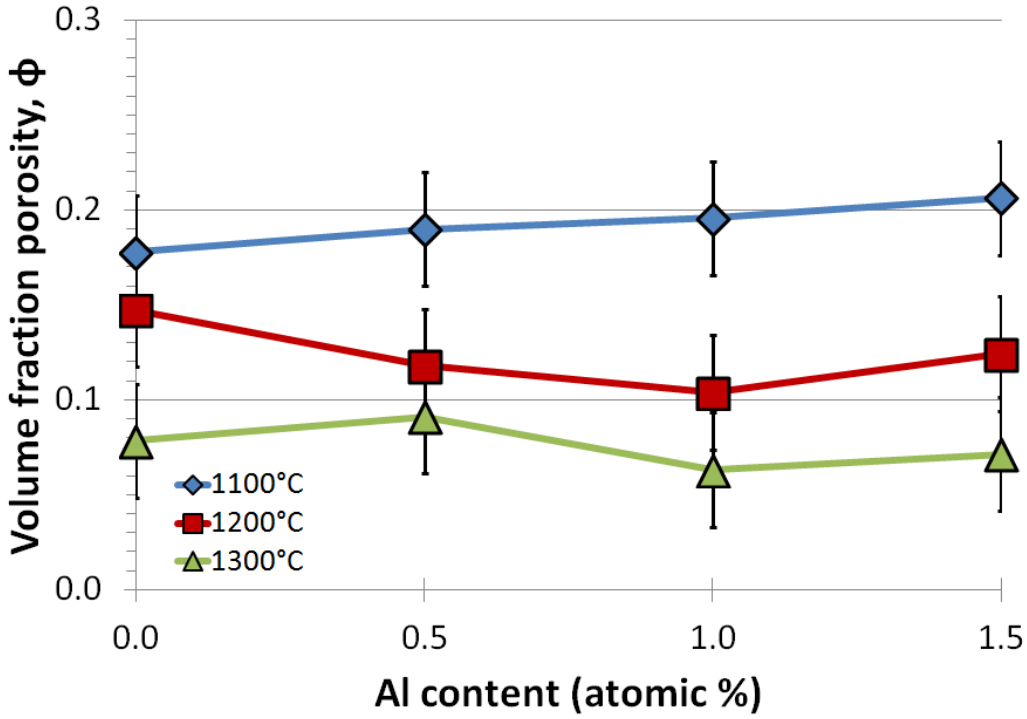

Figure 34: Porosity dependence on the doping level of Al doped ZnO sintered for 8 hours at 1100°C, 1200°C, and 1300°C

There is little change in porosity with Al content for all sintered materials, which is mirrored in *Figure 33*. This suggests that the addition of Al into the system has not inhibited the densification during the sintering process. This also indicates that Al successfully incorporates into the ZnO system without producing secondary phases which would also inhibit densification.

4.4. Summary

The density of doped ZnO material increases as the sintering temperature is increased, and the degree of porosity reduces. The degree of porosity of the doped ZnO material is in the region of 8% for both Al and Sb doped material sintered for 8 hours at 1300°C. The degree of porosity increases with doping level for sintering temperatures of 1000°C, 1100°C and 1200°C for Sb doped samples, while there is no change in porosity with increasing Al content. The porosity is sensitive to the level of Sb content, which is due to the presence of a secondary phase within the Sb doped material, which inhibits the densification leading to a higher degree of porosity. This is backed up with findings in the literature (Park et al., 2008).

There is a physical change in the microstructure of both the Al and Sb doped ZnO samples with increasing temperature. The samples sintered at 1300°C show a dense material with larger grain sizes and at lower sintering temperatures, the grain sizes are smaller, this is reflected in the level of porosity for the sintered materials.

5. Electrical and thermal conductivity

In this chapter the effect that porosity has on the electrical resistivity of doped ZnO is investigated. By linking porosity effects to known models and experimental data obtained, the effects that doping has on the electrical properties was studied. The effect that porosity has on the thermal conductivity of doped ZnO is also investigated by linking porosity effects to experimental data obtained.

5.1. Electrical conductivity

5.1.1. Sb doped ZnO

The electrical resistivity of Sb doped ZnO is shown in *Figure 35* as a function of Sb content. The resistivity decreases with increasing sintering temperature, reflecting the lower degree of porosity present *(Chapter 4)*.

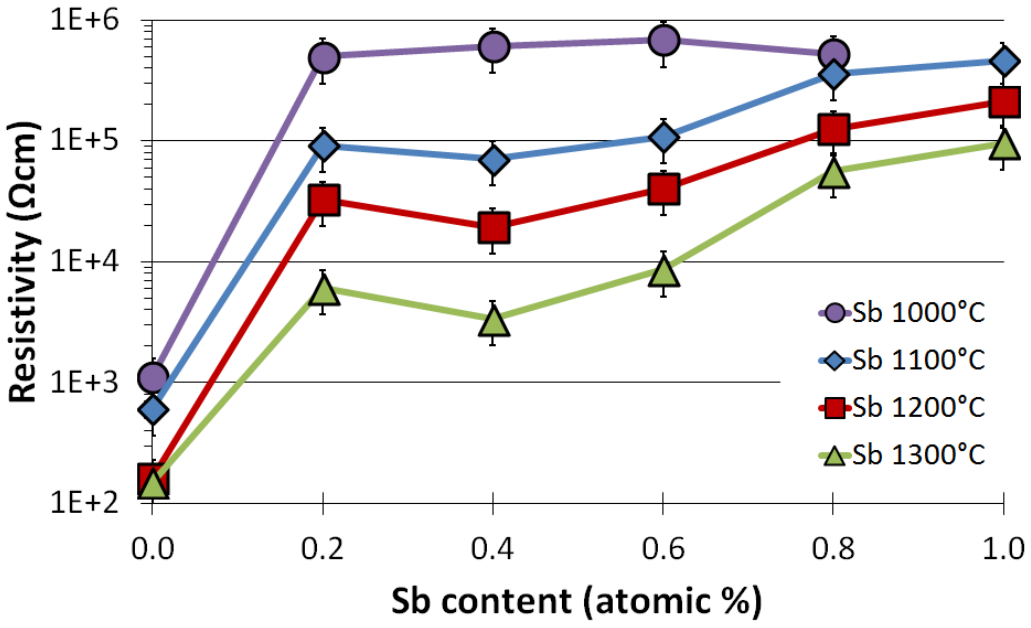

Figure 35: Electrical resistivity of as a function of Sb content for 0.0at.% to 1.0at.% Sb doped ZnO sintered for 8 hours at 1000°C, 1100°C, 1200°C, and 1300°C

The resistivity of the 0.2at.% to 1.0at.% Sb doped materials, *Figure 35*, is greater than undoped material however for the materials with Sb content greater than 0.0at.%, the resistivity exhibits a minimum at a Sb content of 0.4at.% for the materials sintered at 1100°C, 1200°C, and 1300°C and then increases further with Sb content. The electrical resistivity depends on both the doping level and level of porosity in the materials. In order to understand how porosity and doping each affect the electrical resistivity it is necessary to isolate the two effects.

By considering the doped material after an ideal sinter stage where the material is fully densified with no pores present in the structure, the effect of porosity upon the electrical resistivity could be evaluated. This could be accomplished by comparing to the porous material in order to evaluate the porosity effects upon the electrical resistance. Achieving an ideal sinter would not be practical in this instance due to the high energies required, therefore in order to evaluate the effect of porosity upon the electrical resistivity, first the geometry of the pores must be taken into consideration. The geometry of various pore configurations is illustrated in *Figure 36*. These can be used as the basis of various models presented in *Table 1* which describe the resistivity dependence based upon pore geometry.

The models are used to determine the resistivity dependence upon porosity by modelling the pores as an idealised shape. The shape of the pore determines how the electrical resistivity is affected by modelling the passage of electrical current through the material with an insulating void within the material of the same dimensions as the pore.

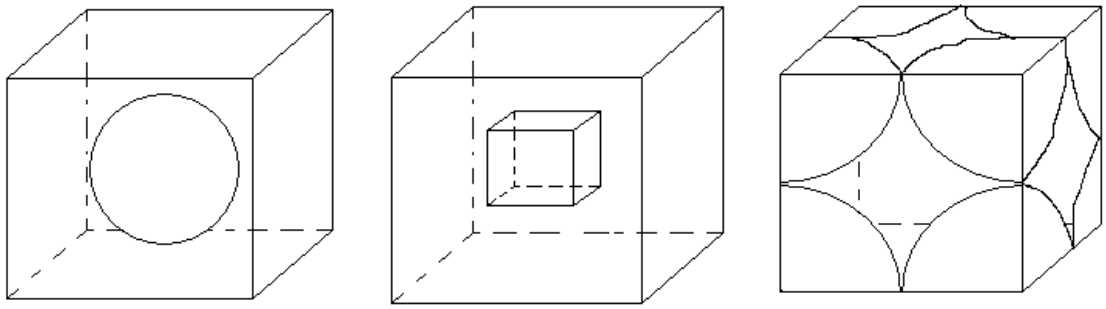

Spherical pore | Cubic pore | Pore between spherical particles

Figure 36: Various pore structures found in sintered bodies

In order to determine the electrical resistivity of the material without pores, also known as the matrix resistivity (ρ_0), the model curves calculated from the equations given in *Table 1* were fitted to the experimental data by varying the matrix resistivity to minimise the sum of the squares of error between experimental data and calculated values. The comparison of best fit model curves and experimental data are shown in *Figure 37*.

Table 1: Models for porosity dependence of the electrical resistivity where ρ is the resistivity of the porous material, ρ_0 is the resistivity of the matrix material and ϕ is the volume fraction porosity. For the Spriggs model, b depends on the geometry of the pores, for spherical pores b=3

Pores between spherical particles	$\frac{\rho}{\rho_0} = 1/(1-1.5\phi)$
Spherical pores	$\frac{\rho}{\rho_0} = 1/(1-\phi)^{3/2}$
Cubic pores	$\frac{\rho}{\rho_0} = 1+\frac{\phi}{1-\phi^{2/3}}$
Rule of mixtures	$\frac{\rho}{\rho_0} = 1/(1-\phi)$
Spriggs	$\frac{\rho}{\rho_0} = 1/\exp(-b\phi)$

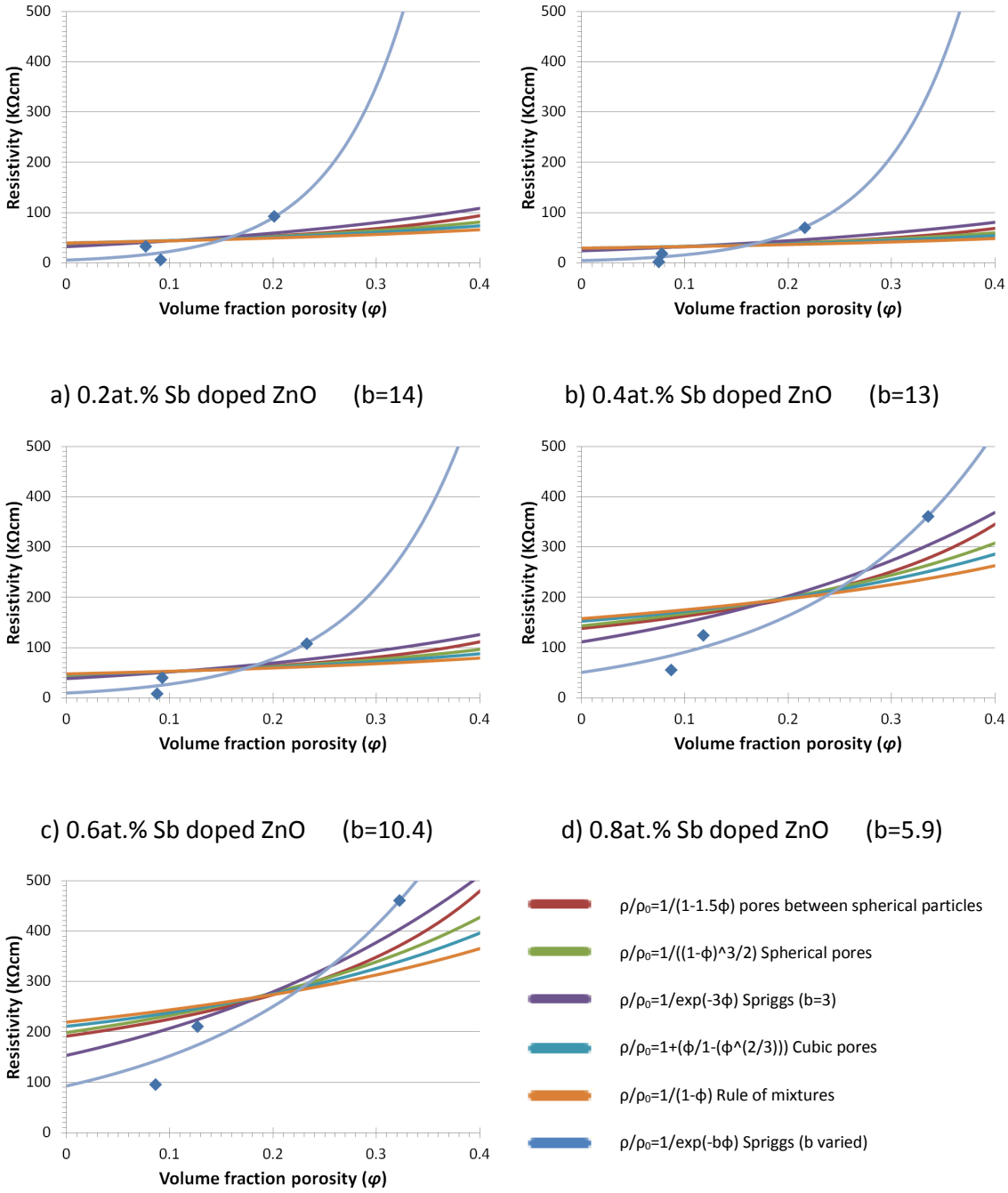

Figure 37: Least squares fitting of the curves described by each porosity model to the electrical resistivity of Sb doped ZnO pellets sintered for 8 hours at 1100°C, 1200°C, and 1300°C with Sb content of a) 0.2at.%, b) 0.4at.%, c) 0.6at.%, d) 0.8at.%, and e) 1.0at.%

5. Electrical and thermal conductivity

The values for the matrix resistivity as determined by the experimental values of porosity and resistivity of the sintered samples are displayed in *Table 2*. The Spriggs model with the value for *b* dynamically altered to give the best fit for each doping level gives the closest match to the experimental data as indicated by the quality of fit values, R^2. The other fitted models have one variable which is the matrix resistivity, ρ_0 which was varied in order to obtain the best fit. These curves do not fit as well to the experimentally determined values of electrical resistivity due to the assumption of a uniform and idealised geometry of the pores which is not achieved in the microstructures observed.

Using the data obtained from the model fitting to the experimental data for resistivity, the matrix resistivity for each doping level has been extrapolated from each fitted model and is shown in *Figure 38*.

Table 2: Fitted parameters of each model to the experimental data

Model	Sb content Atomic %	Matrix resistivity P_0 (KΩcm)	R^2
$\frac{\rho}{\rho_0} = 1/(1-1.5\phi)$ Pores between spherical particles	0.2	38	0.24
	0.4	28	0.27
	0.6	45	0.32
	0.8	138	0.62
	1.0	192	0.65
$\frac{\rho}{\rho_0} = 1/(1-\phi)^{3/2}$ Spherical pores	0.2	38	0.22
	0.4	28	0.25
	0.6	45	0.29
	0.8	143	0.55
	1.0	198	0.58
$\frac{\rho}{\rho_0} = 1 + \frac{\phi}{1-\phi^{2/3}}$ Cubic pores	0.2	39	0.18
	0.4	29	0.20
	0.6	47	0.24
	0.8	152	0.47
	1.0	211	0.50
$\frac{\rho}{\rho_0} = 1/(1-\phi)$ Rule of mixtures	0.2	40	0.14
	0.4	29	0.17
	0.6	48	0.19
	0.8	158	0.38
	1.0	219	0.41
$\frac{\rho}{\rho_0} = 1/\exp(-3\phi)$ Spriggs (b=3)	0.2	33	0.36
	0.4	24	0.42
	0.6	38	0.46
	0.8	111	0.76
	1.0	153	0.80
$\frac{\rho}{\rho_0} = 1/\exp(-b\phi)$ Spriggs (b varied)	0.2	6 (b=14)	0.88
	0.4	4 (b=13)	0.95
	0.6	10 (b=10.4)	0.91
	0.8	50 (b=5.9)	0.97
	1.0	93 (b=5.0)	0.95

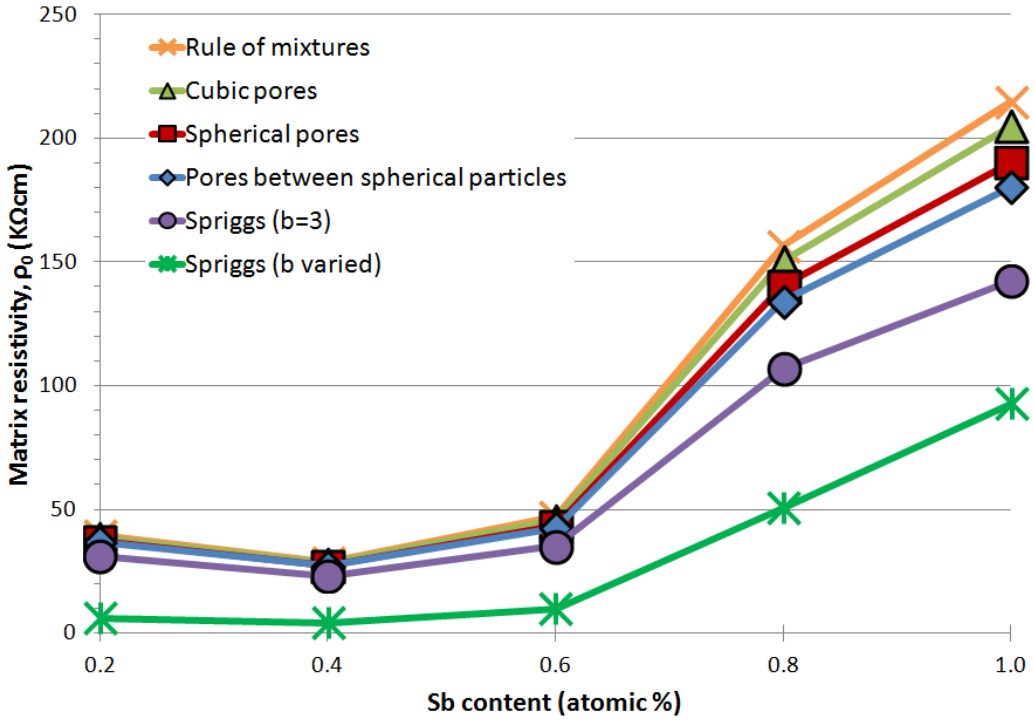

Figure 38: Predicted matrix resistivity as a function of doping level, derived from different porosity models applied to experimental data.

The variation in matrix resistivity for all the models follows the same trend, as shown in *Figure 38*, with a low plateau value for Sb content between 0.2at.% and 0.6at.%, which then increases when Sb content is between 0.6at.% and 1.0at.%. The Spriggs model fitting with altered *b* values for each Sb doping level matches the experimental data the closest and also extrapolates to a matrix resistivity closest to that exhibited at the highest density sample for each dopant level. This predicts a minimum matrix resistivity of 4kΩcm at a Sb content of 0.4 atomic %.

Even though the Spriggs porosity model has the closest fit to the data compared to the other models fitted, as determined by the R^2 values, it is still not a perfect fit to the experimental data. It was assumed that the geometry of the pores remains unchanged with sintering temperature and independent of porosity, therefore the value for the geometry

factor, *b* used in the Spriggs model stays at a constant value for different sintering temperatures at each doping level. By studying the cross sections of Sb doped ZnO, *Figure 20*, and *Figure 21*, it is clear that the geometry of the pores change with sintering temperature. At 1100°C the material forms a loose and open pore structure which develops as the sintering temperature is increased and forms a closed pore structure at 1300°C. This change in pore structure alters the shape of the pores which in turn will cause the pore geometry factor, *b* to be different after each sintering temperature.

There is less of a difference in the geometry of pores between samples sintered at the same temperature. The geometry factors, *b* for the materials sintered at 1000°C, 1100°C, 1200°C and 1300°C were determined from the density and porosity data and are shown in *Figure 39*.

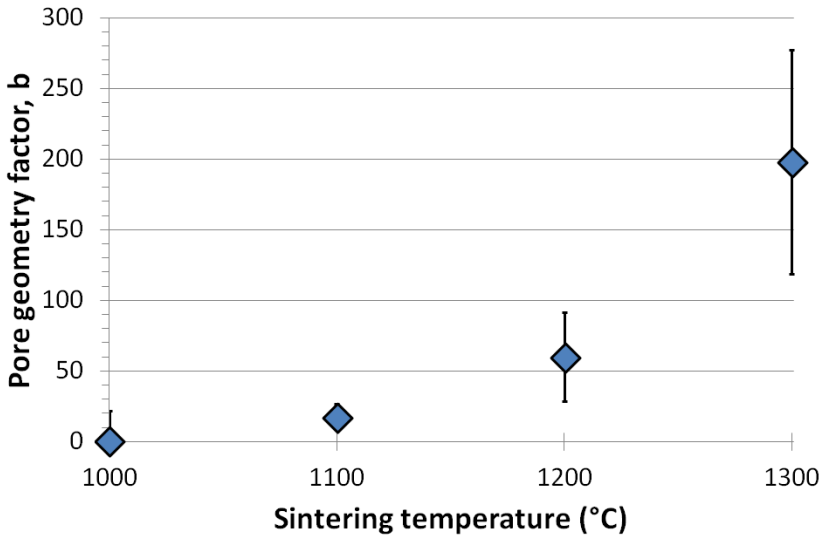

Figure 39: Pore geometry factor, b as a function of sintering temperature for Sb doped ZnO

The pore geometry factor increases with the sintering temperature which indicates a change in the geometry of the pores which is mirrored in observations of the microstructure. Due to the scatter of the data and the standard error of data values, a large uncertainty factor is introduced when the experimental data was used to obtain values of *b*. This combined with there being little change in porosity with doping level at each sinter temperature means curve fitting results in a large uncertainty factor. The uncertainty factor is so large that it

would not be practical to use the values of *b* for detailed analysis, however it is clear that the value is not constant but increases with sinter temperature.

The geometry factor tends to vary within a limited range and values >50 are considered extreme. Calculation of the geometry factor requires constant pore type and constant matrix resistivity. The resistivity of the samples increases with Sb content due to changes to the matrix resistivity and/or pore shape. The effect of this is that the b value appears larger. The extreme geometry factors calculated indicate that more than just pore effects are altering the resistivity, and that changes with matrix resistivity are evidence of Sb incorporation. It is observed in *Chapter 4* that the level of Sb incorporation increases with sintering temperature, therefore the matrix resistivity may also change with sintering temperature and therefore the calculated geometry factor may be higher.

5.1.2. Al doped ZnO

The electrical resistivity of Al doped ZnO is shown in *Figure 40* as a function of Al content. The electrical resistivity is lowest for material sintered at 1300°C, which is due to the lower degree of porosity present. For each sintering temperature, the electrical resistivity of the Al doped material is lower than for the undoped material. Although the addition of Al has decreased the electrical resistivity from that of undoped material, the electrical resistivity increases with doping level between 0.5at.% to 1.5at.% Al content.

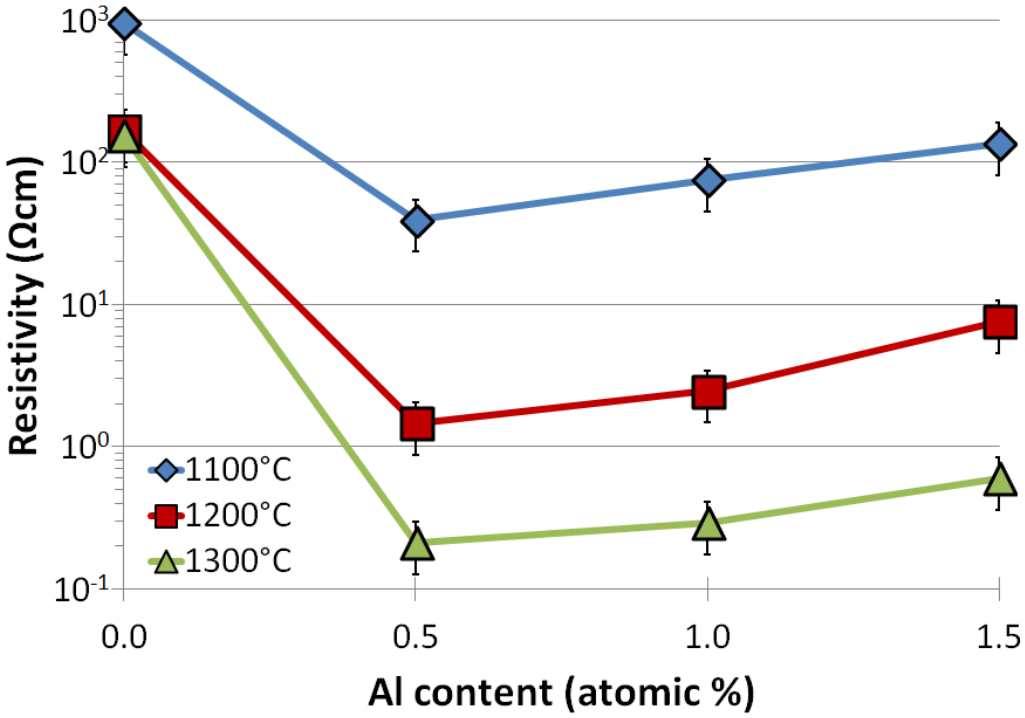

Figure 40: Resistivity of Al doped ZnO sintered for 8 hours at 1100°C, 1200°C, and 1300°C

The samples sintered at 1300°C have the lowest electrical resistivity, where a minimum resistivity of 0.2 Ωcm was obtained at a doping level of 0.5at.% Al content. The electrical resistivity of ZnO has been reduced by almost 3 orders of magnitude by introducing Al dopant into the system. The sintering temperature also has an impact, reducing the electrical resistivity by over an order of magnitude for each 100°C increase in sintering treatment temperature. To determine how the electrical resistivity is related to the degree of porosity, the porosity models from *Table 1* were fitted to the experimentally determined values of electrical resistivity and porosity for Al doped ZnO in order to determine the electrical resistivity of the matrix material. Fits of these curves are shown in *Figure 41*.

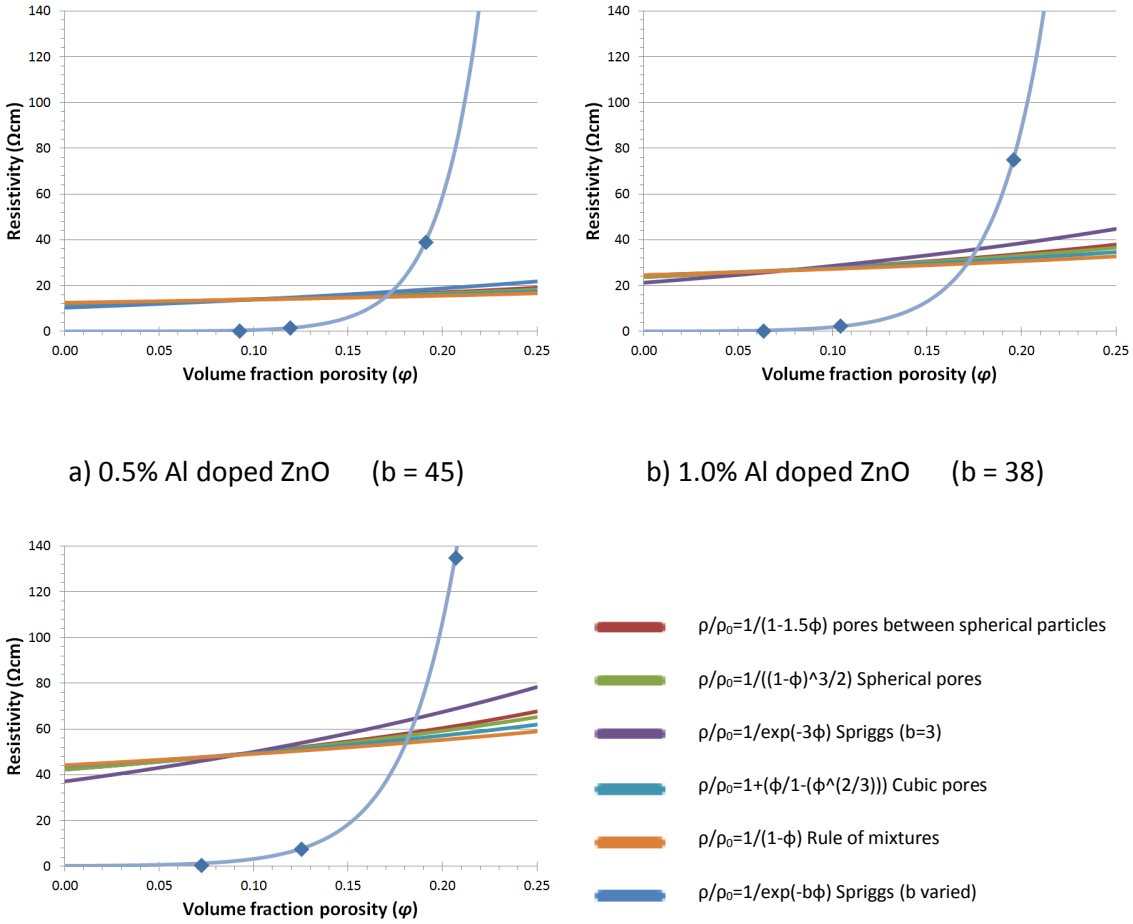

a) 0.5% Al doped ZnO (b = 45)

b) 1.0% Al doped ZnO (b = 38)

c) 1.5% Al doped ZnO (b = 35)

Figure 41: Least squares fitting of the curves described by each porosity model to the experimental values of electrical resistivity and porosity of Al doped ZnO sintered for 8 hours at 1100°C, 1200°C, and 1300°C with Al content of a) 0.5at.%, b) 1.0at.%, and c)1.5at.%

5. Electrical and thermal conductivity

The Spriggs model with varied *b* values of geometry fit the experimental the best as determined by the R^2 values in *Table 3*. From the cross sections of Al doped ZnO, *Figure 31*, and *Figure 32*, the geometry of the pores appears to remain consistent with increasing porosity. In order to confirm this assumption, the *b* values of the Al doped samples sintered at different temperatures were calculated and are shown in *Figure 42*.

Table 3: Parameters of each porosity model fitted to the experimental data of porosity and resistivity of sintered ZnO with 0.5at.% - 1.5at.% Al content.

Model	Al content (atomic %)	Matrix resistivity ρ_0 (Ωcm)	R^2
$\frac{\rho}{\rho_0} = 1/(1-1.5\phi)$	0.5	11.83	0.12
	1.0	23.68	0.16
Pores between spherical particles	1.5	42.24	0.16
$\frac{\rho}{\rho_0} = 1/(1-\phi)^{3/2}$	0.5	11.86	0.11
	1.0	23.72	0.14
Spherical pores	1.5	42.37	0.15
$\frac{\rho}{\rho_0} = 1+\frac{\phi}{1-\phi^{2/3}}$	0.5	12.29	0.09
	1.0	24.39	0.12
Cubic pores	1.5	43.82	0.12
$\frac{\rho}{\rho_0} = 1/(1-\phi)$	0.5	12.43	0.07
	1.0	24.55	0.10
Rule of mixtures	1.5	44.28	0.10
$\frac{\rho}{\rho_0} = 1/\exp(-3\phi)$	0.5	10.33	0.19
	1.0	21.16	0.25
Spriggs (*b*=3)	1.5	36.96	0.25
$\frac{\rho}{\rho_0} = 1/\exp(-b\phi)$	0.5	0.007 (*b*=45)	0.96
	1.0	0.042 (*b*=38)	0.98
Spriggs (*b* varied)	1.5	0.090 (*b*=35)	0.97

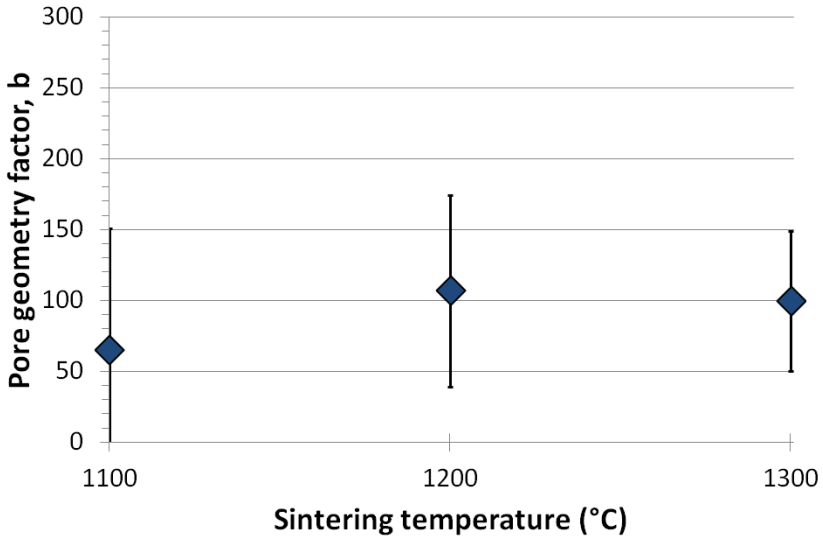

Figure 42: Pore geometry factor, b as a function of sintering temperature for Al doped ZnO

The geometries of the pores found for each doping level (*Figure 42*) are constant with sintering temperature within the calculated degree of uncertainty, this adds a degree of confidence that the geometry of the pores of Al doped ZnO do not change with increasing porosity which is confirmed by observations made on the microstructure in *Figure 31*, and *Figure 32*. Although the geometry factor is extremely high which indicates that the level of Al incorporation impacts upon the matrix resistivity, the geometry factor is more consistent which is in agreement with the SEM observations of the microstructure.

The matrix resistivity as predicted from the fit of the Spriggs porosity model (*b* varied) to the experimental data is shown in *Figure 43* as a function of Al content. The matrix resistivity increases with Al content and predicts a minimum value for of $7.0\times10^{-3}\Omega$cm for the matrix material with 0.5% Al content.

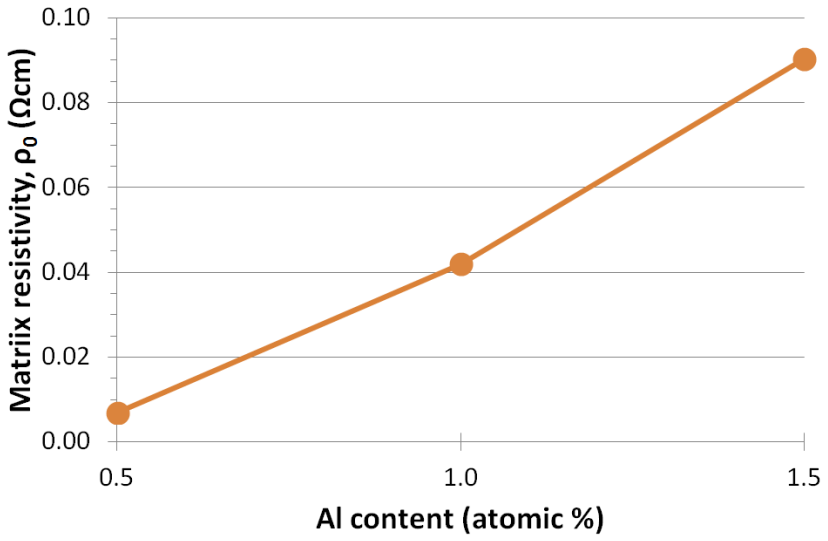

Figure 43: Matrix resistivity of Al doped ZnO as determined by fitting the Spriggs model of porosity to the experimental data for electrical resistivity and porosity.

Of the doping levels studied, a doping level of 0.5at.% Al gives the lowest value for electrical resistivity of 7.0mΩcm and is identified as the most suitable Al doping level for thermoelectric energy harvesting in terms of the electrical resistivity.

5.2. Thermal conductivity

5.2.1. Sb doped ZnO

The thermal conductivities of the Sb doped ZnO pellets were determined using the cut bar method as described in chapter 3. The experimentally determined values of thermal conductivity are presented in *Figure 44* as a function of temperature. The thermal conductivity of the sintered Sb doped ZnO samples remains constant with sample temperature in the range of temperatures studied.

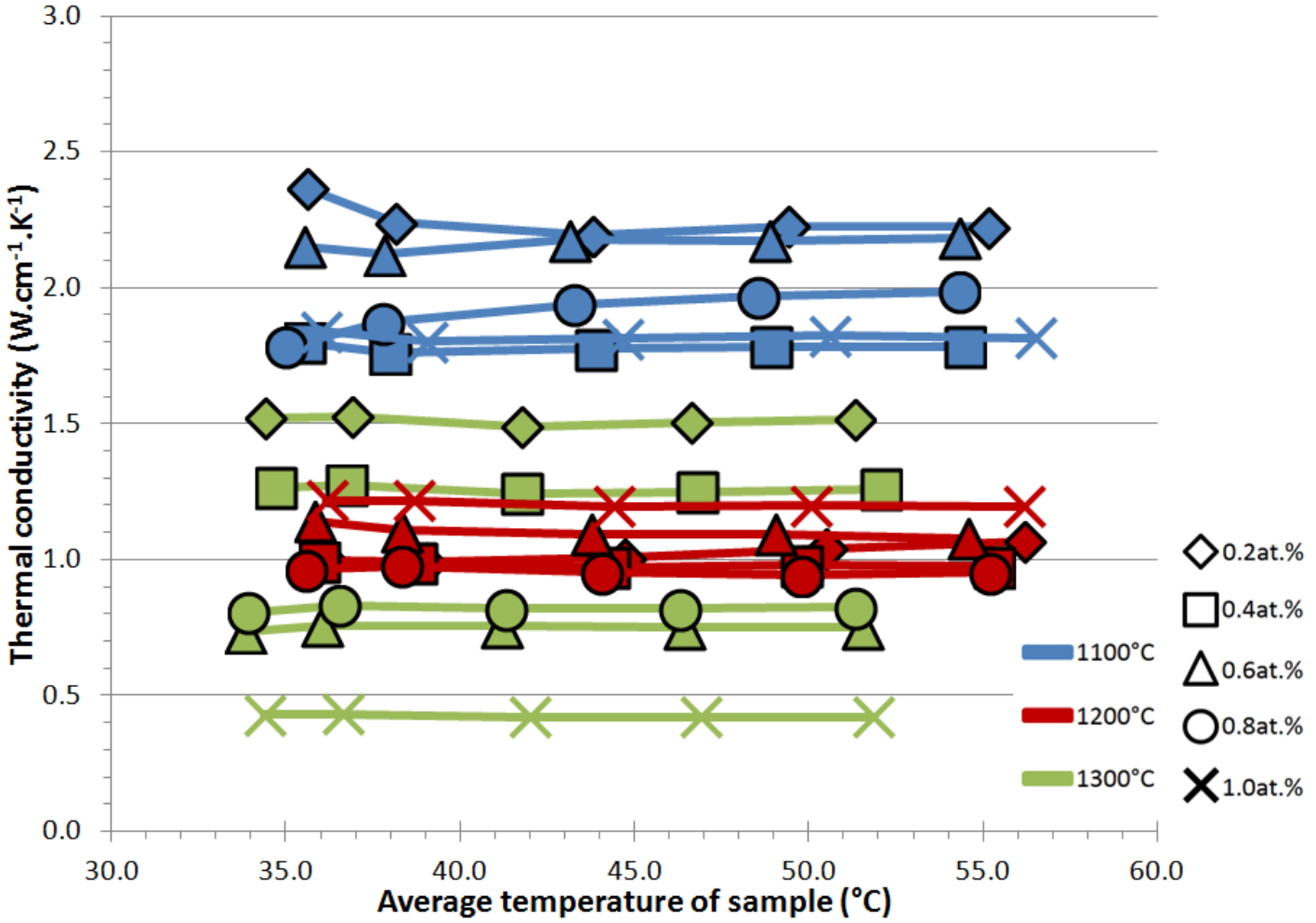

Figure 44: Thermal conductivity of 0.2at.% - 1.0at.% Sb doped ZnO sintered for 8 hours at 1100°C, 1200°C, and 1300°C

The majority of samples have a thermal conductivity in the range of (0.5-2.0)$W.m^{-1}.K^{-1}$. In order to determine how the thermal conductivity of the system changes with the level of doping, the average thermal conductivity obtained over the temperature range of 35 - 55°C is presented in *Figure 45* as a function of Sb content.

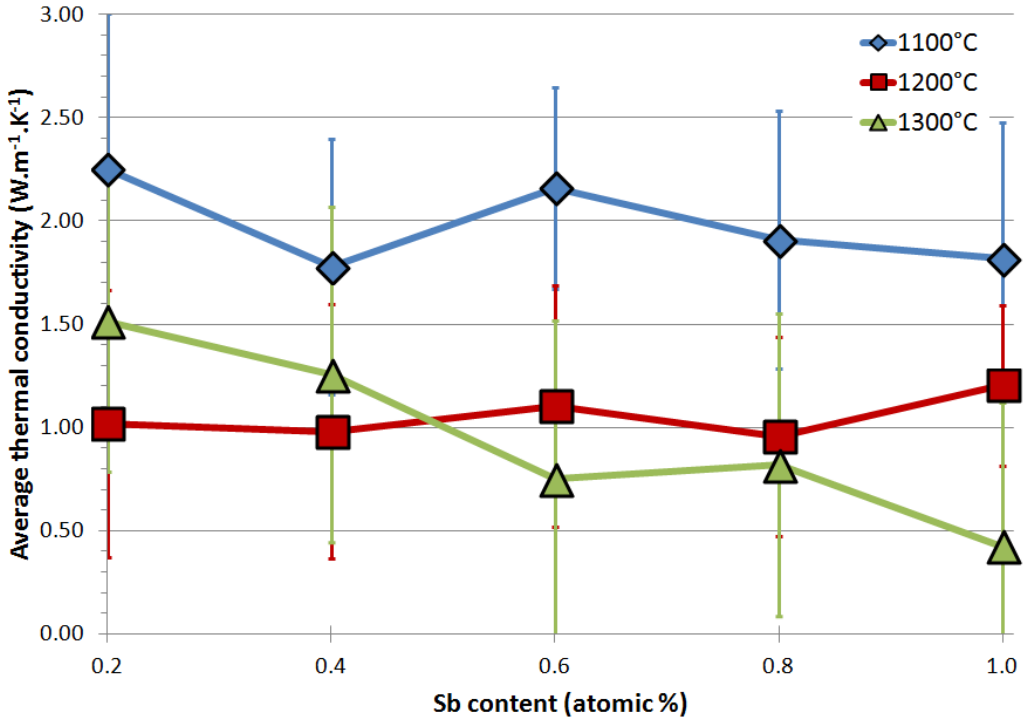

Figure 45: Thermal conductivity of 0.2at.% - 1.0at.% Sb doped ZnO sintered for 8 hours at 1100°C, 1200°C, and 1300°C

The thermal conductivity of the samples sintered at 1100°C and 1200°C is constant with the level of Sb content. There is a decrease in the thermal conductivity of approximately 1.0$W.m^{-1}.K^{-1}$ for samples sintered at 1300°C with increasing Sb content between 0.2% and 1.0%.

The thermal conductivity is influenced by the quality of grain boundaries and area of contact throughout the bulk material which means that for a given quality of grain boundary

increasing porosity should decrease the thermal conductivity as the presence of voids within the material adds an insulation character. Therefore it would be expected that the thermal conductivity of the samples sintered at 1100°C would be lower than the samples sintered for the same length of time at higher temperature due to the higher porosity of the samples sintered at 1100°C as established from *Figure 23*. The experimental findings from *Figure 45* contradict this, even though the standard error of the experimental system is large, the experimental values for thermal conductivity of the samples sintered at 1100°C is consistently higher than the samples sintered at higher temperatures across the range of doping levels studied.

In order to observe how the thermal conductivity is influenced by porosity, the thermal conductivity data is plotted as a function of porosity of the material, shown in *Figure 46*.

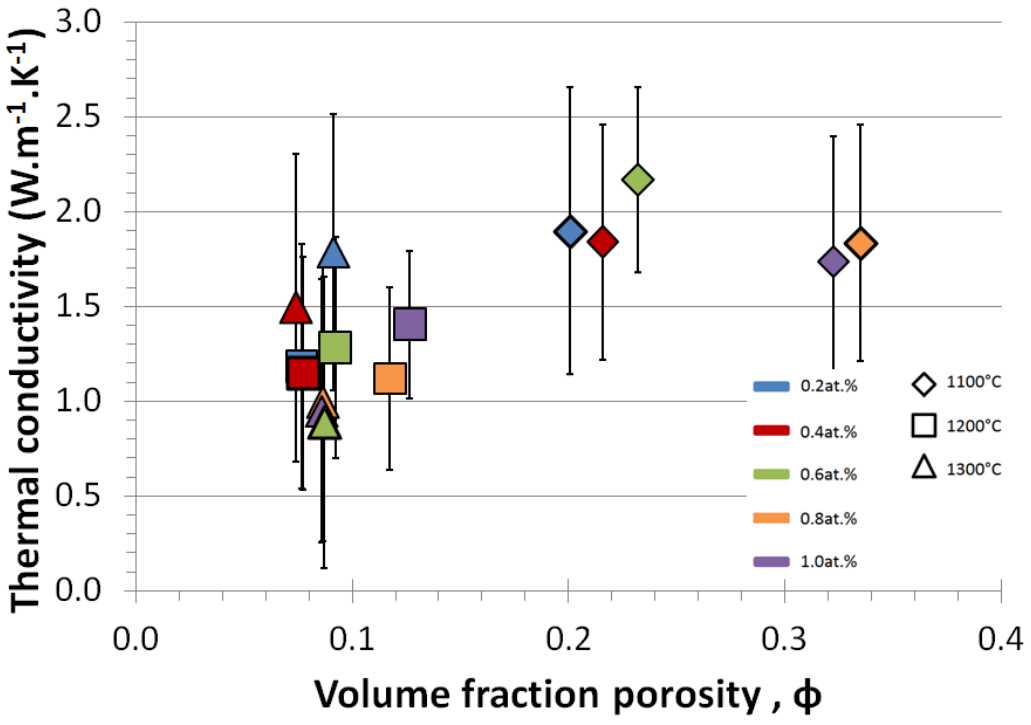

Figure 46: Thermal conductivity as a function of porosity for 0.2at.% to 1.0at.% Sb doped ZnO sintered for 8 hours at 1100°C, 1200°C, and 1300°C

There is a large uncertainty factor in the data, there is some evidence in the data presented in *Figure 46* that the thermal conductivity increases with porosity, however this is not confirmed due to the large error associated with the measurement setup. It was noted that the samples sintered at 1100°C had lower hardness than those sintered at higher temperatures. Although this was not quantified it could lead to the polishing procedure being more effective at producing a flat surface for the samples sintered at lower temperatures for better transmittance of thermal energy over the interface between the sample and the heat source and sink. Although it was ensured that the pellets were flat after the polishing stage, the softer samples may have been able to deform slightly to the minor irregularities of the surface interface of the heat source and heat sink producing a better thermal contact and leading to a higher measured thermal conductivity.

Another theory for there being a link between the increase in thermal conductivity with porosity is that absorbed water may have contributed to thermal conductivity. Olorunyolemi et al. (Olorunyolemi et al., 2002) measured the thermal conductivity of sintered ZnO powder with different particle sizes (micron, sub-micron, and nanometer). The thermal conductivity results show the opposite of what is expected for the different particle sizes, with the nanopowder having the highest thermal conductivity of the samples analysed. It was found by Olorunyolemi et al. that the nanopowder had a substantial amount of absorbed water, more than the sub-micron powder, which again had more than the powder with micron sized particles. The increase in thermal conductivity is related to the amount of absorbed water, which is influenced by particle size.

The error associated with the thermal conductivity measurements are large, meaning that there is a low degree of certainty of the trend observed. The thermal conductivity of the sintered compacts are in the region of 0.5 - 2.5 $W.m^{-1}.K^{-1}$ which is in agreement with literature values, which lie in the region of 1 $W.m^{-1}.K^{-1}$ (Özgür et al., 2006).

5.2.2. Al doped ZnO

The experimentally determined values of the thermal conductivity of Al doped ZnO are presented in *Figure 47* as a function of temperature. The thermal conductivity of the sintered Al doped ZnO samples remains constant with sample temperature in the range of temperatures studied.

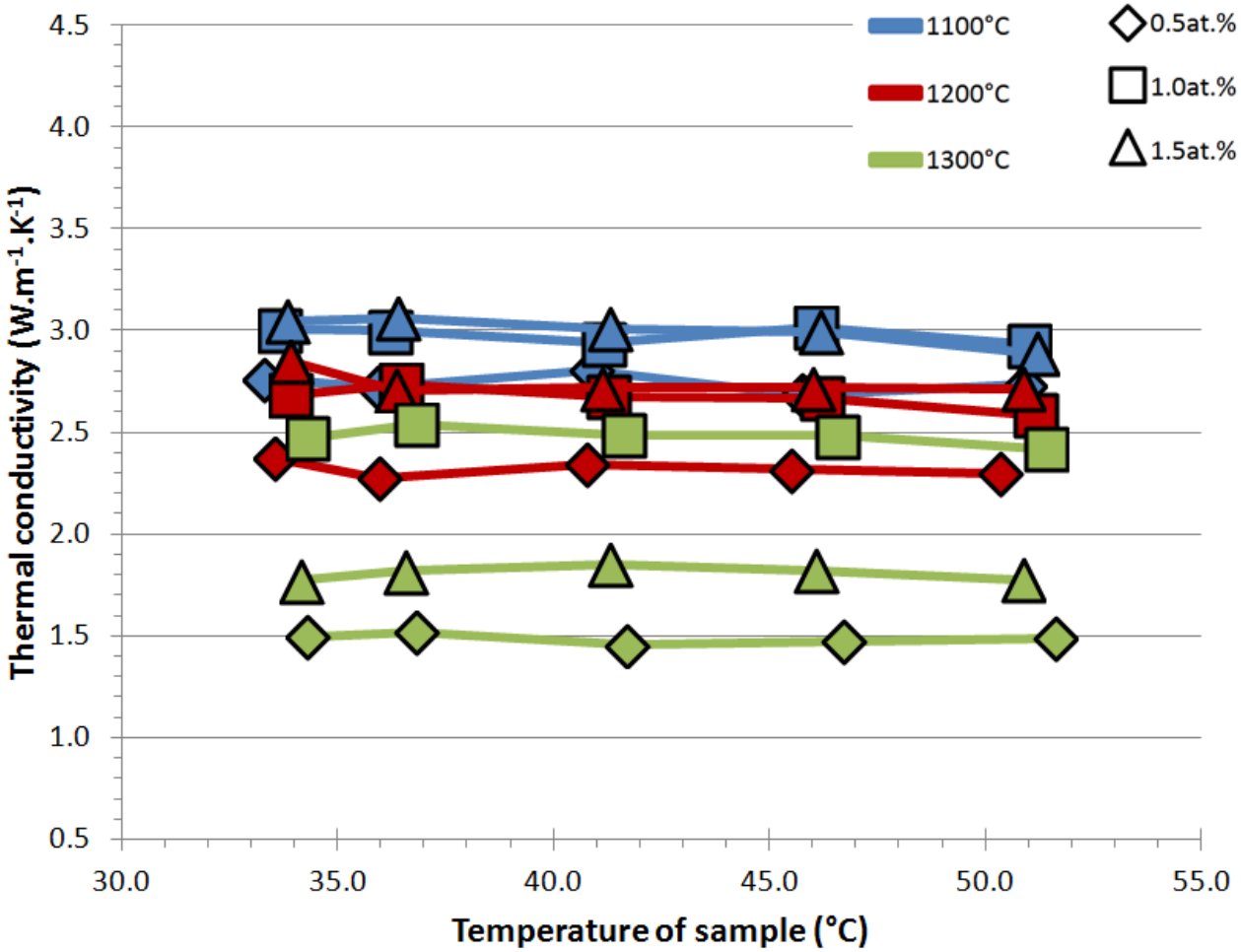

Figure 47: Thermal conductivity of 0.5% - 1.5% Al doped ZnO sintered for 8 hours at 1100°C, 1200°C, and 1300°C

The Al doped ZnO samples have average thermal conductivities in the range 1.0 - 4.0 $W.m^{-1}.K^{-1}$. The average thermal conductivity of Al doped ZnO is presented in *Figure 48* as a function of Al content.

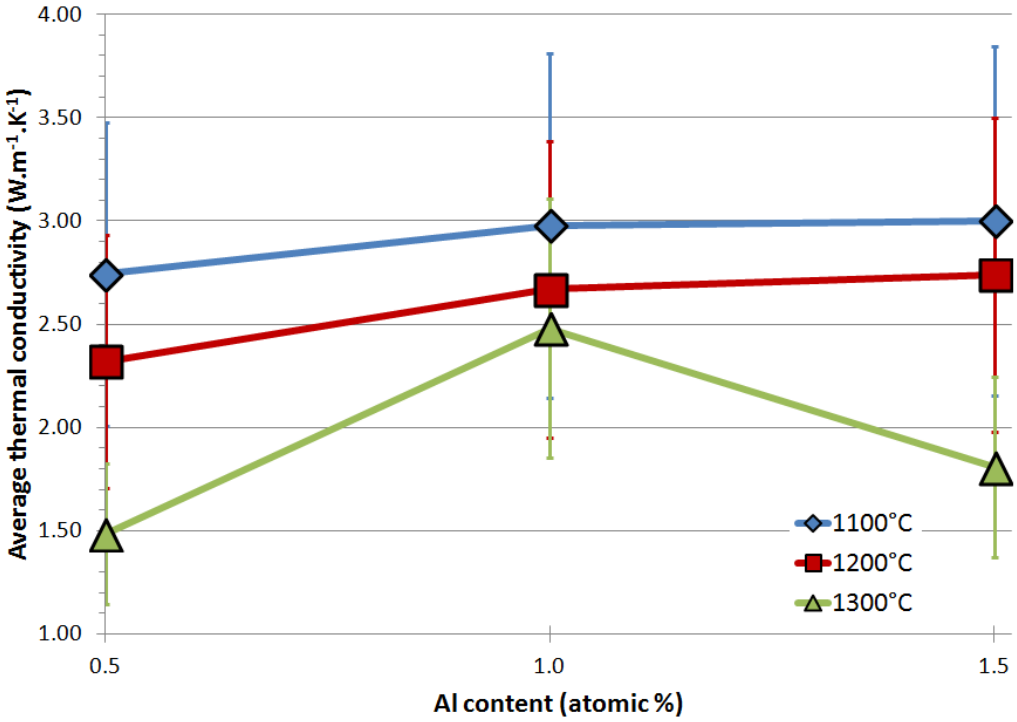

Figure 48: Thermal conductivity of 0.5% - 1.5% Al doped ZnO sintered for 8 hours at 1100°C, 1200°C, and 1300°C

The thermal conductivity of the Al doped samples sintered at 1100°C and 1200°C are broadly constant with Al content within the range of doping levels studied. The thermal conductivity of the samples sintered at 1300°C forms a maximum thermal conductivity of $2.5W.m^{-1}.K^{-1}$ at a doping level of 1.0% Al content.

In order to observe how the thermal conductivity of Al doped ZnO is influenced by the degree of porosity, the thermal conductivity data is plotted as a function of porosity of the material, shown in *Figure 49*.

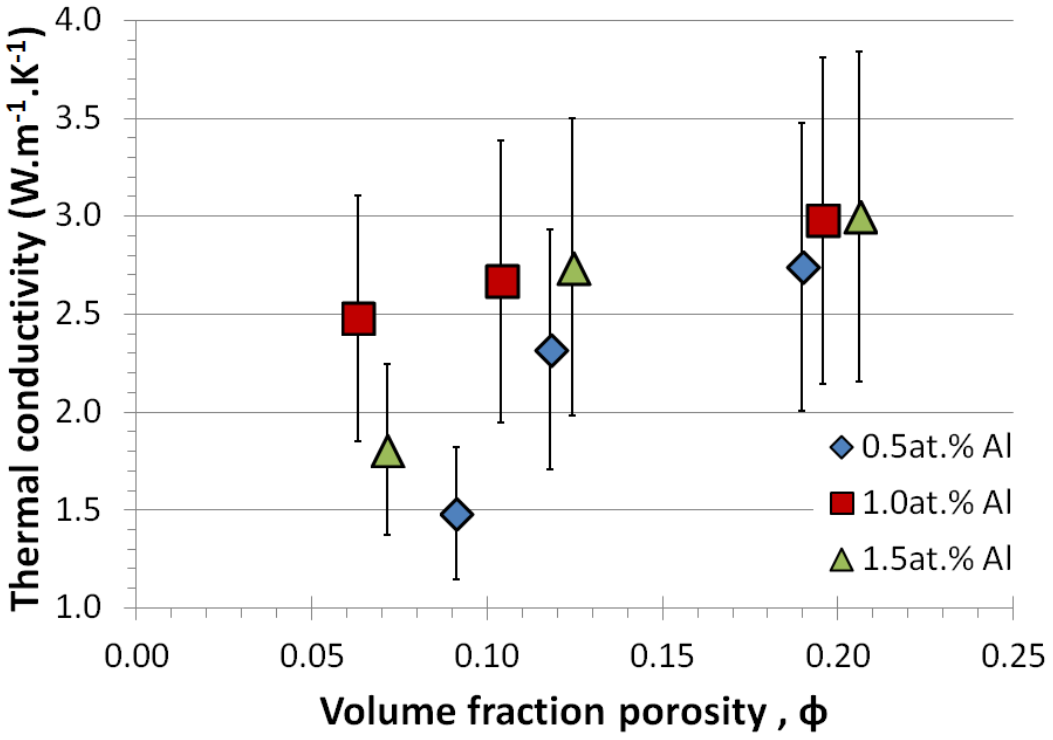

Figure 49: Thermal conductivity of Al doped ZnO as a function of porosity for 0.5at.% to 1.5at.% Al content sintered at 1100°C, 1200°C, and 1300°C

There is some evidence of the thermal conductivity of the Al doped ZnO compacts increasing with thermal conductivity in *Figure 45*, however due to the large error, any observed trends are not reliable. The thermal conductivities lie in the region of 1 - 4 $W.m^{-1}.K^{-1}$ which is in agreement with observations in the literature which lie in the region of 1 $W.m^{-1}.K^{-1}$ (Özgür et al., 2006). Han et al. (Han et al., 2014) investigated the thermoelectric properties of spark plasma sintered 2.0at.% Al doped ZnO and found thermal conductivities of 3 - 8 $W.m^{-1}.K^{-1}$ which are also in agreement with the thermal conductivities in *Figure 45*.

5.3. Summary

The sintering treatment has a profound impact upon the electrical resistivity of doped ZnO, with the electrical resistivity being reduced by approximately an order of magnitude for every 100°C increase in sintering treatment temperature. This is due to the degree of porosity of the material, which decreases with increasing sinter temperature. The electrical resistivity of Sb doped material is higher than undoped material and increases with Sb content while the electrical resistivity for Al doped ZnO is lower than undoped ZnO but increases with doping level. The lowest values for the resistivity were found at 1300°C for both the Al and Sb doped material with values of 3.4kΩ.cm at an Sb content of 0.4at.% and 0.21Ω.cm at an Al content of 0.5% which is over 4 orders of magnitude lower than the Sb doped sample. In terms of the electrical resistivity, the highest performing material was the Al doped material. By studying the fitted models of porosity of the experimentally determined values for resistivity and porosity, the lowest matrix resistivity was found to be 400Ω.cm for Sb content of 0.4% and 7.0×10^{-3} Ω.cm for Al content of 0.5%.

The electrical resistivity is an important factor to consider when choosing a material for thermoelectric energy harvesting, in order to maintain a high ZT value for the figure of merit, the electrical resistivity must be low. Although undoped material has the lowest electrical resistivity compared to the Sb doped material, dopant is required in order to achieve suitable thermoelectric behaviour, therefore a doping level of 0.2% to 0.6% Sb content is the most favourable range of Sb content. The highest performing Al doped material in terms of the electrical resistivity was at an Al content of 0.5%.

The thermal conductivity of the Al doped samples lie in the range of 1.0 to 4.0 $W.m^{-1}.K^{-1}$ and the Sb doped samples lie in the range of 0.5 to 2.5 $W.m^{-1}.K^{-1}$. The Al doping level with the highest thermal conductivity across the range of sintering temperatures was 1.0% with values in the range of 2.5 - 3.0 $W.m^{-1}.K^{-1}$ and the Sb content of 0.2% with thermal conductivity in the region of 1.0 - 2.3 $W.m^{-1}.K^{-1}$. In terms of the thermoelectric behaviour, a low thermal conductivity is desirable for improvement in ZT. The lowest thermal

conductivities obtained occurred at doping levels of 0.5% Al and 1.0% Sb with conductivities in the ranges of 1.5 - 2.7 $W.m^{-1}.K^{-1}$ and 0.4 - 1.8 $W.m^{-1}.K^{-1}$ respectively. These values are in agreement with the literature values which are in the region of 1 $W.m^{-1}.K^{-1}$ (Özgür et al., 2006).

6. Seebeck coefficient

6.1. Introduction

In this chapter the Seebeck character of the Sb and Al doped ZnO pellets is studied and the effect that the level of doping and the degree of porosity have upon the experimental values of the Seebeck coefficient are discussed.

The Seebeck coefficients were calculated from thermal and voltage measurements as detailed in *Chapter 3*. The Seebeck coefficients were calculated over a range of temperatures.

6.2. Doped ZnO

The Seebeck coefficients of Al doped ZnO and Sb doped ZnO, are shown in *Figure 50* and *Figure 51* respectively as a function of average sample temperature as the temperature of the hotplate was increased. All of the doped ZnO samples analysed have negative Seebeck coefficients across the temperature range examined, indicating n-type conduction.

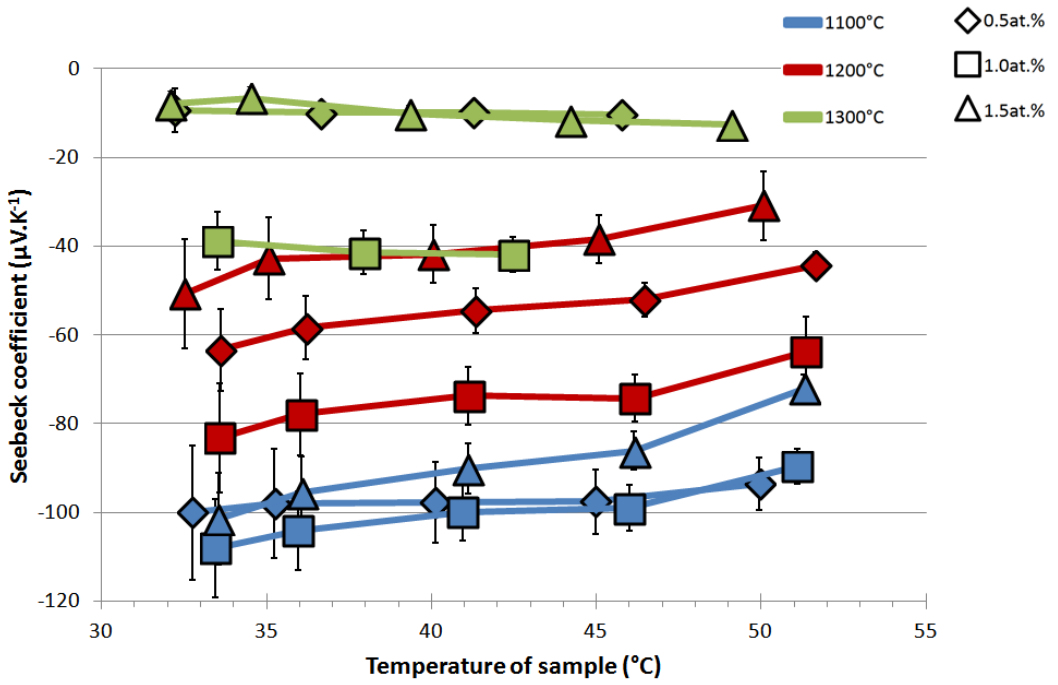

Figure 50: Seebeck coefficient as a function of temperature for doped ZnO with Al content of 0.5at.%, 1.0at.%, and 1.5at.% sintered for 8 hours at 1100°C, 1200°C, and 1300°C

The Seebeck coefficients for the Al doped ZnO samples are presented in *Figure 50* the Al doped samples sintered at 1100°C display the largest Seebeck coefficients at the range of temperatures conducted in this experiment, in the region of -90 to -110 $\mu V.K^{-1}$, followed by the samples sintered at 1200°C with Seebeck coefficients in the region of -40 to -80 $\mu V.K^{-1}$, while the samples sintered at 1300°C display the lowest values of Seebeck coefficient in the region of -10 to -40 $\mu V.K^{-1}$. This forms three distinct areas, the samples sintered at 1300°C, those sintered at 1200°C, and the highest performing sintered at 1100°C. Ohtaki (Ohtaki et al., 2009) found a room temperature Seebeck coefficient in the region of -80 to -100$\mu V.K^{-1}$ for bulk 2.0at.% Al doped ZnO which is in agreement with the Seebeck coefficients obtained here for samples sintered at 1100°C and 1200°C.

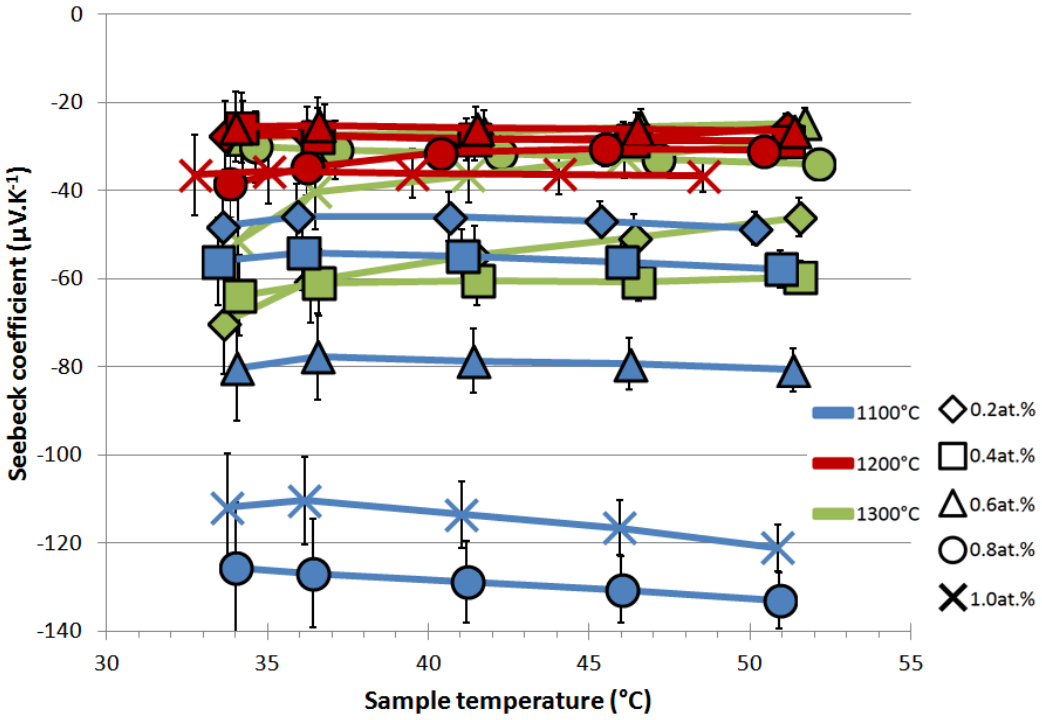

Figure 51: Seebeck coefficient as a function of temperature for 0.2at.% to 1.0at.% Sb doped ZnO sintered for 8 hours at 1100°C, 1200°C, and 1300°C

The Seebeck coefficients of the Sb doped samples in *Figure 51* remain broadly constant with temperature in the temperature range analysed. The samples sintered at 1100°C display the largest Seebeck coefficients in the region of -50 to -130 $\mu V.K^{-1}$, this agrees well with Park et al. (Park et al., 2008), who investigated the thermoelectric properties of Sb doped ZnO and found the seebeck coefficient for 0.5at.% - 5.0at.% Sb doped ZnO to be in the region of -40 to -170 $\mu V.K^{-1}$.

The n- type character of the Sb doped ZnO pellets analysed *Figure 51* is intriguing as group 5 elements are considered p- type dopants in the zinc oxide system. Undoped ZnO often displays n- type conductivity due to native donor effects and/or hydrogen incorporation (Fan et al., 2013b). This natural n-type character of ZnO could compensate for the p-type doping action of Sb within the system, however this is unlikely due to the magnitude of Seebeck coefficient obtained and that the magnitude of Seebeck coefficient would decrease with increasing Sb content if the natural n- type behaviour were being compensated for.

6. Seebeck coefficient

To establish p-type doping of ZnO, group V acceptor dopants are expected to generate acceptor states if incorporated subsitutionally on the oxygen sites in ZnO (Fan et al., 2013b), since the ionic radii of Sb^{3-} (2.44 Å) far exceeds that of O^{2-} (1.38 Å) it is more likely to occupy a Zn site (0.76 Å for Sb^{3+} and 0.6 Å for Zn^{2+}) and act as donors (Liu et al., 2012). (Wahl et al., 2009) found that the majority of Sb ions do indeed occupy Zn sites in ZnO. This donor behaviour could explain, at least in part, the n-type behaviour exhibited by ZnO when doped with Sb.

In order to explain the p- type behaviour observed by other authors, the large size mismatch of Sb compared to O the mechanism of p- type formation cannot be explained by simple substitution of Sb on the O site. Instead, the Sb forms an Sb_{Zn}-$2V_{zn}$ acceptor complex. The Sb energetically prefers to substitute into the Zn site (Sb_{Zn}) and induces two Zn vacancies (V_{Zn}) to form a Sb_{Zn}-$2V_{zn}$ complex. These complexes are considered to form a shallow acceptor level which leads to p- type behaviour.

(Liu et al., 2012) carried out experiments on Sb doped ZnO and found that Sb produced donor behaviour in ZnO which leads to n-type behaviour, at high Sb concentrations of above ~1 atomic %, the Sb was found to incorporate onto the O site or form point defect complexes (such as Sb_{Zn}-$2V_{zn}$) that act as acceptors which leads to p-type behaviour.

The level of Sb doping carried out in this study is ≤ 1.0at.% which is below the region where Sb is proposed to incorporate onto the O site or form defect complexes, this leads to the assumption that Sb has incorporated onto the Zn site and has resulted in donor behaviour which has lead to n-type conduction, resulting in negative Seebeck behaviour.

In order to observe how the doping level affects the measured Seebeck values, the Seebeck coefficients of the Al doped ZnO and Sb doped ZnO are shown in *Figure 52* and *Figure 53*, respectively, as a function of dopant content.

6. Seebeck coefficient

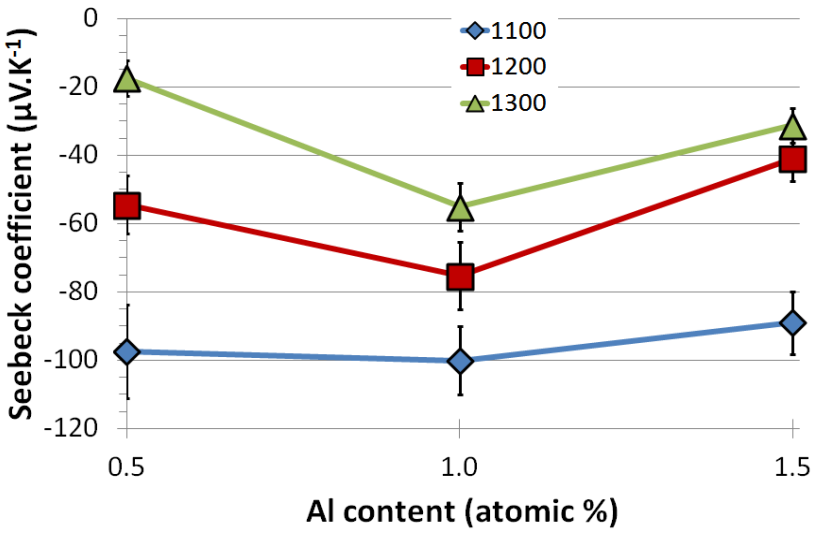

Figure 52: Seebeck coefficient as a function of Al content for samples of (0.5at.% to 1.5at.%) Al doped ZnO sintered for 8 hours at 1100°C, 1200°C, and 1300°C

.

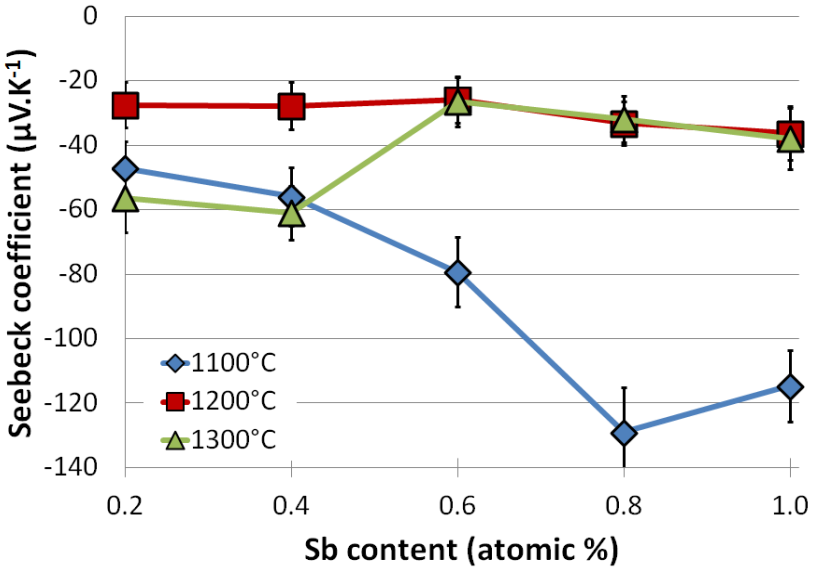

Figure 53: Seebeck coefficient as a function of Sb content for 0.2at.% to 1.0at.% Sb doped ZnO sintered for 8 hours at 1100°C, 1200°C, and 1300°C

The highest values of Seebeck coefficient for the range of sinter temperatures studied in the Al doped ZnO system in *Figure 52* occurs for the materials with 1.0at.% Al content, this

doping level forms a maximum value at all sintering temperatures analysed, with the highest performing sample with a Seebeck coefficient value of -100μV.K^{-1} for the 1.0at.% Al doped ZnO sample sintered at 1100°C. The Seebeck coefficients form three grouped regions which are visible in *Figure 52*, where there is a separation of samples sintered at 1100°C, 1200°C, and 1300°C, with the samples sintered at 1100°C having the highest Seebeck coefficients and 1300°C the lowest.

The Seebeck values of the Sb doped samples sintered at 1200°C is constant with increasing Sb content with a slight increase in value between 0.6at.% and 1.0at.%. The Seebeck values of the samples sintered at 1100°C, the highest performing of the three, increases with Sb content and forms a maximum of -130 μV.K^{-1} at an Sb content of 0.8at.%. The samples sintered at 1300°C start at -60 μV.K^{-1} at 0.2at.% and 0.6at.% then decreases in magnitude between 0.4at.% and 0.6at.% and follows the profile of the samples sintered at 1200°C.

It is interesting to note that the Seebeck coefficients for both the Al and Sb doped samples generally have larger magnitudes for the samples sintered at lower temperatures. Even with the same level of doping, the samples sintered at 1100°C display the highest values of Seebeck coefficients. In order to understand why this occurs, it is necessary to look at the material to see what differences there exists between the samples sintered at different temperatures that would cause the difference in the values of the obtained Seebeck coefficients.

A change in the crystallography or the presence of secondary phases in varying amounts in the material between samples could alter the thermoelectric behaviour and therefore result in a change in Seebeck coefficient. However there is little evidence of secondary phases present in the crystallography between the samples of the Al doped materials sintered at different temperatures from the XRD analysis (*Chapter 4*). There is broadening of the XRD peaks of Al doped ZnO which is related to the level of Al incorporation into the matrix material.

In order to determine if there is a dependence of the Seebeck coefficient upon the degree of dopant incorporation into the ZnO lattice, the Seebeck coefficients for the Al doped

materials are shown in *Figure 54* as a function of the width (FWHM) of the (101) peak of ZnO.

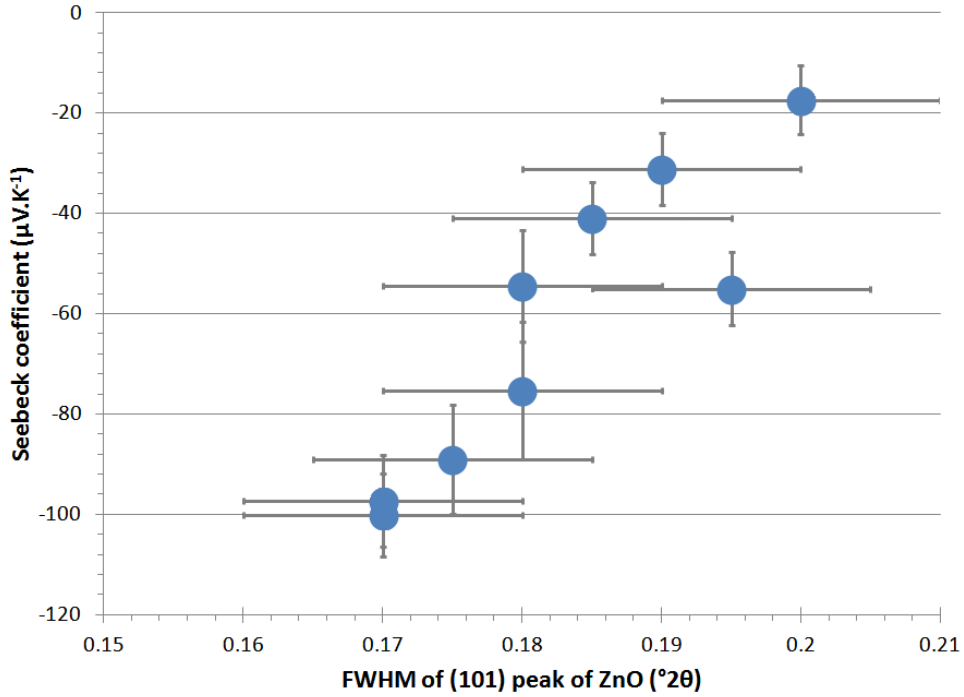

Figure 54: Seebeck coefficient as a function of the width of the (101) peak of ZnO for samples of Al doped ZnO sintered at 1100°C, 1200°C, and 1300°C

It can be seen in *Figure 54* that there is a correlation between Seebeck coefficient of Al doped ZnO and the width of the (101) peak of ZnO. This indicates that as more Al is incorporated into the ZnO lattice, the Seebeck coefficient is decreased in magnitude. It is therefore evident that there is evidence that the degree of Al incorporation into the material structure has an impact upon the Seebeck coefficient. However, given that the Seebeck coefficient decreases linearly with Log of carrier concentration (*Figure 55*), it is unlikely that a threefold increase in dopant level would account for the observed reduction in Seebeck coefficient. While broadening of the (101) peaks could indicate increased incorporation of Al into the crystal structure the maximum incorporation would still be limited to below 1.5at.% making it unlikely that this is a dominant mechanism. Therefore the difference in the obtained Seebeck values could be attributed to the morphology of the materials rather than the crystallography, as there is a significant difference in

microstructure between samples as observed from the SEM micrographs taken from the fracture cross sections. The two main differences in microstructure between the samples are the level of porosity present, and the size of the grains.

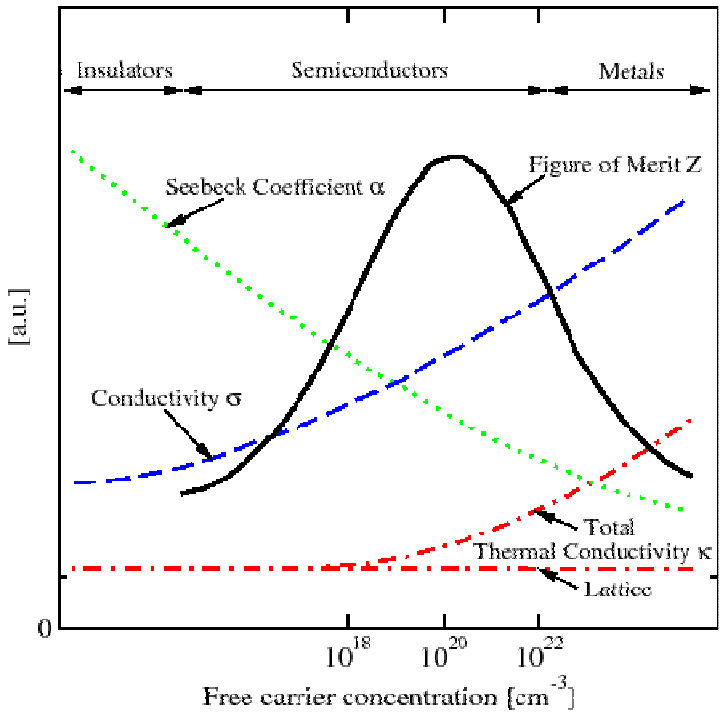

Figure 55: Seebeck coefficient, conductivity, thermal conductivity, and figure of merit with respect to free carrier concentration (Dughaish, 2002)

Gao et at. (Gao et al., 2010) investigated the impact of grain size on the Seebeck coefficient of bulk polycrystalline thermoelectric materials. Based on the Boltzmann transport equations of electrons, and the scattering effect of electrons at the grain boundary, a theoretical model of the Seebeck coefficient within polycrystalline thermoelectric materials was proposed and applied to the grain size effects upon the Seebeck coefficient. Gao found, based on the hypothesis that the Seebeck coefficient was controlled by transmissivity and mean free path of electrons, that the Seebeck coefficient increases with the length of grains decreasing *Figure 56*.

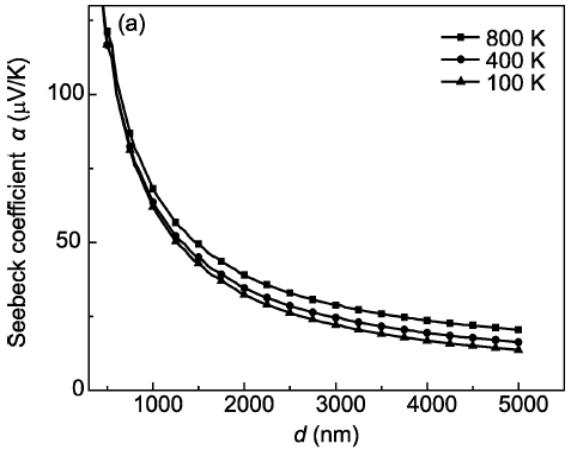

Figure 56: The Seebeck coefficients vs. the length of grains at different temperatures. From (Gao et al., 2010)

The Seebeck effect can be altered by the presence of interfaces due to the energy filtering of the charge carriers and is often quoted as a reason for the increased Seebeck coefficient in nanostructured bulk materials (Kinemuchi et al., 2010). Energy filtering occurs when electrons with low kinetic energies get stopped by the energy barrier at grain boundaries while high-energy electrons pass through them. Grain boundaries in polycrystalline semiconductors become electrically active as a result of charge trapping by gap states localised in the interface between adjacent grains. These interface states may be the result of impurities, dislocations or interfacial defects which can form a potential barrier that restricts the energy of carriers. For an n-type semiconductor the gap states can be filled by electrons from donor levels, this will lead to a negative charge accumulation at the interface and a positive charge region on either side of the interface. These space-charge regions create a double Schottky barrier at the grain-boundary-grain interface that acts as a barrier for electrons, *Figure 57*. Where the height of the potential barrier is close to the Fermi level, the low-energy electrons are screened out by the barrier, while high energy electrons are able to pass through the barrier which gives rise to the increase in Seebeck coefficient.

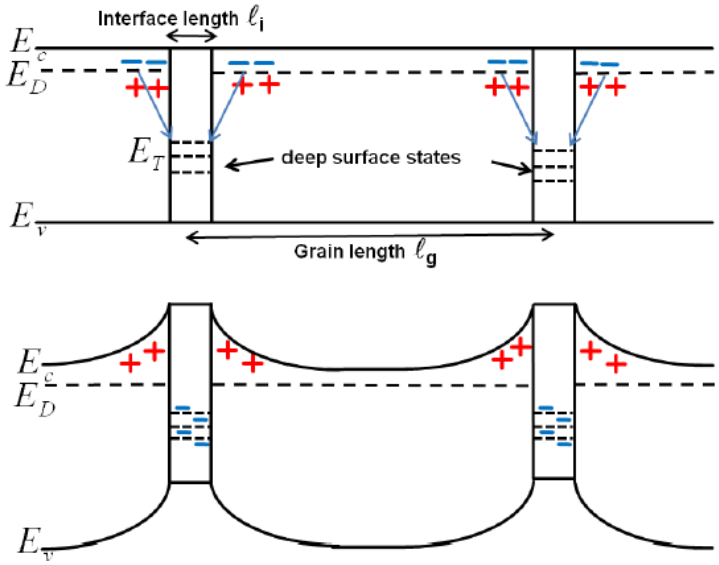

Figure 57: Band diagram before (top) and after (bottom) the generation of a double Schottky barrier. E_c is the bottom of the conduction band, E_D is the energy level of donors, E_T is the energy levels of trapping states, and E_v is the top of the valence band. Image from (Bachmann et al., 2012)

Only charge carriers with energy greater than the barrier height can pass through the barrier, this means that the carriers with energy below the barrier height are filtered out and therefore there is a net rise in the average energy of carriers passing through the material. The more grain boundaries that are present in the material, the greater the degree of energy filtering, therefore it is important to note that the surface area to volume ratio of grains is a driving factor of the energy filtering effect, as well as the width of the grains as grain size approaches the mean free path of the charge carriers.

In the doped ZnO system, the energy filtering effect could explain observations of the experimental data; at low sinter temperatures, were the grain size is small, larger values of Seebeck are observed. (Kinemuchi et al., 2010) observed the grain size dependence of Seebeck coefficient in ZnO, a higher Seebeck coefficient was observed for ZnO material with smaller grains (30nm) compared to material with larger grains (20µm). (Gao et al., 2010) compared experimentally determined values of Seebeck coefficient of $CoSb_3$ compounds as a function of grain diameter to theoretical results based on the energy filtering theory and found that theoretical investigation could sufficiently predict experimental findings. As the

grain diameter was decreased, the scattering effect of electrons in the grain boundary becomes stronger so the effect upon Seebeck coefficient increases. As the length of the grains increases, the opposite effect is shown and the Seebeck coefficient decreases.

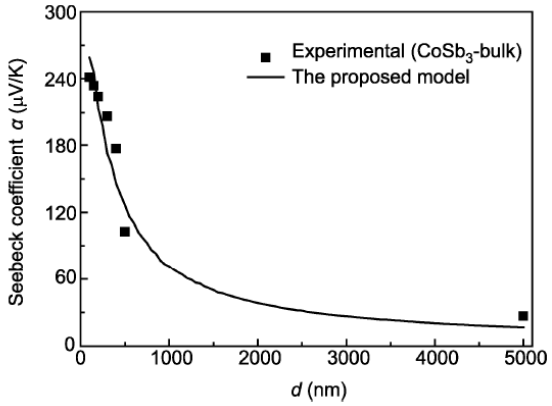

Figure 58: Comparison of theoretical investigation of $CoSb_3$ to experimentally determined values (Gao et al., 2010)

Nanostructures present in the material may also be used to increase the power factor by the energy filtering mechanism. When there are nanoscale particles present in the material such as different phases, carriers with low kinetic energies are stopped by the energy barrier at particle phase boundaries while high energy electrons pass through them (Narducci et al., 2012). This mechanism has been used to explain improvements in the Seebeck coefficient.

In the Al doped ZnO materials there has not been sufficient evidence of the presence of secondary phases as determined from the XRD analysis, therefore it is unlikely that nanoprecipitates of secondary phases are the cause for the increase in Seebeck coefficient. Instead grain size effects are likely to dominate (*Figure 59*).

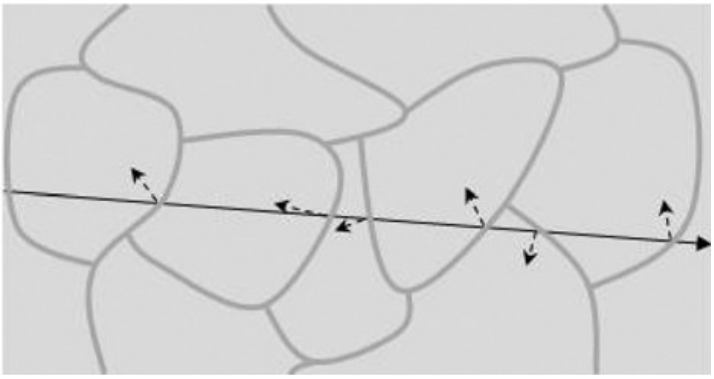

Figure 59: Energy filtering by grain boundaries in polycrystalline materials. All carriers are filtered out in energy.(Narducci et al., 2012)

In order to relate the grain size of the material to the Seebeck coefficients, the average grain diameter of the materials was calculated from data obtained from post image processing of the SEM micrographs of the sintered materials (*Chapter 4*). The grain size diameters for the Al doped ZnO and Sb doped ZnO are presented in *Figure 60* and *Figure 61* as a function of sintering temperature.

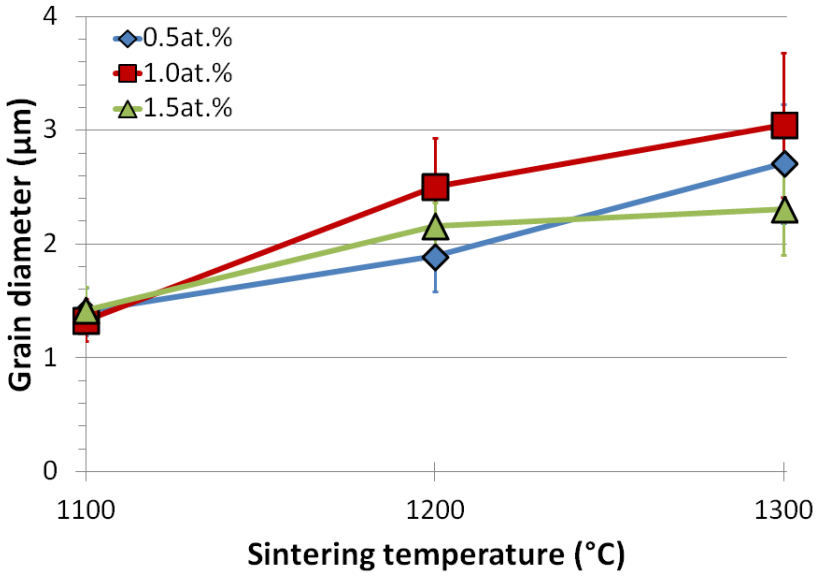

Figure 60: Average grain diameters obtained from the fracture cross section SEM micrographs of the Al doped pellets sintered for 8 hours at 1100°C, 1200°C, and 1300°C

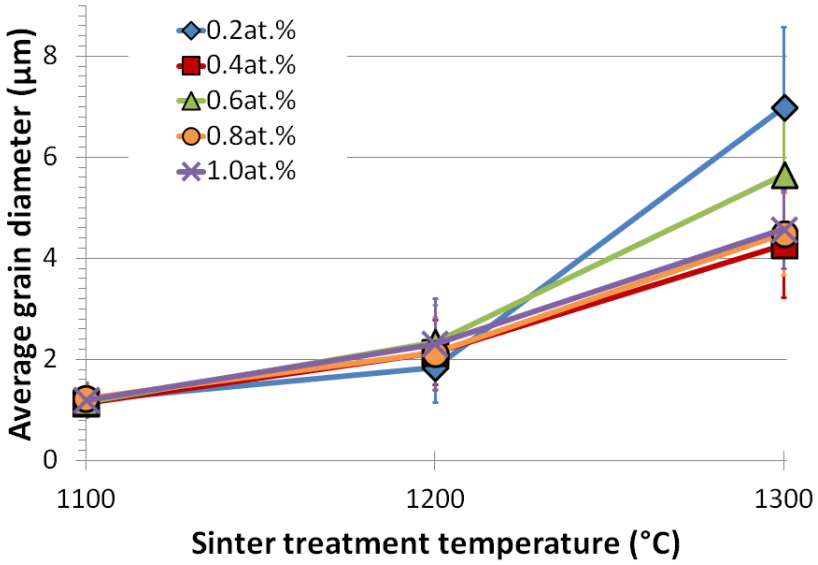

Figure 61: Grain diameter as a function of sintering temperature for 0.2at.% to 1.0at.% Sb doped pellets sintered for 8 hours at 1100°C, 1200°C, and 1300°C

As shown in *Figure 60* and *Figure 61*, the sintering temperature has an impact on the average grain diameter of the material, with the grain diameter increasing with sintering temperature. This is expected due to sintering mechanics where at higher sintering temperatures there is more energy available for the development of grains. The Al and Sb doped materials have similar grain diameters in the region of ~1µm at 1100°C and ~2µm at 1200°C.

In order to relate the grain diameter to the degree of porosity, the grain diameters of the sintered samples are presented in *Figure 62* and *Figure 63* as functions of porosity. There is a relation between the size of the grains and the level of porosity present in the material, as the level of porosity increases, the size of the grains decreases. This trend is related to the development of the material through densification and grain growth during the sintering process.

6. Seebeck coefficient

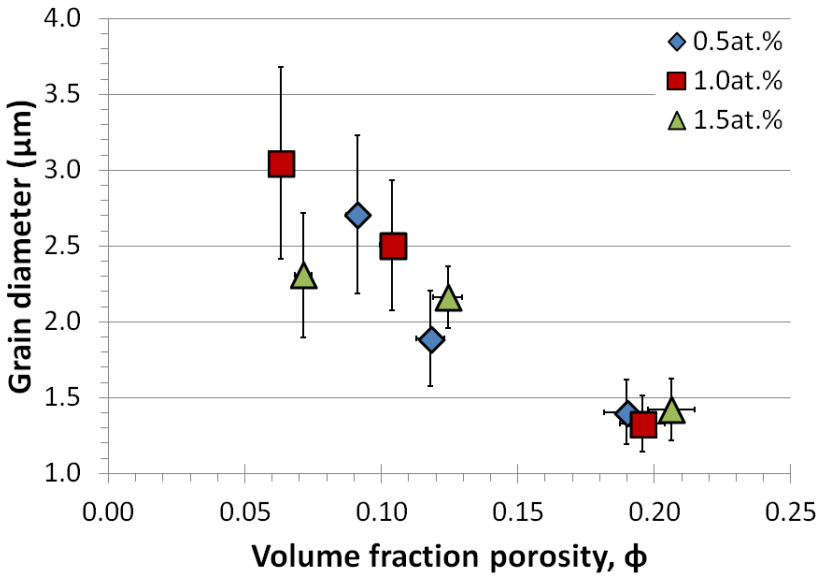

Figure 62: Average grain diameter as a function of porosity of 0.5at.% to 1.5at.% Al doped ZnO sintered for 8 hours at 1100°C, 1200°C, and 1300°C

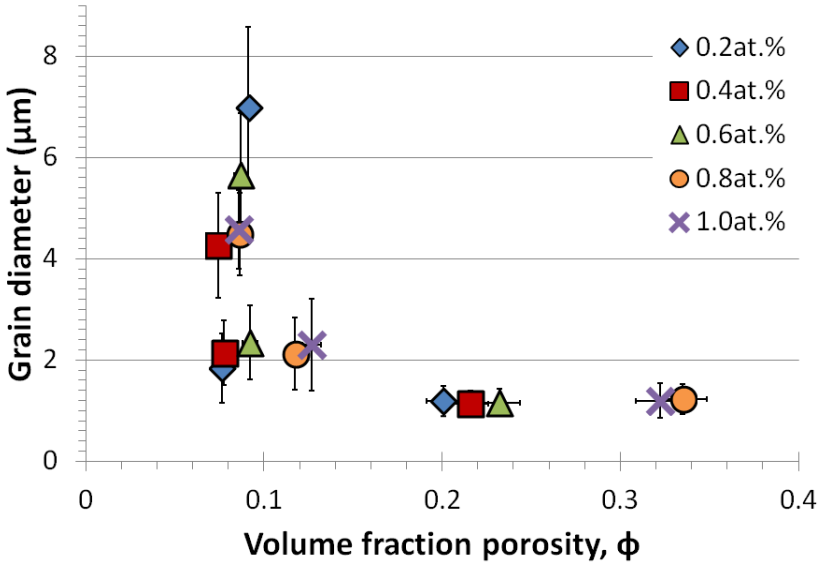

Figure 63: Grain diameter vs. porosity for 0.2at.% - 1.0at.% Sb doped ZnO sintered for 8 hours at 1100°C, 1200°C, and 1300°C

6. Seebeck coefficient

Figure 64 shows data taken from both *Figure 62* and *Figure 63* and plotted onto the same graph. It is clear that in this case the grain diameter - porosity relationship of both the Sb and Al doped systems overlap.

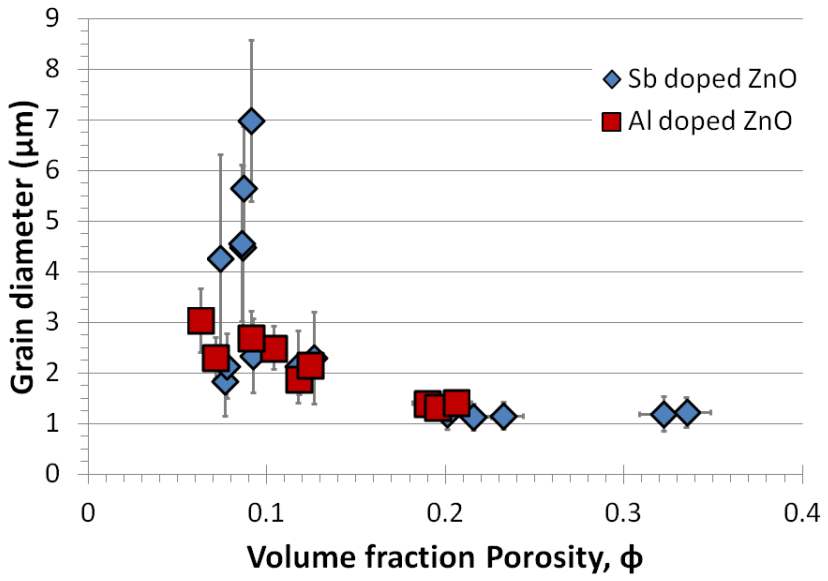

Figure 64: Grain diameter vs. porosity for 0.2at.% - 1.0at.% Sb doped ZnO and 0.5at.% - 1.5at.% Al doped ZnO sintered for 8 hours at 1100°C, 1200°C, and 1300°C

There is an increase in grain diameter with increasing sintering temperature which is expected as normal progression of grain growth occurs with increasing sinter temperatures. In order to observe how the grain size of the pellets relates to the obtained values of Seebeck coefficient, the average Seebeck coefficient of Sb doped ZnO and Al doped ZnO are presented in *Figure 65* and *Figure 66* respectively as functions of grain diameter.

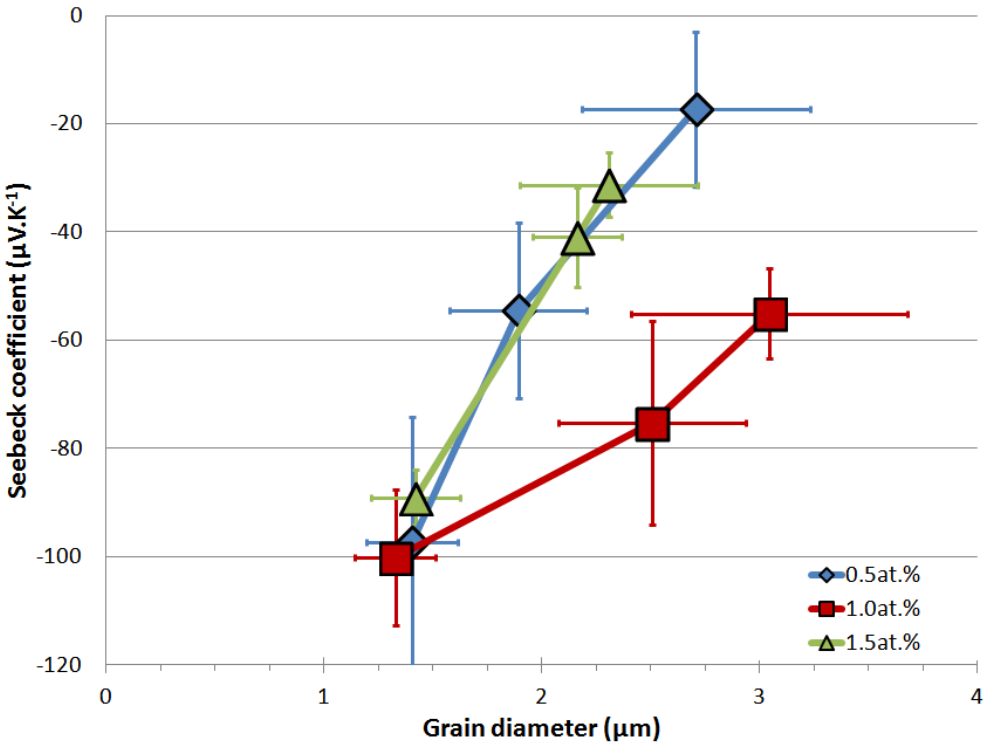

Figure 65: Seebeck coefficient as a function of grain diameter of Al doped ZnO pellets sintered for 8 hours at 1100°C, 1200°C, and 1300°C

The magnitude of Seebeck coefficient of the Al doped ZnO pellets decreases with increasing grain diameter, even an increase in diameter of only 0.9µm sees a decrease in the Seebeck coefficient by as much as (60 ± 12) $\mu V.K^{-1}$ in the case of the 1.5at.% Al doped specimen, *Figure 65*. The Seebeck coefficient of Sb doped ZnO in *Figure 66* is also sensitive to change in grain size at low diameters (<2µm), especially between 1.0µm and 2.0µm where the Seebeck coefficient decreases by nearly $100\mu V.K^{-1}$ from ~$-130\mu V.K^{-1}$ to ~$-35\mu V.K^{-1}$, this effect is by no means trivial.

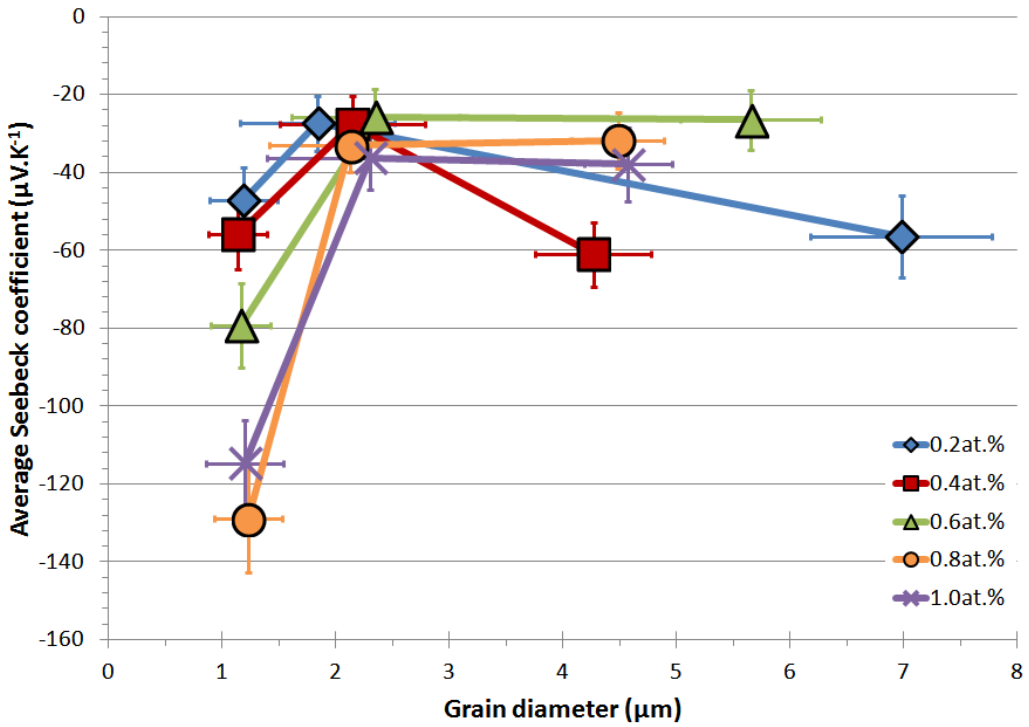

Figure 66: Seebeck coefficient as a function of average grain diameter of 0.2at.% to 1.0at.% Sb doped ZnO pellets sintered for 8 hours at 1100°C, 1200°C, and 1300°C

The behaviour of the Sb doped samples in *Figure 57* does not follow the same pattern as Al doped ZnO. Generally for Al doped ZnO the Seebeck coefficient is highest for all samples with small grain diameter. This is in agreement with the energy filtering effect, the Seebeck coefficient for the Sb doped material decreases and forms a minimum at grain diameter of approximately 2µm, and then increases slightly with increasing grain diameter. All samples with grain diameter in the region of 2.0 µm have a Seebeck value of (-30 ± 10) $\mu V.K^{-1}$. This indicates that there is a change in the thermoelectric properties of the Sb doped material as the average grain diameter approaches 2.0 µm.

As the length of the grains is large (> 2 µm), the size effect of the grains on the Seebeck coefficient is not significant. However when the grains are small (< 2 µm), the Seebeck coefficient sharply increases with grain length decreasing, *Figure 58*. This is mirrored in the Sb doped material, *Figure 66*, where the Seebeck coefficient sharply increases below grain

diameter of 2.0 µm. This indicates that the increase in Seebeck coefficient below 2.0 µm is a result of the energy filtering mechanism.

In order to determine if the observations in experimental data could be caused by the energy filtering effect, the experimental data for the Seebeck coefficient is plotted as a function of grain diameter for Al doped ZnO and Sb doped ZnO in *Figure 67* and *Figure 68*. The analytical predictions for the Seebeck behaviour from the energy filtering effect carried out by (Gao et al., 2010) *Figure 56* is included for comparison. The curve shape Gao proposed has been applied to the experimental data by the least squares fitting technique for the sintered samples to the average values of Seebeck coefficient and grain diameter for the samples sintered at 1100°C for the Al doped ZnO in *Figure 67*, and fitted to the samples sintered at 1200°C for the Sb doped ZnO in *Figure 68*. These clusters were selected because there is little deviation in the values of grain diameter and Seebeck coefficient between these samples, therefore a good fit for all theoretical predictions would pass through these regions and by doing so discrepancies between other data points and theory can be outlined and investigated. Although Gao based predictions upon bulk $CaSb_3$, with many calculation parameters different than in the ZnO system, the general shape of the curve would still hold.

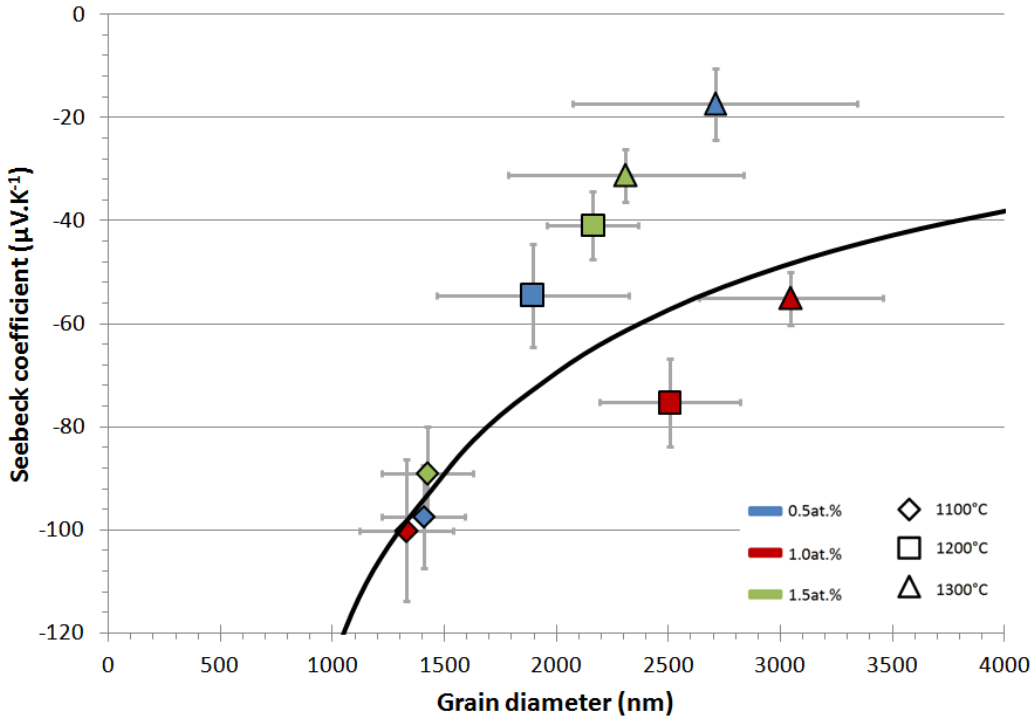

Figure 67: Seebeck coefficient as a function of grain diameter of Al doped ZnO pellets sintered for 8 hours at 1100°C, 1200°C, and 1300°C with theoretical prediction from Gao (Gao et al., 2010)

As can be seen in *Figure 67*, the data for the Al doped ZnO material does not match the prediction the curve. However, there are a number of competing factors, which may act to alter the Seebeck coefficient including grain size effects, and level of dopant incorporation.

In the case of the Sb doped material, *Figure 68*, the data points for the samples sintered at 1300°C and for some samples sintered at 1100°C fall below the curve prediction. The data generally follows the theoretical prediction in that the Seebeck coefficient decreases with increasing grain diameter then levels off however, it is apparent that the theory does not match well with the experimental data.

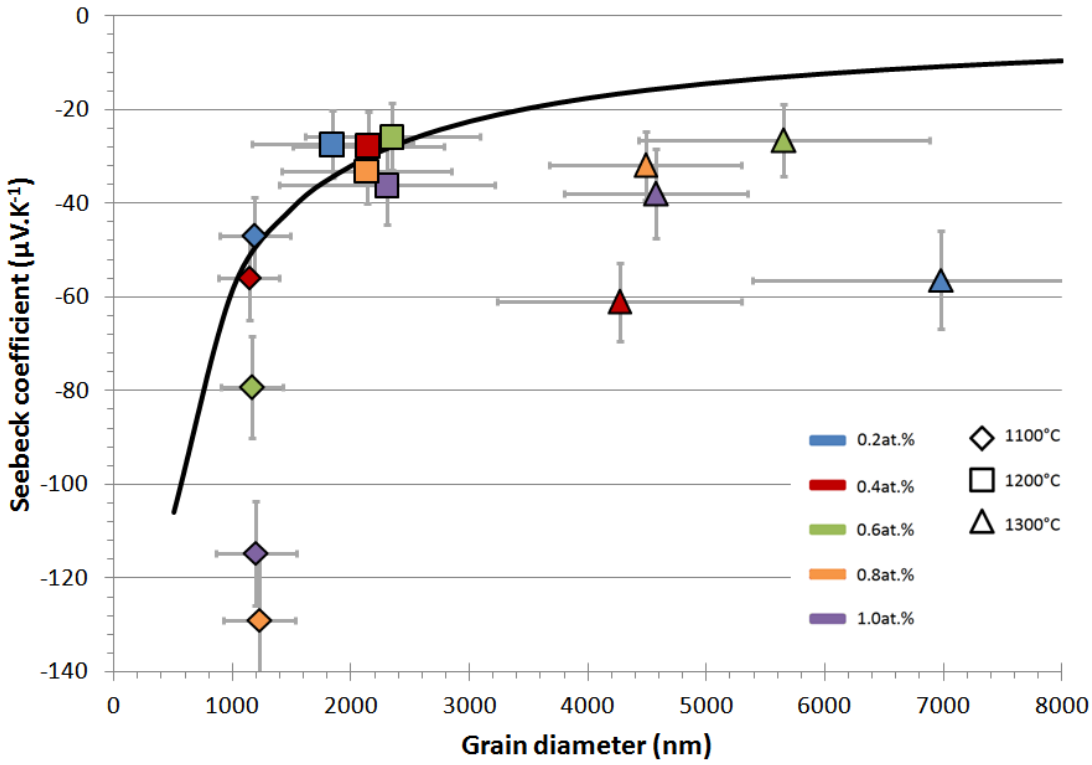

Figure 68: Seebeck coefficient as a function of average grain size of Sb doped ZnO sintered at 1100°C, 1200°C, and 1300°C for Sb content of 0.2at.%, 0.4at.%, 0.6at.%, 0.8at.%, and 1.0at.%.

The experimental data for the Sb doped material falls into three separate regions which are grouped by sintering temperature *Figure 68*. The samples sintered at 1100°C fall into one region, those sintered at 1200°C fall into the second region, and the samples sintered at 1300°C fall into the third region. The samples sintered at 1100°C all have little deviation in the average grain diameter, but have a large distribution in observed Seebeck coefficient. This means that the difference in Seebeck coefficient between the samples sintered at 1100°C cannot be attributed to grain size effects. These samples follow the trend that Seebeck coefficient increases with increasing Sb content, as discussed previously (*Figure 51*). All the data for the pellets sintered at 1200°C are clustered together with little deviation in Seebeck coefficient, or grain diameter, this means that the amount of Sb dopant has little impact upon the Seebeck coefficient at this sintering temperature. The samples sintered at 1300°C have a wide distribution in average grain diameter and a large distribution in

6. Seebeck coefficient

Seebeck coefficient. All values of Seebeck coefficient for the samples sintered at 1300°C have higher magnitudes than the theoretical prediction taken from the work carried out by Gao et al.

As the theoretical predictions only match the experimental data partially, this implies that there could be factors other than the energy filtering due to grain size effects, which vary among the samples which could be competing in the system to alter the Seebeck coefficient. Gao's prediction assumes that the transmissivity of electrons across the grain boundary and also the mean free path of electrons remain unchanged with increasing grain diameter. In the samples studied this may not be the case because as the sintering conditions were changed, the chemistry of the material also changes, with higher amounts of Al or Sb incorporating into the ZnO lattice at higher sintering temperatures. This may cause the mean free path and transmissivity of electrons to be different after different sintering temperatures and therefore not follow a standard prediction that assumes variables remain constant with grain size.

In order to determine if the deviation between the data and the theoretical prediction carried out by Gao can be related to the degree of dopant incorporation into the ZnO system, the difference between the theoretical prediction and data is plotted as a function of the FWHM of the (101) peak of ZnO for Al doped ZnO in *Figure 69*. By taking the values of the FWHM of the (101) peak for Al doped material and plotting alongside the deviation from the theoretical prediction, any trend will become apparent.

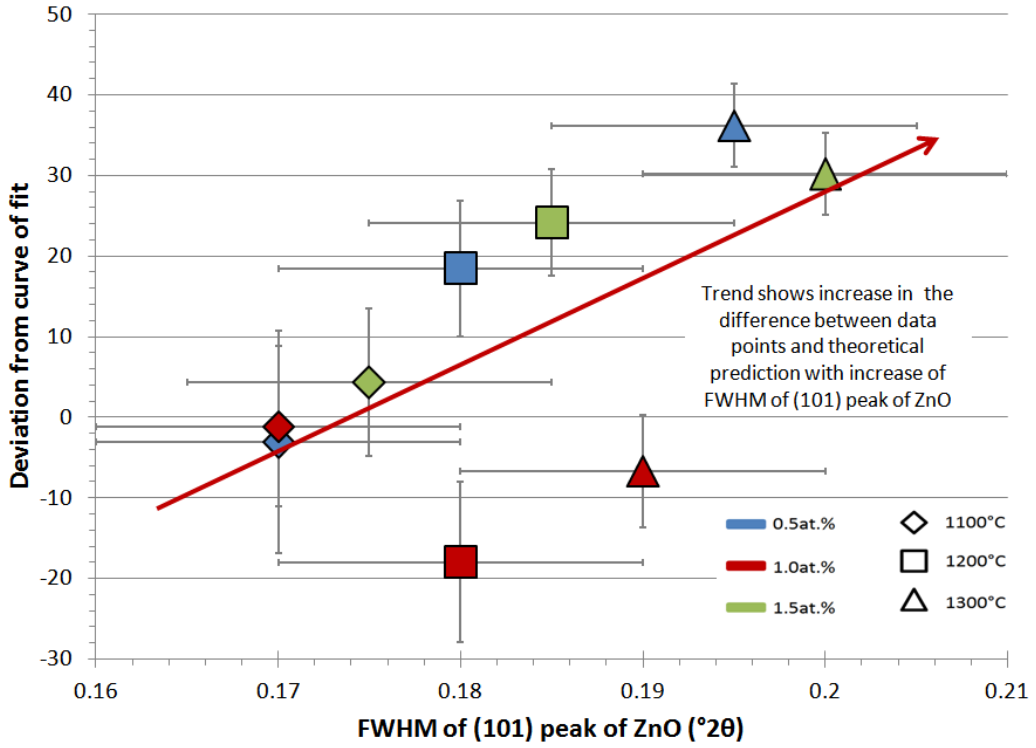

Figure 69: Deviation from the fit of predicted theory based on energy filtering as a function of the ratio of the width of the (101) peak of ZnO as determined from the XRD analysis for samples of Al doped ZnO sintered for 8 hours at 1100°C, 1200°C, and 1300°C with Al content of 0.5at.%, 1.0at.%, and 1.5at.%.

In *Figure 69* the graph shows that as more Al is accepted into the ZnO lattice, the magnitude of Seebeck coefficient becomes lower than expected according to the theoretical prediction by Gao. This means that increasing the Al incorporation into the ZnO unit cell is causing the Seebeck coefficient to become lower than it otherwise would be. This means that the Seebeck coefficient in this system is influenced by both grain size effects, and the level of Al acceptance into the ZnO lattice, with smaller grain sizes increasing the observed Seebeck coefficient and increases in Al acceptance decreasing the Seebeck coefficient.

The deviation in Seebeck coefficients of the Sb doped materials to theory are shown in *Figure 70* as a function of the XRD peak height ratio of secondary phase to ZnO determined in the XRD analysis.

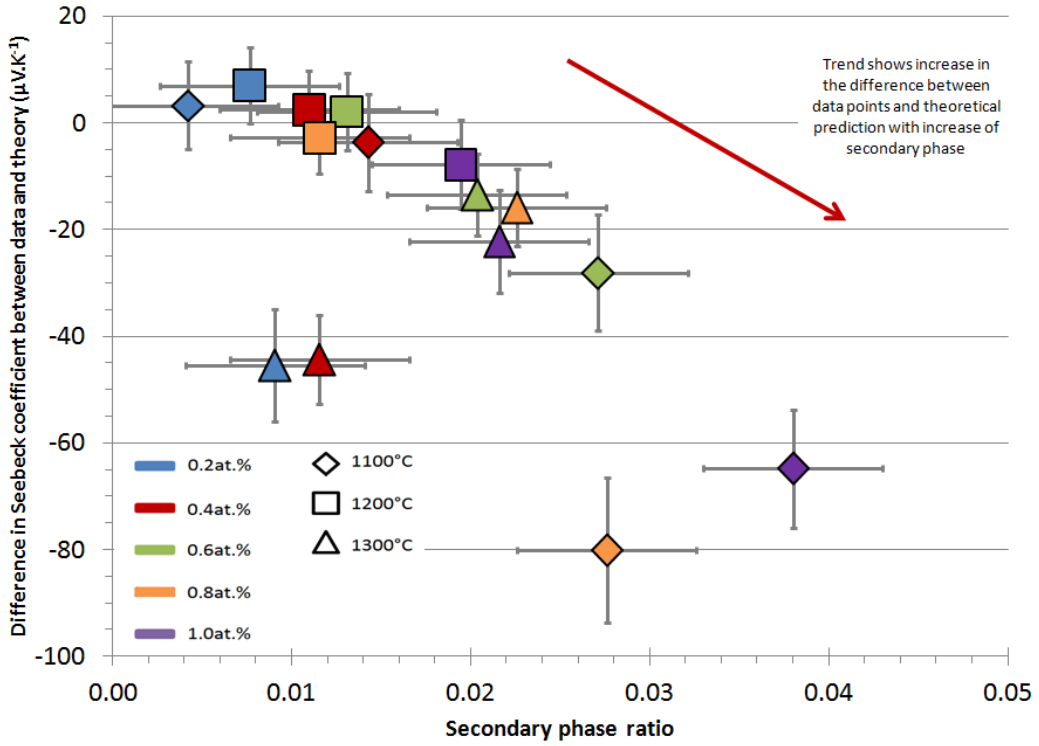

Figure 70: Deviation from the fit of predicted theory based on energy filtering as a function of the ratio of intensity of secondary phase to ZnO as determined from the XRD analysis for Sb doped ZnO sintered for 8 hours at 1100°C, 1200°C, and 1300°C with Sb content of 0.2at.%, 0.4at.%, 0.6at.%, 0.8at.%, and 1.0at.%.

For Sb doping (*Figure 70*) there is a general trend that the higher the secondary phase ratio of the Sb doped ZnO system the further below the theoretical prediction the data lies. This is an indication that the secondary phase in the system is contributing to increase the magnitude of the Seebeck coefficient of the materials.

6.3. Summary

6.3.1. Al doped ZnO system

Al is incorporated very effectively into the ZnO matrix such that no secondary phases are produced. The effect of incorporating Al into the ZnO structure is to reduce the Seebeck coefficient due to increase in carrier concentration. But within the system studied the grain size and porosity also play a significant role with small grains and higher levels of porosity leading to higher values of Seebeck coefficient.

6.3.2. Sb doped ZnO system

Unlike the Al doped systems, the addition of Sb dopants leads to the formation of secondary phases which appear to increase the Seebeck coefficient by an energy filtering effect akin to grain size effects. Higher levels of dopant lead to higher levels of secondary phase. As with Al doped systems grain size and porosity affect the observed Seebeck coefficients.

7. Thermoelectric characterisation

In this chapter, doped zinc oxide is studied as a candidate for thermoelectric energy harvesting by analysing its thermal properties in terms of the power factor and the figure of merit of the material.

7.1. Thermopower

The thermopower is a measure of the power that a thermoelectric material can provide per unit temperature difference, it is taken from the Seebeck coefficient and the electrical conductivity. The power factor, $S^2\sigma$ which represents the electrical contribution to the overall thermoelectric performance was calculated from the results obtained in the Seebeck and electrical resistivity studies, and is shown in *Figure 71* and *Figure 72* as a function of sample temperature for Al and Sb doped ZnO respectively.

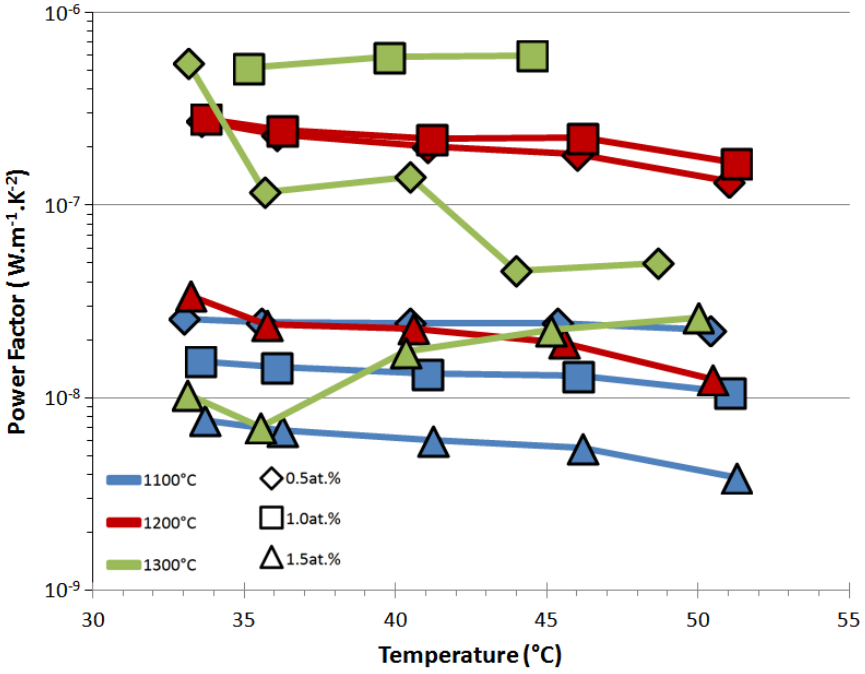

Figure 71: Power factors of $(Zn_{1-x}Al_x)O$ sintered for 8 hours at 1100°C, 1200°C, and 1300°C as a function of temperature for x = 0.005, 0.010 and 0.015

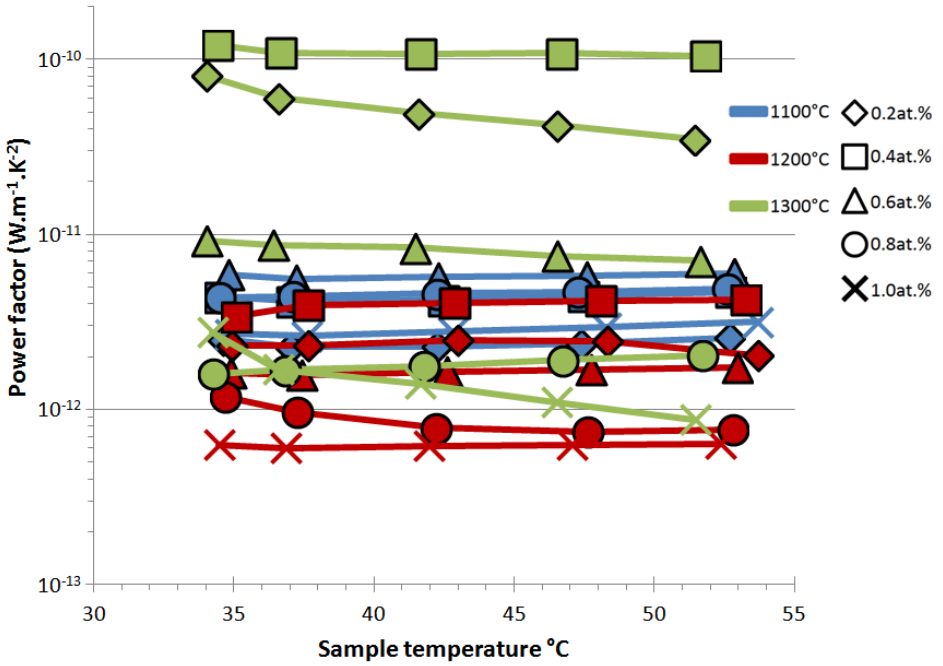

Figure 72: Power factors of Sb doped ZnO sintered for 8 hours at 1100°C, 1200°C, and 1300°C as a function of temperature for Sb content of 0.2at.%, 0.4at.%, 0.6at.%, 0.8at.%, and 1.0at.%

The power factors for Sb doped ZnO (*Figure 72*) are in the region of (1 - 100) × 10^{-12} $W.m^{-1}.K^{-2}$ which is lower than that of the Al doped ZnO samples (*Figure 71*) which are in the range of (4 - 600) × 10^{-9} $W.m^{-1}.K^{-2}$. All data was taken over a range of average sample temperatures from approximately 33°C to 53°C. The highest performing samples of Al doped ZnO attain power factors of (0.1 - 0.6) × 10^{-6} $W.m^{-1}.K^{-2}$, and the highest performing Sb sample attains power factors some three orders of magnitude lower in the region of 0.1 x 10^{-9} $W.m^{-1}.K^{-2}$. These values are much lower than literature values, which are in the region of 7 - 22 x 10^{-4} $W.m^{-1}.K^{-2}$ (Tsubota et al., 1997), (Ohtaki et al., 2009). This is in part due to the high electrical resistivity of the doped materials, which are in the region of 2 x 10^{-1}Ω.cm to 2 x 10^{2}Ω.cm for Al doped ZnO and 2 x 10^{3}Ω.cm to 3 x 10^{5}Ω.cm for Sb doped ZnO. The highest performing Sb doped material studied is 0.4at.% Sb sintered at 1300°C, and the highest performing Al doped sample of 1.0at.% Al sintered at 1300°C.

The power factor for the Al and Sb doped samples are shown in *Figure 73* and *Figure 74* respectively as functions of dopant content.

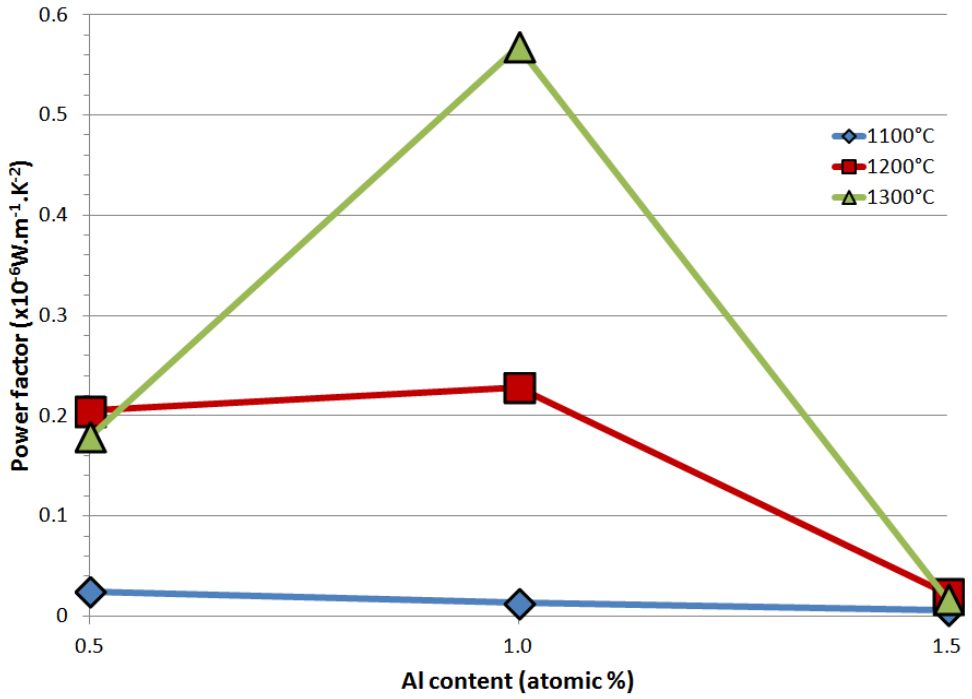

Figure 73: Average power factors from data from Figure 71 of $(Zn_{1-x}Al_x)O$ sintered for 8 hours at 1100°C, 1200°C, and 1300°C as a function of Al content for x = 0.005, 0.010 and 0.015

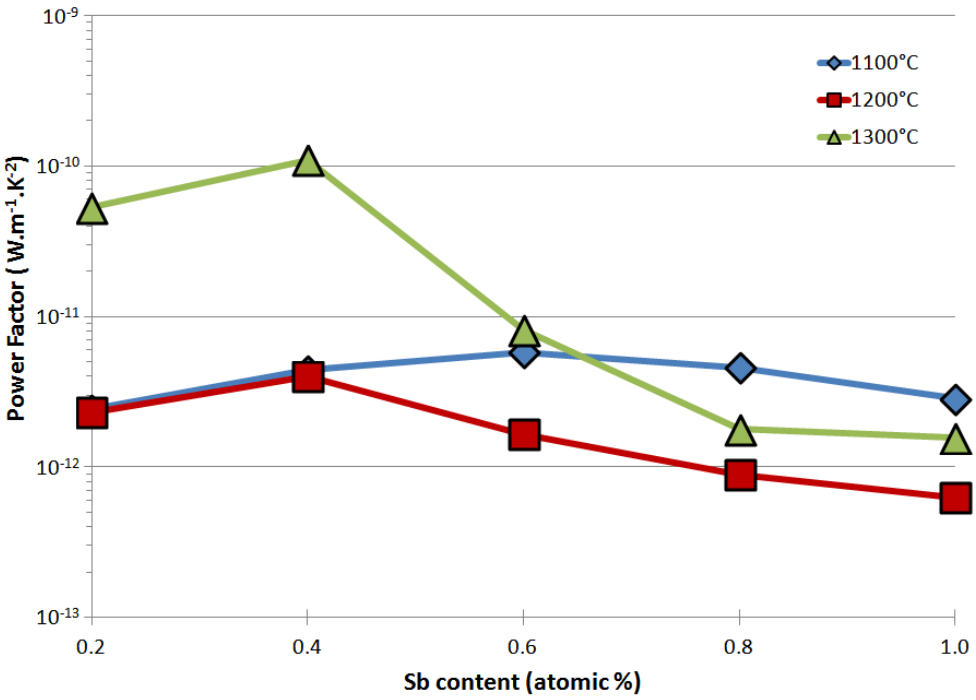

Figure 74: Power factors of Sb doped ZnO sintered for 8 hours at 1100°C, 1200°C, and 1300°C as a function of Sb content for Sb content of 0.2at%, 0.4at.%, 0.6at.%, 0.8at.%, and 1.0at.%

Although the samples sintered at 1300°C display the lowest Seebeck coefficients, and the samples sintered at 1100°C displaying the highest values of Seebeck coefficients (*Chapter 6*), the power factor does not follow this trend. This is because the electrical resistivity of the sintered material decreases with sintering temperature which means that the samples sintered at 1300°C have lower electrical resistivity than the samples sintered at lower temperatures (*chapter 5*). This compensates for the lower Seebeck values so much so that the 1.0at.% Al doped sample sintered at 1300°C in *Figure 73*, and the 0.2at.% to 0.6at.% Sb samples sintered at 1300°C are the highest performing samples of those tested in terms of the power factor.

When compared to values found in work carried out by (Tsubota et al., 1997), *Figure 75* there is a general trend that the power factor increases with Al content, however, this is not the case in *Figure 73*, where the 1.5at.% sample displays the lowest power factor for each set of sintering temperatures. Also in the room temperature region, *Figure 75*, the power

factor is in the region of ~5 x 10^{-4} $W.m^{-1}.K^{-2}$, whereas in *Figure 73*, the power factor is approximately three orders of magnitude lower in the region of 0.1 x 10^{-6} $W.m^{-1}.K^{-2}$. The Seebeck values are approximately (10 – 110) $\mu V.K^{-1}$ compared to the literature values which are in the region of (100-160) $\mu V.K^{-1}$ (Tsubota et al., 1997), (Ohtaki et al., 2009), however the main contribution to the difference in values of power factor arise from the difference in electrical conductivity. (Tsubota et al., 1997) found the electrical resistivity for their Al doped ZnO samples to be in the range of (1-10) x 10^{-3} Ωcm, and (Ohtaki et al., 2009) found the electrical resistivity of 2.0at.% Al doped ZnO to be 5.6 x 10^{-4} Ωcm at room temperature, while the electrical resistivity of 0.5at.% - 1.5at.% Al doped ZnO from this work was found to be in the region (0.1 – 100) Ωcm (*chapter 5*).

There are several factors that could account for the difference in the electrical resistivity between literature values and this work. The samples prepared by (Tsubota et al., 1997) were not pre calcined at 800°C and instead sintered at a higher temperature for longer - 1400°C for 10 hours, compared to 1100°C to 1300°C for 8 hours as carried out throughout this work, this could lead to a lower degree of porosity within the samples and also lower electrical resistivity due to larger grain size and lower number of scattering sites. Crucially the elevated temperature may also have enhanced the incorporation of Al into the ZnO structure. Significant reduction in resistivity is observed in this work when sintering temperature is increased from 1200°C to 1300°C suggesting that it may increase further at 1400°C.

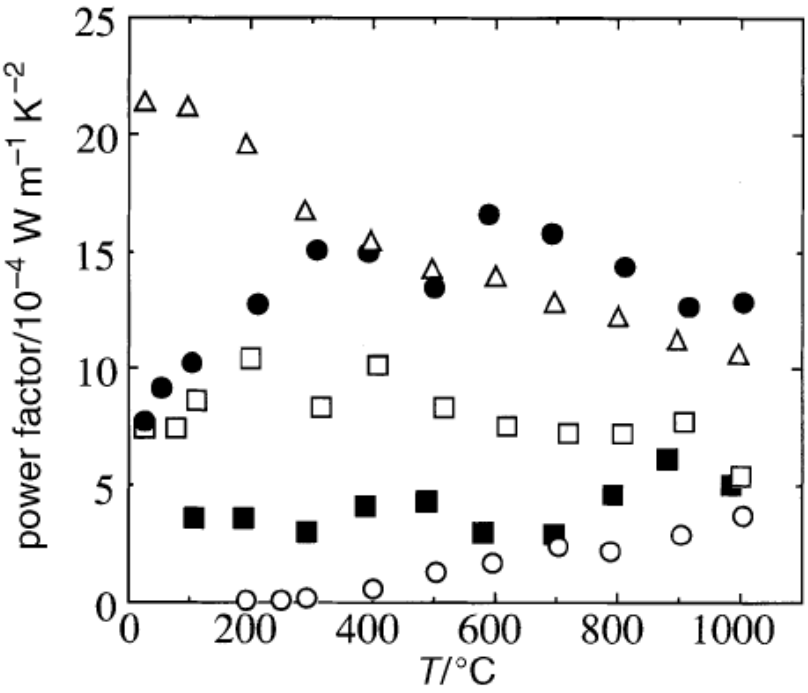

Figure 75: The power factors of ($Zn_{1-x}Al_x$) as a function of temperature for x = 0 (○), 0.005 (■), 0.01 (□), 0.02(●), and 0.05 (Δ) (Tsubota et al., 1997)

7.2. Figure of Merit

The dimensionless figure of merit, *ZT* was calculated from the power factor ($S^2\sigma$) and the thermal conductivity study and is shown in *Figure 76* and *Figure 77* as a function of average sample temperature for Al doped ZnO and Sb doped ZnO respectively.

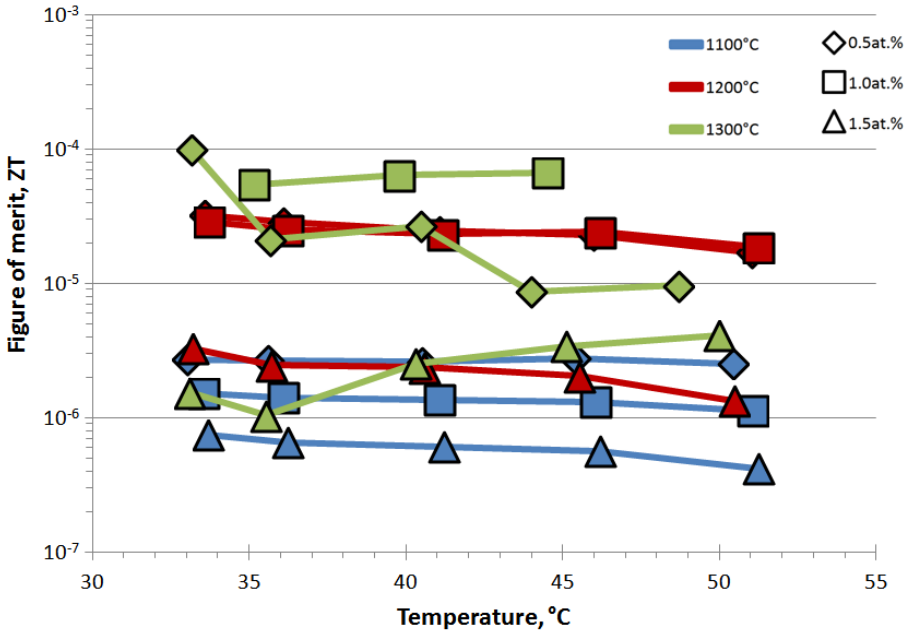

Figure 76: Dimensionless figure of merit, ZT of $(Zn_{1-x}Al_x)O$ sintered for 8 hours at 1100°C, 1200°C, and 1300°C as a function of temperature for x = 0.005, 0.010 and 0.015.

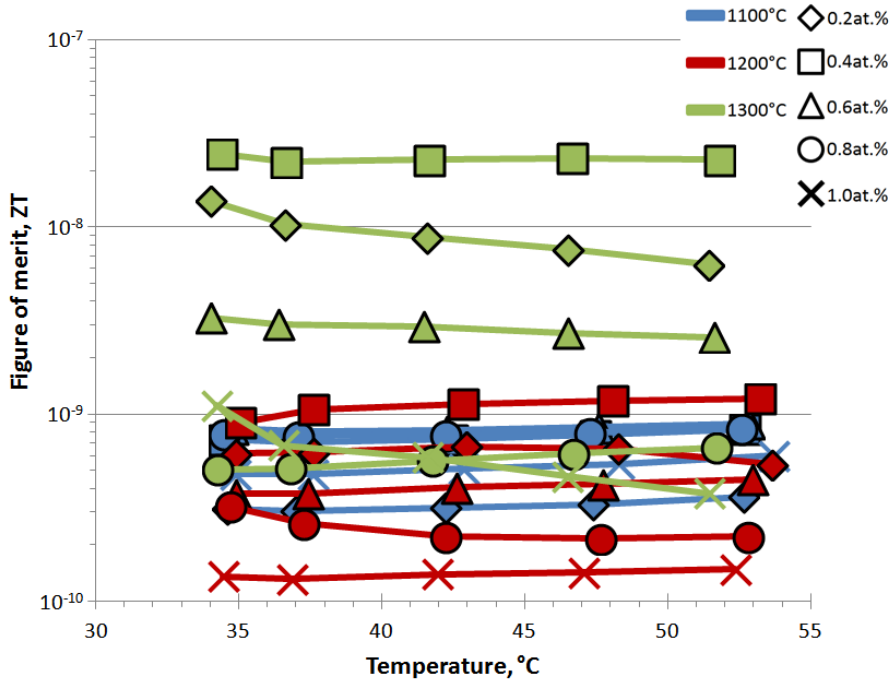

Figure 77: Dimensionless figure of merit, ZT of Sb doped ZnO sintered for 8 hours at 1100°C, 1200°C, and 1300°C as a function of temperature for Sb content of 0.2%, 0.4%, 0.6%, 0.8%, and 1.0%

The samples sintered at 1300°C have highest ZT values for both Al and Sb doped ZnO which is due to the lower electrical resistivity, while the sample with Al content of 1.0at.% (*Figure 76*) shows the highest ZT values of all the samples studied due to the Seebeck value of the 1.0 at.% sample being the highest of the Al doped samples sintered at 1300°C. The electrical resistivity strongly depends on the sinter temperature and changes by orders of magnitude between the sintering temperatures studied (*Chapter 5*). This has a large impact upon the figure of merit and in this case is the dominant factor controlling the figure of merit.

The majority of the Sb doped samples analysed (*Figure 77*) have a figure of merit in the region of (0.1 - 1.0) × 10^{-9}, the highest performing Sb doped ZnO materials have figure of merits in the region of (3 - 30) × 10^{-9}, over an order of magnitude greater. The higher performing samples were sintered at 1300°C, the performance is higher due to the reduced electrical resistivity of the 1300°C samples in comparison to the samples sintered at lower temperatures.

In order to compare the behaviour of the materials sintered at different temperatures in terms of their figure of merit, the figure of merit of the Al doped ZnO samples is shown in *Figure 78* as a function of Al content, and the Sb doped ZnO samples is shown in *Figure 79* as a function of Sb content.

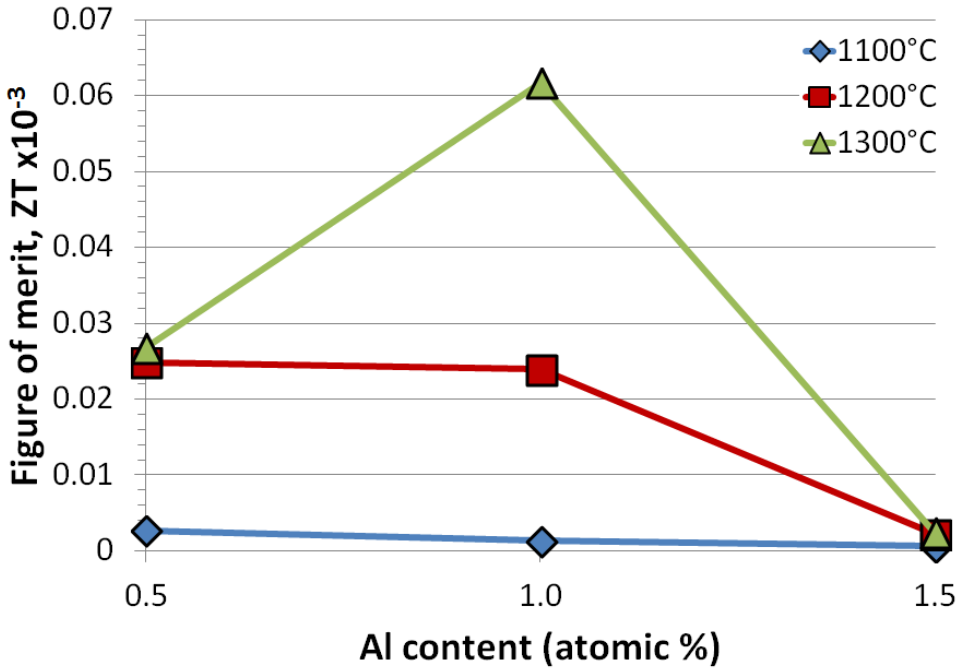

Figure 78: Average dimensionless figure of merit, ZT from data from Figure 76 of $(Zn_{1-x}Al_x)O$ sintered for 8 hours at 1100°C, 1200°C, and 1300°C as a function of Al content for x = 0.005, 0.010 and 0.015

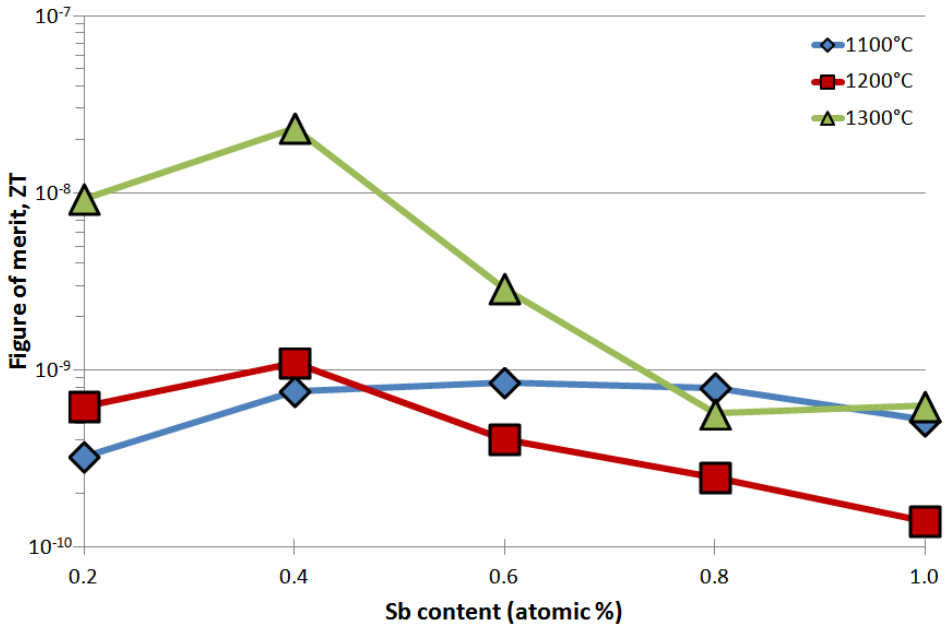

Figure 79: Dimensionless figure of merit, ZT of Sb doped ZnO sintered for 8 hours at 1100°C, 1200°C, and 1300°C with Sb content of 0.2%, 0.4%, 0.6%, 0.8%, and 1.0%

The figure of merit of the Sb doped samples (*Figure 79*) sintered at 1300°C increases from 0.01×10^{-6} to 0.02×10^{-6} between Sb content of 0.2% and 0.4%, then the figure of merit decreases with doping level. This trend is mirrored for the samples sintered at 1200°C, increasing from 0.6×10^{-9} to 1.0×10^{-9} then decreasing. The trend is initially followed for the sample sintered at 1100°C with the figure of merit increasing between 0.2% and 0.4% but then it stays at a constant level, then falling slightly between 0.8% and 1.0% Sb content. This difference in trend indicates that there is a change of the material between 0.4% to 0.8% that occurs between 1100°C and 1200°C which slightly alters the behaviour of the material, lowering the thermoelectric figure of merit.

The sintering temperature has had a profound impact upon the figure of merit, increasing it by over an order of magnitude from approximately 1.0×10^{-6} for the samples prepared at a sintering temperature of 1100°C to the region of 25×10^{-6} for the samples sintered at 1200°C and 1300°C at an Al doping level 0.5%. The figure of merit peaks at 60×10^{-6} for the 1.0% sample sintered at 1300°C and drops dramatically between 1.0% and 1.5% for both the

1300°C and 1200°C. This indicates that an Al doping level of ~1.0% gives the best material for thermoelectric performance based upon the dimensionless figure of merit.

(Tsubota et al., 1997) prepared bulk samples of Al doped ZnO in a similar fashion to the synthesis carried out above, the samples were found to have figures of merits in the order of ZT = 0.01 in the room temperature regime. Although the values obtained from Tsubota et al.'s work are much higher than here, the electronic resistivity was found to be several orders of magnitude lower than in this experiment, this leads to a drastic difference of the calculated values of ZT. The electrical resistivity was found to increase drastically with sintering temperature as shown in *chapter 5*, which has had a large impact upon ZT. It is therefore acceptable to deduce that the electrical resistivity, and by extension, the figure of merit is sensitive to initial processing sinter treatment conditions. Due to the large difference in calculated electrical resistivity, it is apparent that the electronic resistivity is the main cause for the reduction in the figure of merit of the samples.

The *ZT* values are at maximum at an Sb content of 0.4at.% for the samples sintered at both 1200°C and 1300°C, this is partially due to the electrical resistivity of the materials which forms a minimum at an Sb content of 0.4at.% (*Chapter 5*). The electrical resistivity has a significant impact upon the figure of merit. The behaviour of the sample at 1100°C can be explained better by studying the Seebeck behaviour (*Chapter 6*). The Seebeck coefficient increases between 0.4at.% and 0.8at.% Sb content forming a maximum at 0.8at.% then retreating slightly. This counteracts the effects of resistivity upon the ZT value and so a plateau is formed.

The Seebeck forms a maximum at 0.4at.% for the 1300°C sample which then decreases, this could also help explain the peak in ZT which then decreases. The thermal conductivity does not have as much of an impact upon the ZT values between samples due to little variation of the thermal conductivity values between samples.

While the figures of merit are much lower than what would be expected it is important to note that the values were obtained at a relatively narrow range of temperatures, a range of temperatures below what ZnO operates best at, which can be used up to and beyond 800K (Lu and Ferguson, 2013). In literature, the thermal behaviour of ZnO is studied in the high

temperature regime, up to approximately 1000K, while little is studied in the low temperature region.

7.3. Efficiency

The Efficiency of the thermoelectric conversion of heat energy into electrical energy for the Al and Sb doped samples was calculated from *Equation (13)* and is shown in *Figure 80* and *Figure 81* respectively.

$$\eta = \frac{\Delta T}{T_h} \cdot \frac{\sqrt{1+ZT}-1}{\sqrt{1+ZT}+\frac{T_c}{T_h}} \qquad (13)$$

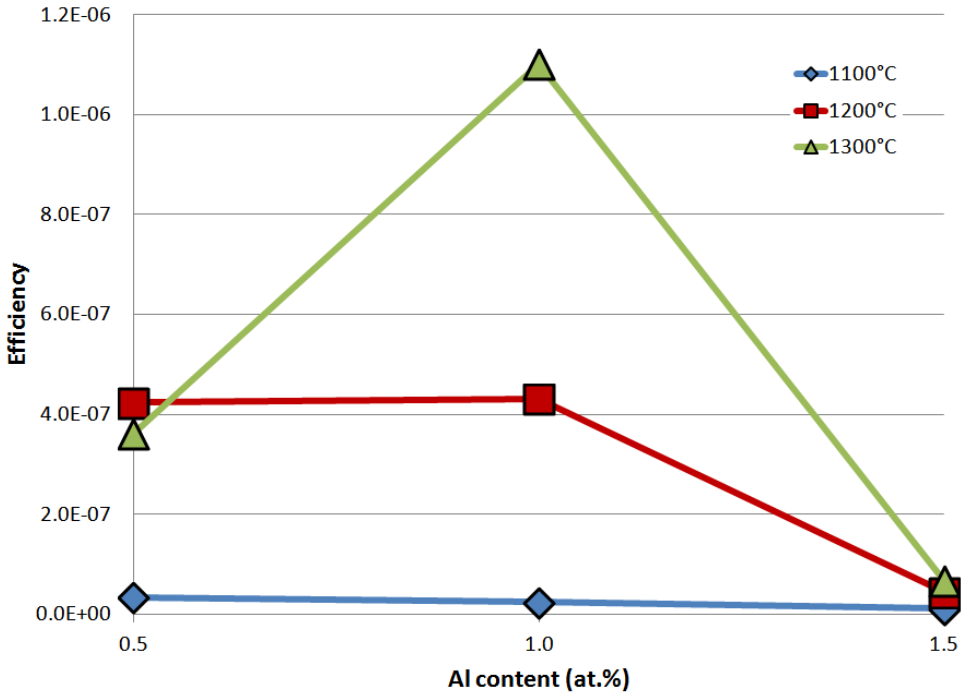

Figure 80: Thermoelectric conversion efficiency of Al doped ZnO as a function of Al content sintered at 1100°C, 1200°C, and 1300°C with Al content of 0.5at.%, 1.0at.%, and 1.5at.%

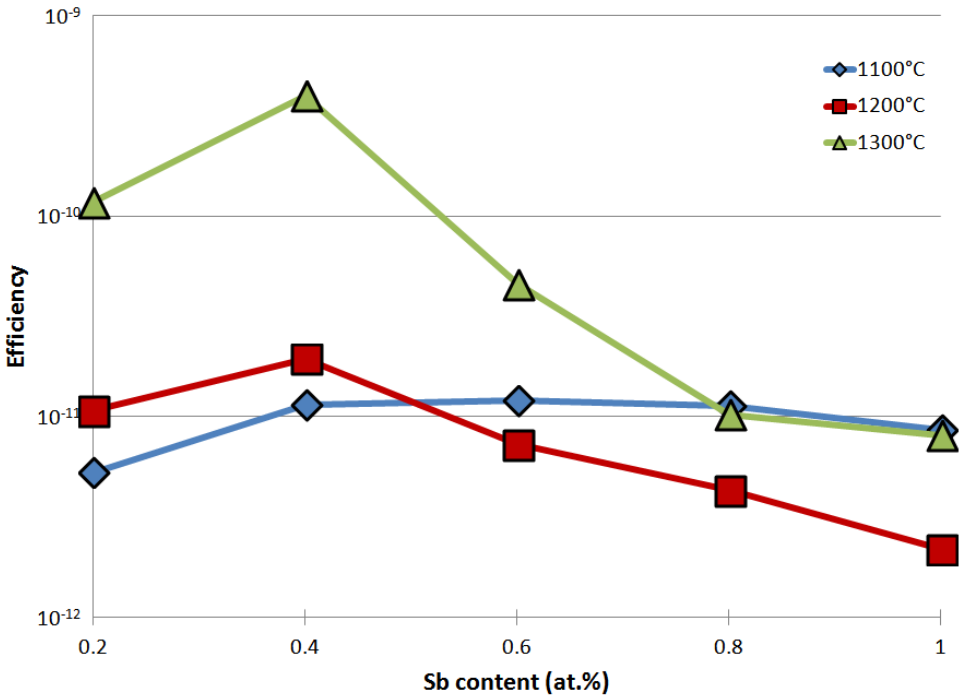

Figure 81: Thermoelectric conversion efficiency of Sb doped ZnO as a function of Sb content sintered at 1100°C, 1200°C, and 1300°C with Sb content of 0.2at.%, 0.4at.%, 0.6at.%, 0.8at.%, and 1.0at.%

The efficiency is strongly dependent upon the ZT value of the material, and therefore the efficiencies shown in *Figure 80* and *Figure 81* also follow the same trends as for the Figure of merits in *Figure 78* and *Figure 79*. The samples sintered at 1200°C and 1300°C for the Sb doped ZnO samples follow a similar trend, that the efficiency increases from 0.2at.% to 0.4at.% where it forms a maximum before decreasing between 0.4at.% to 1.0at.%. This implies that for the Sb doped samples, the most efficient material has a Sb content between 0.2at.% and 0.6at.%. The samples sintered at 1100°C increase between 0.2 at.% and 0.4 at.% , similar to the results at 1200°C and 1300°C but then remain broadly constant with Sb content. This implies that the efficiency of the material at low sintering temperature is not as strongly dependent on the Sb content as at higher temperatures.

7. Thermoelectric characterisation

The thermal properties of the tested materials is displayed in *Table 4*. In the room temperature regime, the main differing factor between the data in this work and that for other authors is that the electrical resistivity is much larger in this work. This has the effect of reducing the power factor and the figure of merit due to these properties being related to the electrical resistivity. The Seebeck coefficient is consistent with literature values. Generally the literature values change with increasing temperature, the electrical resistivity, Seebeck coefficient, and the figure of merit are dependent upon the operating temperature. The temperature range used to analyse the doped ZnO materials in this study is outside the range that ZnO operates best at. Therefore it is speculated that the values obtained in this study would improve at elevated operating temperatures and become more consistent with data obtained from literature sources.

Table 4: The thermoelectric properties of bulk Al doped ZnO material as compared to values obtained in other studies

	This work	*(Tsubota et al., 1997)*	(Ohtaki et al., 2009)	*(Tsubota et al., 1997)*	(Ohtaki et al., 2009)
Electrical resistivity, ρ (Ω.cm)	$2.0x10^{-1}$ – $2.0x10^{2}$	1.0 – 6.0 $x10^{-3}$	5.6 $x10^{-4}$	1.0 – 10 $x10^{-3}$	7.3 – 13 $x10^{-4}$
Thermal conductivity, κ ($W.m^{-1}.K^{-1}$)	1.5 – 3.0	35 – 40	40	5 – 25	8 – 18
Seebeck coefficient, S ($\mu V.K^{-1}$)	-17 – -100	-100 – -160	-84	-110 – -250	-100 – -147
Power factor, $S^2\sigma$ ($W.m^{-1}.K^{-2}$)	0.01 – 0.57 $x10^{-6}$	7 – 22 $x10^{-4}$	12 $x10^{-4}$	3 – 22 $x10^{-4}$	11.1 – 14.8 $x10^{-4}$
Figure of merit, ZT	4.0 $x10^{-7}$ – $1.0x10^{-4}$	0.01 – 0.02	0.01	0.03 – 0.3	0.03 – 0.2
Al content (atomic %)	0.5 – 1.5	1.0 – 5.0	2.0	1.0 – 5.0	2.0
Temperature range (°C)	20 – 60	20 – 60	Room temperature	100 – 1000	200 – 800

8. Conclusion

A better understanding of the effects that microstructure plays on thermoelectric behaviour has been developed. The thermoelectric behaviour was shown to have strong grain size dependence with the microstructure not only affecting thermal conductivity and electrical conductivity but also the Seebeck coefficient.

There are many factors to consider when identifying a suitable thermoelectric material for specific applications. The electrical resistivity and thermal conductivity are often closely related in the material, with an improvement in one often results in a detrimental effect in the other and little or no net improvement in the figure of merit being observed.

The Al doped material incorporates effectively into the ZnO system and no secondary phases are produced. The Seebeck coefficient is reduced through incorporation of Al into the ZnO structure due to increase in the carrier concentration. Grain size and porosity also play a significant role with small grains and higher levels of porosity leading to higher values of Seebeck coefficient.

The Sb doped ZnO material displays n-type behaviour which is intriguing as Sb is considered a p-type dopant in the ZnO system. It is proposed that at low doping levels <1.0at.%, Sb incorporates onto the Zn site rather than the O site as expected, and act as a donor which leads to n-type behaviour. The addition of Sb dopant leads to the formation of secondary phases which appear to increase the Seebeck coefficient by an energy filtering effect. Higher levels of dopant leads to higher levels of secondary phase. The grain size and porosity also have a significant impact upon the observed Seebeck coefficients.

When considering real materials undergoing sintering, the microstructure changes significantly with the material starting off as highly porous with small grains. As sintering progresses, the level of porosity decreases and grains increase in size. During the final stages of sintering the level of porosity may not change significantly, but grain growth may be more significant.

The morphology of the material should be taken into consideration as it has a strong impact not only upon the electrical and thermal conductivity but also the Seebeck coefficient. The grain size is an important factor when considering a thermoelectric material, as there is a dependence of the Seebeck coefficient on the grain size, with higher Seebeck coefficients observed for materials with smaller grain size. This is due to the energy filtering effect whereby the interface between grains forms an electrical junction, a barrier through which the electrons must pass. Any electron with energy lower than the barrier height does not have enough energy to overcome the electrical barrier and therefore is filtered out and may not pass through the material. This has the effect of increasing the overall average energy of the electrons which pass through the grains. A material with smaller grains has a larger amount of overall grain interface which electrons must pass through. This has the effect of increasing the cumulative effect which results in higher Seebeck coefficient being observed.

The Seebeck coefficient is also dependent upon the amount of secondary phase present within the material. It is speculated that the secondary phases reside at the surface of the grains at the grain boundary interface. This has the effect of changing the electrical properties of the junction compared to an interface of material with no secondary phase. A higher amount of secondary phases within the system means that a higher concentration is found in the interfaces between grains which then increases the barrier height, further increasing the energy filtering effect.

The electrical conductivity is strongly dependent upon the sintering conditions, after higher sintering temperatures the electrical conductivity was lower than the conductivity at lower sintering temperatures. This links to the level of porosity, with vast increases in resistivity with level of porosity. The electrical resistivity, both for the bulk and the matrix resistivity, also increases with the level of dopant, this is due to pinning effects caused by secondary phases within the material.

The power factor and figure of merit were highest for the samples sintered at the highest temperatures. This is linked to the grain size and porosity, despite the higher thermal conductivity of samples found at higher porosity, and the higher Seebeck coefficients for samples sintered at lower temperatures with low grain diameter. The improvements to electrical conductivity with increasing grain diameter are so vast they compensate for the

detrimental effects. The electrical conductivity is very sensitive to changes in the porosity which means that the main contribution to improvements to the figure of merit is the improvement of electrical conductivity which comes with increased sintering temperature.

An ideal thermoelectric material will have a low electrical resistivity, therefore when identifying an idealised material based upon the resistivity, the grain sizes should be large to minimise the number of scattering sites. This can be done through sintering at high temperatures, this will also minimise the amount of secondary phases within the material. A high Seebeck coefficient is desirable for thermal energy harvesting, therefore in terms of an idealised material based upon the Seebeck coefficient, grain sizes should be small in order to increase the carrier energy filtering effect. This can be achieved through reducing the sintering temperature, however this will have a negative effect upon the electrical resistivity which require large grains for improved thermoelectric performance and will compensate for attempts at improving the thermoelectric power factor.

8.1. Further work

Further work would study the effects of doping ZnO in more detail, in the Al doped system a wider range of doping levels would be studied in order to obtain a more detailed picture of the effects that Al doping concentration has on the thermoelectric behaviour of ZnO. It is shown that grain size affects the thermoelectric behaviour, in particular the Seebeck coefficient and expanding upon this through controlled sintering would gain a better understanding of the macro effects that microstructure modification plays. The grain sizes can be altered through sintering conditions.

Grain size effects have an impact upon the thermoelectric behaviour therefore in order to gain a better understanding of these effects, further work should be carried out focussing on the grain size effects and also the degree of secondary phase present. It is speculated that decreasing the grain size further would further enhance the grain size energy filtering effect and therefore increase the observed Seebeck coefficient. Investigations into altering sintering conditions in order to partially separate connection between the grain size and

degree of secondary phase of the sintered material can be carried out can be accomplished by using methods such as hot pressure sintering and spark plasma sintering.

It is speculated that the Sb doped system would switch from n-type to p-type as the Sb dopant content reaches above ~1 at.%. This would be met with increasing p-type Seebeck behaviour as the majority of charge carriers within the ZnO material shifts from electrons to holes with increasing Sb content. Therefore studies in Sb doping of above 1.0at.% should be carried out in order to investigate this proposed effect.

The thermoelectric behaviour was carried out in the room temperature region, at a temperature where the ZnO system does not operate best at, and because of this some of the observations, in particular the figures for power factor and the ZT values were lower than they would be when studied at elevated temperatures. In order to observe a greater depth of understanding of how the synthesised materials behave at proposed operating temperatures, the thermoelectric behaviour should be studied at elevated temperatures above the room temperature regime.

References

Apostol, M. and Nedelcu, M. (2001), "Ultrafast thermoelectric conduction", *International Conference on Thermoelectrics, ICT, Proceedings,* pp. 42.

Apostol, M. and Nedelcu, M. (2010), "Pulsed thermoelectricity", *Journal of Applied Physics,* vol. 108, no. 2.

Bachmann, M., Czerner, M. and Heiliger, C. (2012), "Ineffectiveness of energy filtering at grain boundaries for thermoelectric materials", *Physical Review B - Condensed Matter and Materials Physics,* vol. 86, no. 11.

Claflin, B., Look, D. C., Park, S. J. and Cantwell, G. (2006), "Persistent n-type photoconductivity in p-type ZnO", *Journal of Crystal Growth,* vol. 287, no. 1, pp. 16-22.

Coleman, V.A. and Jagadish, C., (2006), *Basic Properties and Applications of ZnO*.

Dughaish, Z. H. (2002), "Lead telluride as a thermoelectric material for thermoelectric power generation", *Physica B: Condensed Matter,* vol. 322, no. 1-2, pp. 205-223.

Fan, J. C., Sreekanth, K. M., Xie, Z., Chang, S. L. and Rao, K. V. (2013a), "P-Type ZnO materials: Theory, growth, properties and devices", *Progress in Materials Science,* vol. 58, no. 6, pp. 874-985.

Fan, J. C., Sreekanth, K. M., Xie, Z., Chang, S. L. and Rao, K. V. (2013b), "p-Type ZnO materials: Theory, growth, properties and devices", *Progress in Materials Science,* vol. 58, no. 6, pp. 874-985.

Fleurial, J. -. (2009), "Thermoelectric power generation materials: Technology and application opportunities", *JOM,* vol. 61, no. 4, pp. 79-85.

Freunek, M., Müller, M., Ungan, T., Walker, W. and Reindl, L. M. (2009), "New physical model for thermoelectric generators", *Journal of Electronic Materials,* vol. 38, no. 7, pp. 1214-1220.

Gao, Y. W., He, Y. Z. and Zhu, L. L. (2010), "Impact of grain size on the Seebeck coefficient of bulk polycrystalline thermoelectric materials", *Chinese Science Bulletin,* vol. 55, no. 1, pp. 16-21.

Han, L., Van Nong, N., Zhang, W., Hung, L. T., Holgate, T., Tashiro, K., Ohtaki, M., Pryds, N. and Linderoth, S. (2014), "Effects of morphology on the thermoelectric properties of Al-doped ZnO", *RSC Advances,* vol. 4, no. 24, pp. 12353-12361.

He, J., Liu, Y. and Funahashi, R. (2011), "Oxide thermoelectrics: The challenges, progress, and outlook", *Journal of Materials Research,* vol. 26, no. 15, pp. 1762-1772.

Jantrasee, S., Pinitsoontorn, S. and Moontragoon, P. (2014), "First-principles study of the electronic structure and thermoelectric properties of al-doped ZnO", *Journal of Electronic Materials,* vol. 43, no. 6, pp. 1689-1696.

Jood, P., Mehta, R. J., Zhang, Y., Peleckis, G., Wang, X., Siegel, R. W., Borca-Tasciuc, T., Dou, S. X. and Ramanath, G. (2011), "Al-doped zinc oxide nanocomposites with enhanced thermoelectric properties", *Nano Letters,* vol. 11, no. 10, pp. 4337-4342.

Kinemuchi, Y., Nakano, H., Mikami, M., Kobayashi, K., Watari, K. and Hotta, Y. (2010), "Enhanced boundary-scattering of electrons and phonons in nanograined zinc oxide", *Journal of Applied Physics,* vol. 108, no. 5.

Koumoto, K., Terasaki, I. and Funahashi, R. (2006), "Complex oxide materials for potential thermoelectric applications", *MRS Bulletin,* vol. 31, no. 3, pp. 206-210.

Lee, D., Dulai, G. and Karanassios, V. (2013), "Survey of energy harvesting and energy scavenging approaches for on-site powering of wireless sensor- and microinstrument-networks", *Proceedings of SPIE - The International Society for Optical Engineering,* Vol. 8728, .

Li, J. -., Liu, W. -., Zhao, L. -. and Zhou, M. (2010), "High-performance nanostructured thermoelectric materials", *NPG Asia Materials,* vol. 2, no. 4, pp. 152-158.

Limpijumnong, S., Zhang, S. B., Wei, S. -. and Park, C. H. (2004), "Doping by large-size-mismatched impurities: The microscopic origin of arsenicor antimony-doped p-type zinc oxide", *Physical Review Letters,* vol. 92, no. 15, pp. 155504-1.

Liu, H. Y., Izyumskaya, N., Avrutin, V., Özgür, U., Yankovich, A. B., Kvit, A. V., Voyles, P. M. and Morkoç, H. (2012), "Donor behavior of Sb in ZnO", *Journal of Applied Physics,* vol. 112, no. 3.

Liu, J., Wang, H. C., Su, W. B., Wang, C. L., Zhang, J. L. and Mei, L. M. (2010), "Synthesis and thermoelectric properties of Sr0.95La0.05TiO3-d-TiO2 solid solutions", *Solid State Sciences,* vol. 12, no. 1, pp. 134-137.

Lu, N. and Ferguson, I. (2013), "III-nitrides for energy production: Photovoltaic and thermoelectric applications", *Semiconductor Science and Technology,* vol. 28, no. 7, pp. 1-11.

Maldonado, F. and Stashans, A. (2010), "Al-doped ZnO: Electronic, electrical and structural properties", *Journal of Physics and Chemistry of Solids,* vol. 71, no. 5, pp. 784-787.

Marina, O. A., Canfield, N. L. and Stevenson, J. W. (2002), "Thermal, electrical, and electrocatalytical properties of lanthanum-doped strontium titanate", *Solid State Ionics,* vol. 149, no. 1-2, pp. 21-28.

Martin, J. (2013), "Protocols for the high temperature measurement of the Seebeck coefficient in thermoelectric materials", *Measurement Science and Technology,* vol. 24, no. 8.

Martin, J., Tritt, T. and Uher, C. (2010), "High temperature Seebeck coefficient metrology", *Journal of Applied Physics,* vol. 108, no. 12.

Min, G. and Rowe, D. M. (1992), "Optimisation of thermoelectric module geometry for 'waste heat' electric power generation", *Journal of Power Sources,* vol. 38, no. 3, pp. 253-259.

Muta, H., Ieda, A., Kurosaki, K. and Yamanaka, S. (2004), "Substitution effect on the thermoelectric properties of alkaline earth titanate", *Materials Letters,* vol. 58, no. 30, pp. 3868-3871.

Muta, H., Kurosaki, K. and Yamanaka, S. (2003), "Thermoelectric properties of rare earth doped SrTiO3", *Journal of Alloys and Compounds,* vol. 350, no. 1-2, pp. 292-295.

Nagayoshi, H., Kajikawa, T. and Sugiyama, T. (2002), "Comparison of maximum power point control methods for thermoelectric power generator", *Thermoelectrics, 2002. Proceedings ICT '02. Twenty-First International Conference on,* pp. 450.

Narducci, D., Selezneva, E., Cerofolini, G., Frabboni, S. and Ottaviani, G. (2012), "Impact of energy filtering and carrier localization on the thermoelectric properties of granular semiconductors", *Journal of Solid State Chemistry,* vol. 193, pp. 19-25.

Nedelcu, M., Stoican, O. and Stockholm, J. G. (2002), "Thermoelectric generators with electric pulsed output", *Thermoelectrics, 2002. Proceedings ICT '02. Twenty-First International Conference on,* pp. 439.

Nolasa, G. S., Kaeser, M., Littleton, R. T. and Tritt, T. M. (2000), "High figure of merit in partially filled ytterbium skutterudite materials", vol. 77, no. 12, pp. 1855.

Ohta, H. (2007), "Thermoelectrics based on strontium titanate", *Materials Today,* vol. 10, no. 10, pp. 44-49.

Ohtaki, M., Araki, K. and Yamamoto, K. (2009), "High thermoelectric performance of dually doped ZnO ceramics", *Journal of Electronic Materials,* vol. 38, no. 7, pp. 1234-1238.

Ohtaki, M. and Hayashi, R. (2006), "Enhanced thermoelectric performance of nanostructured ZnO: A possibility of selective phonon scattering and carrier energy filtering by nanovoid structure", *International Conference on Thermoelectrics, ICT, Proceedings,* pp. 276.

Olorunyolemi, T., Birnboim, A., Carmel, Y., Wilson Jr., O. C., Lloyd, I. K., Smith, S. and Campbell, R. (2002), "Thermal conductivity of zinc oxide: From green to sintered state", *Journal of the American Ceramic Society,* vol. 85, no. 5, pp. 1249-1253.

Omer, S. A. and Infield, D. G. (1998), "Design optimization of thermoelectric devices for solar power generation", *Solar Energy Materials and Solar Cells,* vol. 53, no. 1-2, pp. 67-82.

Onodera, A. and Takesada, M. (2012), "Electronic Ferroelectricity in II-VI Semiconductor ZnO", in Peláiz-Barranco, A. (ed.) *Advances in Ferroelectrics,* InTech, .

Özgür, Ü, Gu, X., Chevtchenko, S., Spradlin, J., Cho, S. -., Morkoç, H., Pollak, F. H., Everitt, H. O., Nemeth, B. and Nause, J. E. (2006), "Thermal conductivity of bulk ZnO after different thermal treatments", *Journal of Electronic Materials,* vol. 35, no. 4, pp. 550-555.

Park, J. W., Kwak, D. H., Yoon, S. H. and Choi, S. C. (2009), "Thermoelectric properties of Bi, Nb co-substituted CaMnO3 at high temperature", *Journal of Alloys and Compounds,* vol. 487, no. 1-2, pp. 550-555.

Park, K., Seong, J. K. and Nahm, S. (2008), "Improvement of thermoelectric properties with the addition of Sb to ZnO", *Journal of Alloys and Compounds,* vol. 455, no. 1-2, pp. 331-335.

Pradhan, A. K., Mundle, R. M., Santiago, K., Skuza, J. R., Xiao, B., Song, K. D., Bahoura, M., Cheaito, R. and Hopkins, P. E. (2014), "Extreme tunability in aluminum doped Zinc Oxide plasmonic materials for near-infrared applications", *Scientific Reports,* vol. 4.

Rowe, D. M. and Min, G. (1998), "Evaluation of thermoelectric modules for power generation", *Journal of Power Sources,* vol. 73, no. 2, pp. 193-198.

Ruoho, M. (2012), *Nanostructured thermoelectric materials* (unpublished Master of Science in Technology thesis), Aalto University, .

Sales, B. C., Mandrus, D., Chakoumakos, B. C., Keppens, V. and Thompson, J. R. (1997), "Filled skutterudite antimonides: Electron crystals and phonon glasses", *Physical Review B - Condensed Matter and Materials Physics,* vol. 56, no. 23, pp. 15081-15089.

Sales, B. C., Mandrus, D. and Williams, R. K. (1996), "Filled skutterudite antimonides: A new class of thermoelectric materials", *Science,* vol. 272, no. 5266, pp. 1325-1328.

Savaniu, C. -. and Irvine, J. T. S. (2009), "Reduction studies and evaluation of surface modified A-site deficient La-doped SrTiO3 as anode material for IT-SOFCs", *Journal of Materials Chemistry,* vol. 19, no. 43, pp. 8119-8128.

Shang, P. -., Zhang, B. -., Liu, Y., Li, J. -. and Zhu, H. -. (2011), "Preparation and thermoelectric properties of la-doped SrTiO 3 ceramics", *Journal of Electronic Materials,* vol. 40, no. 5, pp. 926-931.

Shi, X., Bai, S., Xi, L., Yang, J., Zhang, W., Chen, L. and Yang, J. (2011), "Realization of high thermoelectric performance in n-type partially filled skutterudites", *Journal of Materials Research,* vol. 26, no. 15, pp. 1745-1754.

Shikano, M. and Funahashi, R. (2003), "Electrical and thermal properties of single-crystalline (Ca2CoO3)0.7CoO2 with a Ca3Co4O9 structure", *Applied Physics Letters,* vol. 82, no. 12, pp. 1851-1853.

Slack, G. A. and Tsoukala, V. G. (1994), "Some properties of semiconducting IrSb3", *Journal of Applied Physics,* vol. 76, no. 3, pp. 1665-1671.

Snyder, G. J. and Toberer, E. S. (2008), "Complex thermoelectric materials", *Nature Materials,* vol. 7, no. 2, pp. 105-114.

Sopicka-Lizer, M., Smaczynski, P., Kozlowska, K., Bobrowska-Grzesik, E., Plewa, J. and Altenburg, H. (2005), "Preparation and characterization of calcium cobaltite for thermoelectric application", *Journal of the European Ceramic Society,* vol. 25, no. 12 SPEC. ISS., pp. 1997-2001.

Tahashi, M., Tanimoto, T., Goto, H., Takahashi, M. and Idoz, T. (2010), "Sintering temperature dependence of thermoelectric performance and crystal phase of calcium cobalt oxides", *Journal of the American Ceramic Society,* vol. 93, no. 10, pp. 3046-3048.

Tang, X., Zhang, Q., Chen, L., Goto, T. and Hirai, T. (2005), "Synthesis and thermoelectric properties of p -type- and n -type-filled skutterudite R yM xCo 4-xSb 12 (R: Ce, Ba, Y; M: Fe, Ni)", *Journal of Applied Physics,* vol. 97, no. 9.

Terasaki, I., Sasago, Y. and Uchinokura, K. (1997), "Large thermoelectric power in NaCo2O4 single crystals", *Physical Review B - Condensed Matter and Materials Physics,* vol. 56, no. 20, pp. R12685-R12687.

Tritt, T. M. and Subramanian, M. A. (2006), "Thermoelectric materials, phenomena, and applications: A bird's eye view", *MRS Bulletin,* vol. 31, no. 3, pp. 188-194.

Tseng, J.C., Schmidt, W., Sager, U., Dauber, E., Pommerin, A. and Weidenthaler, C., (2015), *Microstructure analysis of complex CuO/ZnO@carbon adsorbers: what are the limits of powder diffraction methods?*, The Royal Society of Chemistry.

Tsubota, T., Ohtaki, M., Eguchi, K. and Arai, H. (1997), "Thermoelectric properties of Al-doped ZnO as a promising oxide material for high-temperature thermoelectric conversion", *Journal of Materials Chemistry,* vol. 7, no. 1, pp. 85-90.

Wahl, U., Correia, J. G., Mendona, T. and Decoster, S. (2009), "Direct evidence for Sb as a Zn site impurity in ZnO", *Applied Physics Letters,* vol. 94, no. 26.

Yamamoto, T. and Katayama-Yoshida, H. (1999), "Solution using a codoping method to unipolarity for the fabrication of p-type ZnO", *Japanese Journal of Applied Physics, Part 2: Letters,* vol. 38, no. 2 B, pp. L166-L169.

Yu, C., Scullin, M. L., Huijben, M., Ramesh, R. and Majumdar, A. (2008), "Thermal conductivity reduction in oxygen-deficient strontium titanates", *Applied Physics Letters,* vol. 92, no. 19.

Zhou, Z. and Uher, C. (2005), "Apparatus for Seebeck coefficient and electrical resistivity measurements of bulk thermoelectric materials at high temperature", *Review of Scientific Instruments,* vol. 76, no. 2, pp. 023901-1-023901-5.